A STOCHASTIC EXPANSION-BASED APPROACH FOR DESIGN UNDER UNCERTAINTY

A Thesis
Presented to
The Academic Faculty

by

Miguel A. T. Walter

In Partial Fulfillment
of the Requirements for the Degree
Doctor of Philosophy in the
School of Aerospace Engineering

Georgia Institute of Technology
May 2013

A STOCHASTIC EXPANSION-BASED APPROACH FOR DESIGN UNDER UNCERTAINTY

Approved by:

Professor Dimitri Mavris, Advisor
School of Aerospace Engineering
Georgia Institute of Technology

Professor Brian German
School of Aerospace Engineering
Georgia Institute of Technology

Professor Lakshmi Sankar
School of Aerospace Engineering
Georgia Institute of Technology

Professor Jechiel Jagoda
School of Aerospace Engineering
Georgia Institute of Technology

Professor Rafael de la Llave
School of Mathematics
Georgia Institute of Technology

Date Approved: February 4, 2013

In memory of my mother,

Gloria Walter (1948-2008)

ACKNOWLEDGEMENTS

I would like to thank my advisor, Professor Mavris, for his guidance and support. Having my previous background mostly in computational fluid dynamics and combustion, I have inmensely gained knowledge and experience in the fascinating area of aircraft design during my staying in his laboratory. I would also like thank the members of my committee: Dr. German, Dr. Sankar, Dr. Jagoda and Dr. de la Llave, for their valuable advice and criticisms.

I would like to express my appreciation to all my friends and colleagues at the laboratory, especially Chung Lee for the encouragement and long discussions during the course of this dissertation. Thanks to my friends and former colleagues from the computational combustion laboratory for all the time spent together during my first years at the institute. I am also grateful to Ryan Westafer, Ian Harrison and Shawn Lankton for all these years of friendship and for making my transition to this country and culture more fun.

I am eternally grateful to my mother for her love, life dedication, and her encouragement for pursuing higher education. I would have liked for her to see me finishing this work; unfortunately, she passed away during my time at the institute. I am also extremely thankful to my brother, Julio, who instilled in me the interest in learning mathematics and science.

TABLE OF CONTENTS

LIST OF TABLES

LIST OF FIGURES

SUMMARY

An approach for robust design based on stochastic expansions is investigated. The research consists of two parts : 1) stochastic expansions for uncertainty propagation and 2) adaptive sampling for Pareto front approximation. For the first part, a strategy based on the generalized polynomial chaos (gPC) expansion method is developed. Second, in order to alleviate the computational cost of approximating the Pareto front, two strategies based on adaptive sampling for multi-objective problems are presented. The first one is based on the two aforementioned methods, whereas the second one considers, in addition, two levels of fidelity of the uncertainty propagation method.

Uncertainty is important because designers are concerned about performance risk. One of the major challenges in design under uncertainty is computational efficiency, especially for computational intensive simulations. Design under uncertainty is composed of two major parts. The first one is the propagation of uncertainties, and the other one is the optimization method. An efficient approach for design under uncertainty should consider improvement in both parts.

Uncertainty propagation based on conventional methods such as Monte Carlo require a large sample size. Other methods, such as local expansion offer low computational cost; however, their applicability is limited to sufficiently small ranges of random inputs and low degree of the non-linearity of the cost functions. A more recent class of uncertainty propagation methods are those based on stochastic expansions. They have shown to perform accurately with a fraction of the expense of Monte Carlo methods.

In the present work, a strategy based on the non-intrusive polynomial chaos expansion method is proposed for the uncertainty propagation part. A common limitation in previous gPC-based approaches for robust design is the growth of the computational cost with number of uncertain parameters. In this research, the computational cost is addressed by using sparse grids as a mean to alleviate the curse of dimensionality.

For scenarios of highly non-linear cost functions or large degrees of uncertainties, the use of an efficient uncertainty propagation may still be expensive for effective application in robust design optimization. Therefore, efficient methods for sampling the design space are necessary. For this reason, two strategies based on the multi-objective expected improvement, an efficient adaptive sampling method for multi-objective problem, are presented. The first one simply uses the gPC based method in conjunction with multi-objective expected improvement. The other is based on two different levels of accuracy (fidelity) for the uncertainty propagation method. In this strategy, the accuracy is provided by the high fidelity propagator, whereas a lower uncertainty propagator drives the overall efficiency. The gPC-based strategy is employed as the high level propagator, whereas a low cost propagator is considered as the low level propagator.

The proposed approaches were tested successfully in a low Reynolds number airfoil robust optimization with uncertain operating conditions and the robust design of a transonic wing. The gPC-based method is able to find the same Pareto front as a reference Monte Carlo-based strategy but with lower computational cost. The bi-level strategy shows further computational efficiency.

CHAPTER I

INTRODUCTION

1.1 *Motivation*

In the last few decades, the drive to increase performance and reduce cost within the aerospace industry has led to the development of efficient design and optimization approaches. Such methods rely heavily on numerical simulations in many different disciplines. A common practice in engineering has been to carry out deterministic analysis in the design process. However, uncertainty is ubiquitous to any real engineering system due to variations in design conditions such as material properties, physical dimensions and operating conditions.

The use of deterministic approaches greatly simplifies the design process since any uncertain parameter is set to a nominal value. The final design, however, can have degraded performance if the actual parameter values are slightly different from the nominal ones [63]. Therefore, it is often important to account for off-design conditions in the design process to avoid performance deficiencies not only during operation, but also in later development and testing phases. Moreover, treatment of uncertainty can potentially provide useful information that can aid in decision making during the design process.

Design methods that pursue minimum sensitivity to inherent fluctuations of the operating conditions or manufacturing processes are of crucial importance in aerospace engineering. For instance, assume an aircraft is designed to consume some amount of fuel for a nominal payload weight and mission. The actual cargo weight may vary in everyday operations. This variation may require the airplane to fly at different angles of attack. As a result, the drag, the thrust required, and ultimately fuel consumption

1

may be quite different from intended values. A design with fuel consumption that is insensitive to payload weight may be more desirable than one with low consumption only for nominal weights.

The consideration of random variation in the design process is known as a design under uncertainty. The two major classes of design formulations that account for uncertainty are robust design (RD) and reliability-based design (RBD) [113]. The purpose of robust design is to obtain designs that are relatively insensitive to small changes in the uncertain quantities so they perform as intended over many operating conditions. In reliability-based design, given some uncertain parameters affecting responses, the main goal is to obtain a design whose probability of failure is lower than some small value. Whether pursuing robust or reliability-based design, one of the main challenges in design under uncertainty is the computational efficiency, especially for expensive numerical simulations.

Design under uncertainty is composed of two major parts. The first part is the propagation of uncertainties from uncontrolled inputs to the cost function of interest. The second part is the optimization method. An efficient approach for design under certainty should consider improvement in both the uncertainty propagation and the optimization methods. Each of these two are discussed.

1.1.1 Uncertainty propagation

Propagation of uncertainties has been addressed in several ways in the literature. The most common methods for the propagation of uncertainty through system outputs are those based on local expansion methods such as the first and second order moment methods. First order methods include the first order first moment (FOFM) and the first order second moment (FOSM), whereas second order methods include the second order first moment (SOFM) and the second order second moment (SOSM); see

for instance references [92, 91, 52]. In these methods, statistical moments are calculated by Taylor expansions of the cost function around the mean of uncertain inputs. Their main advantage is low computational cost and ease of implementation, which only involves the calculation of the response gradients with respect to the uncertain parameters. The main drawback, however, is that these methods are restricted to relatively small ranges of variation and low degrees of non-linearity of responses due to the local validity of the Taylor expansion. The other common approaches are Monte Carlo methods. Their advantages are simplicity of implementation and insensitivity to the number of uncertain parameters. The implementation only involves sampling the uncertain parameters according to a joint probability distribution function and the collection of statistics from the sample. Monte Carlo methods are by nature insensitive to the number of uncertain parameters - dimensionality of the stochastic space. Therefore, they do not suffer from the so-called *"curse of dimensionality* [10, 11]," which is the exponential increase of the computational cost with the number of dimensions. However, the convergence rates of Monte Carlo methods are the main disadvantage. This rate of convergence is of order of $N^{-1/2}$, where N is the size of the sample. Usually, the size of the sample needed to achieve a desired level of accuracy is very large. The implication of this slow convergence rate is high computational cost.

To summarize, the two common approaches are useful but are also prone to difficulties in certain applications. For instance, problems that require large ranges of uncertainty may be poorly predicted by local expansion-based methods due to the methods' local validity. Furthermore, more challenging designs may result on increasingly complex physics which in turn lead to strong non-linear effects of the responses with the uncertain parameters. In such as scenarios, local-based methods can give inaccurate predictions. On the other hand, Monte Carlo methods can give accurate predictions, but their computational cost can quickly become unaffordable.

A more recent class of uncertainty propagation methods are those based on stochastic expansions. Unlike local-based methods or the Monte Carlo methods, they allow high order representation and computational efficiency [111]. Therefore, these methods are intermediates between local expansion and Monte Carlo methods in the trade-off of accuracy and computational cost. Stochastic expansion methods include intrusive and nonintrusive methods. The former involves the treatment of randomness at the discretization level of the partial differential equations, leading to reformulation of the original governing equations. New solvers must be developed or current codes must be modified. Non-intrusive methods, however, acts over the responses of original solvers. Therefore existing codes can be used and they can be treated as black boxes.

Ghanem and Spanos [42] introduced an early intrusive method known as the stochastic Galerkin method. In this method, the Hermite polynomial chaos expansion [108] was used to model uncertainty propagation in solid mechanics. Since then, these methods have been under development and scrutiny, mostly for solving stochastic partial differential equations (SPDE). Some of the main limitations of these methods were highlighted in [25]; however, for more general engineering problems, intrusiveness is the main drawback. Consequently, there is a more recent interest in non-intrusive approaches which can be used with existing deterministic analysis codes. These include the stochastic collocation method and the non-intrusive polynomial chaos. They have been shown to perform accurately with a fraction of the expense of techniques that have similar capabilities such as the Monte Carlo method [71, 76].

The proper selection of an uncertainty propagation method depends on the problem of interest, and several aspects need to be considered. Uncertainty in problems whose responses exhibit low degree of non-linearity and sufficiently small ranges of uncertainty can be efficiently predicted by using local expansion based approaches. In contrast, for more general problems such those involving large degree of uncertainty

and highly non-linear responses, sampling methods such as Monte Carlo can be accurate but at largely higher cost. Therefore, for more general problems, the efficiency in propagating uncertainties is the main limitation. The usefulness of stochastic expansion methods in robust design has been argued; for instance, see [69, 85]. However, these arguments are based on some analytical tests that address the strength of the other methods rather than those of stochastic expansions. Nevertheless, in scenarios of highly non-linear responses and large degrees of uncertainties, computational efficiency is a key advantage of stochastic expansion methods [79].

Because of their compatibility with deterministic solvers, non-intrusive stochastic expansions methods are attractive for use in design under uncertainty. This is especially important for design organizations that use legacy codes. Recent studies [27, 44, 45] have shown the usefulness of the non-intrusive generalized polynomial chaos (gPC) in robust design optimization. These works use a formulation that relies on full tensor quadrature integration techniques for the calculation of the gPC coefficients. However, in more realistic problems, the use of such integration techniques limits the applicability of the non-intrusive polynomial chaos for uncertainty propagation because computational cost (number of deterministic code runs) grows exponentially with the number of stochastic dimensions. Thus, the polynomial chaos-based approaches developed in these previous works are only applicable to problems with few uncertain parameters.

The development of a method to address more uncertain parameters is a focus of this thesis. Because the cost of propagating uncertainties is one of the main difficulties in robust design, it is necessary to develop methods that can reduce the cost when dealing with uncertainties for scenarios of highly non-linear responses or wide range of uncertainties. In the present work, a strategy based on the non-intrusive polynomial chaos expansion is presented. The main difference with previous works [27, 44, 45] is

the use of sparse grids integration techniques as a mean to reduce the cost of calculating the gPC coefficients. Sparse grids [14] are effective techniques for representing multivariate functions. This approach can yield several of order of magnitude reduction in the number of points required to achieve the same level of accuracy as the full tensor grid approach and thus can alleviate the curse of dimensionality.

1.1.2 Optimization approach

Efficient approaches for design under uncertainty should not only consider efficient methods for uncertainty propagation but also efficient methods for optimization. Therefore, improvements on the optimization part are also required. A promising technique to be incorporated in design under uncertainty is adaptive sampling. This technique sequentially selects each sample in the design space based on information from previously sampled data. Steps towards efficient adaptive sampling for multi-objective optimization have already been taken. For instance, Keane [62] describes a multiobjective expected improvement criteria for adaptive sampling while approaching the Pareto front for multi-objective optimization. This criteria is shown to efficiently sample regions of the design space that improve or augment the current non-dominated set.

In the present work, strategies based on stochastic expansions and adaptive sampling for multi-objective problems are presented. These strategies combine and take advantage of both methods to efficiently propagate uncertainties and sample in the stochastic and design space, respectively. In addition, a strategy that uses multifidelity modeling for design under uncertainty is explored in the present work. This handles two different levels of accuracy (fidelity) of the uncertainty propagation methods. The main idea of using different levels of fidelity of the uncertainty propagation method is that information from a low fidelity propagation method can reduce the use of a high fidelity method. Multifidelity methods has been traditionally employed

for modeling different levels of accuracy of analysis codes and mostly applied to deterministic optimization. Therefore, this strategy is a novel extension of multifidelity methods to design under uncertainty.

Robust design involves the maximization of the performance mean and simultaneous minimization of the standard variation of the performance. These statistical moments can be calculated with different levels of accuracy of uncertainty propagation. For instance, highly accurate statical moments can be calculated by high fidelity propagation method such as Monte Carlo or stochastic expansions, whereas less accurate statistical moments may be given by less sophisticated uncertainty propagation method such as local expansion-based methods. The main idea of working with two different accuracy levels of the uncertainty propagation method is that the information (statistical moments) of a low fidelity propagation method can help to represent the more accurate statistical moments of a high fidelity method. This in turn may reduce the amount of information needed from the more accurate propagation method. In the proposed strategy, the uncertainty propagation method works with two levels of information. The accuracy is given by the high fidelity propagator, whereas a lower uncertainty propagator increases the overall efficiency by providing information that guides the use of the high fidelity propagator. Stochastic expansions are employed as the high fidelity propagation method, whereas a less sophisticated uncertainty propagation method such as a local expansion based approach is considered as the low fidelity propagation method.

The use of different levels of fidelity in model representation is known as a multifidelity approach, variable-complexity model, or multi-level code. Such techniques represent system outputs from data of different degrees of accuracy or 'fidelity' [1].

---

[1]Note: the multiple levels should not be confused with multi-level architectures for multidisciplinary optimization, for example, collaborative optimization decomposes an optimization problem into a discipline and system level.

Often, outputs of system models can be obtained from simulation codes at different levels of fidelity or accuracy, with version ranging from the most sophisticated level of simulation to the most basic. For instance, in physical systems, the high level simulation may contain detailed physics that are not accounted for in a lower level simulation that only includes simplified physics. Moreover, models of different complexities also imply different computational cost. The use of only high level simulations for a system of interest may become too costly. In this case, using data from less expensive simulations to represent the system may reduce the overall cost. This is underlying purpose of multi-fidelity approaches.

Multi-fidelity approaches have been mainly developed and applied to surrogate-based optimization (see for instance [37, 96]). In those cases, the need is to include high fidelity simulations such as computational fluid dynamics or finite element method in the design process. Surrogate modeling of experimental and computational data have also been addressed by multi-fidelity modeling [99, 66], although to a lesser extent. In the present approach, multi-fidelity modeling is applied to a different problem: design under uncertainty. The purpose is to use two different levels of fidelity in the uncertainty propagation method.

1.2 Research questions, hypothesis, and predictions

Assume that a Pareto front of the mean and standard deviation of a cost function is needed for robust design. The first research question, hypothesis and prediction are general and provide a framework for the thesis.

1.2.1 Primary research question (general)

How can uncertainties be propagated efficiently for high degrees of uncertainty and non-linearity?

Hypothesis (general)

Higher computational expense due to higher degree of non-linearity and uncertainty is unavoidable for a *single design point*. However, robust design strategies based on stochastic expansions, adaptive sampling and multi-fidelity modeling for uncertainty propagation can be efficient *while finding a Pareto front*. Stochastic expansions is employed as a means for propagating uncertainty efficiently, whereas adaptive sampling is used for efficient approximation of the Pareto front. Furthermore, the consideration of propagating uncertainties with two different levels of fidelity can achieve further computational efficiency since the low fidelity information helps the high fidelity propagator to focus in regions where higher accuracy is needed.

Prediction (general)

Proof-of-concept approaches based on stochastic expansions, adaptive sampling and multi-fidelity modeling for uncertainty propagation can be formulated for use in robust design.

1.2.2   Secondary research question

What are particular implementations of these general strategies for use in robust design?

Hypothesis

Assume two particular implementations: 1) a single-level method and 2) a bi-level method consists of:

- Uncertainty Propagation based on the generalized polynomial chaos (gPC)

- Multi-objective EI for adaptive sampling in the design space

The bi-level approach considers in addition the propagation of uncertainties with two different levels of fidelity. This is based on a correction factor between :

- Polynomial chaos expansions (gPC) as the high fidelity propagator

- A low fidelity propagator

Prediction

These approaches will behave as in the primary hypothesis: they will efficiently work in the stochastic space for uncertainty propagation, and efficiently sample in the design space while approximating the Pareto front. Moreover, the bi-level method will use low fidelity information to efficiently guide the high fidelity propagator while finding the Pareto front. Efficiency is measured by 1) the number of non-dominated designs at the actual Pareto front and 2) average distance of the non-dominated designs to the actual Pareto front

1.2.3 Third research question

How is the bi-level strategy affected by varying levels of non-linearity and uncertainty?

Hypothesis

The performance will decrease as the degree of non-linearity of the cost function and the level of uncertainty of the random parameters decrease.

Prediction

For a test problem in which non-linearity can be varied, the relative performance (bi-level vs. single level) will decrease as the problem becomes non-linear and the level of uncertainty decreases.

1.3 Thesis layout

Review of important concepts such as uncertainty, uncertainty propagation methods and design under uncertainty formulations are presented in Chapter II. Chapter III is exclusively dedicated to explaining stochastic expansion methods. These methods are described with emphasis on nonintrusive approaches. The proposed polynomial chaos - sparse grid based uncertainty propagation approach is presented in chapter IV. Numerical examples are presented to highlight the advantage of this method compared to others. In chapter V, the proposed strategies for robust design optimization are presented. Then, in chapter VI, the presented strategies are applied to aerodynamic robust design under uncertain operating conditions. Finally, conclusions are presented in Chapter VII.

CHAPTER II

BACKGROUND

2.1 *Uncertainty*

2.1.1   Aleatory and epistemic uncertainty

There are at least two types of uncertainty that need to be distinguished due to their difference in origin, modeling and effects: Aleatory and epistemic uncertainty. As described by Oberkampf *et al.*[82, 83], aleatory uncertainty is defined as the inherent variation associated with the physical system or environment under consideration and is also known as inherent uncertainty, variability, irreducible uncertainty, and stochastic uncertainty. Conversely, epistemic uncertainty derives from some level of ignorance of the system or environment.

Sources of aleatory uncertainty are identified because of the natural randomness in the system or process under consideration. The quantities subjected to uncertainty can take on values in an established or known range, but their exact value will vary by chance from time to time. If sufficient information is available, aleatory uncertainty is generally quantified by probabilistic approaches. In computational simulations of physical systems governed by partial differential equations, common sources of aleatory uncertainty include model parameters, boundary and initial conditions that may vary randomly.

Unlike aleatory uncertainty, epistemic uncertainty results from the lack of knowledge or information. It can be reduced by increasing understanding (either by research or more relevant data) of the system or process of interest. For that reason, this type of uncertainty is also know as reducible uncertainty or subjective uncertainty. In addition to probabilistic approaches, epistemic uncertainty can also be

treated by non-probabilistic approaches such as possibility theory, fuzzy set theory, and evidence theory.

In this work, the framework of probability theory is adopted regardless of the type of uncertainty. Probabilistic approaches provide a solid and comprehensive theoretical foundation and offers the most versatile statistical tools.

2.1.2 Uncertainty quantification process

The uncertainty quantification process, in general, involves two stages: quantification and propagation of uncertainty. Quantification of the uncertainty sources is the first stage of uncertainty quantification. This step is very problem dependent and often involves statistical analysis, experimental error analysis, and often expert judgment [33]. The end result of this stage is a joint probability density function, $\rho(\boldsymbol{\xi})$, of the vector $\boldsymbol{\xi}$, which contains all the random variables used to describe the sources of uncertainty.

Once the sources of uncertainty are quantified, the main focus is on quantifying the propagation of these uncertainties through a system or model of interest. In general, the main interest is on the effect of uncertainties on some functional $\mathcal{J}$ of the system or model; this functional is also known as a cost function. Under the probability theory framework, there are several methods for uncertainty propagation that are discussed in the next section.

The end product of the uncertainty quantification process is a quantitative description of the probable values of the cost function, $\mathcal{J}$. It is a result of the combination of our knowledge of the uncertainty sources and the behavior of the cost function with respect to these sources. In the probabilistic framework, this quantitative description is expressed by a probability density function of the cost function, $\rho(\mathcal{J})$. This distribution function allows decision making based on risk analysis.

2.2 Methods for propagating uncertainty

As mentioned above, uncertainty quantification involves two stages. The first stage comprises the determination and quantification of uncertainty sources, denoted here by a vector containing "d" random parameters, $\boldsymbol{\xi} = (\xi_1, \ldots, \xi_d)$. The outcome of such as process is a joint probability density function $\rho(\boldsymbol{\xi})$. The second stages involves the propagation of the random parameters through the cost function $\mathcal{J}$. The outcome of this process can be statistical moments or more generally, a probability density function $\rho(\mathcal{J})$. Several approaches for uncertainty propagation have been developed. The most common approaches are sampling methods, local-based expansion methods, and integration-bases methods. More recently, stochastic expansions have been introduced as uncertainty propagation methods. These methods are described next.

2.2.1 Local expansion-based methods

The local expansion-based methods, also known as perturbation methods in engineering mechanics, are a class of uncertainty propagation methods that consists of expanding all the random parameters around their respective mean values by Taylor expansion series. Mathematical simplicity is the great advantage of these methods, which make s them the most widely used technique for analyzing random systems in engineering [42]. Non-intrusively, the method specifically consists of using sensitivity information of the output of interest with respect to the stochastic variables to approximate statistical moments.

Consider the second-order Taylor approximation of a multi-variate function $\mathcal{J}$ at the mean value $\overline{\boldsymbol{\xi}}$:

$$
\begin{aligned}
\mathcal{J}(\boldsymbol{\xi}) \;=\; & \mathcal{J}(\overline{\boldsymbol{\xi}}) + \frac{1}{2}\sum \left.\frac{\partial \mathcal{J}}{\partial \xi_i}\right|_{\overline{\boldsymbol{\xi}}} (\xi_i - \overline{\xi}_i) \\
& + \frac{1}{2}\sum\sum \left.\frac{\partial^2 \mathcal{J}}{\partial \xi_i\,\partial \xi_j}\right|_{\overline{\boldsymbol{\xi}}} (\xi_i - \overline{\xi}_i)(\xi_j - \overline{\xi}_j),
\end{aligned}
\tag{1}
$$

where $\bar{\xi}_i$ is the mean value of the "i-th" random variable. A central assumption of this approach is that the random variables contained in the vector $\boldsymbol{\xi}$ are uncorrelated. By applying this assumption and the definition of expectation; the mean and variance are:

$$
\begin{aligned}
\mu_{\mathcal{J}} &= \int_{\Gamma} \mathcal{J}(\boldsymbol{\xi})\rho(\boldsymbol{\xi})d\boldsymbol{\xi} \\
\sigma_{\mathcal{J}}^2 &= \int_{\Gamma} \left[\mathcal{J}(\boldsymbol{\xi}) - \mathcal{J}(\bar{\boldsymbol{\xi}})\right]^2 \rho(\boldsymbol{\xi})d\boldsymbol{\xi},
\end{aligned}
\tag{2}
$$

where $\rho(\boldsymbol{\xi})$ is the joint probability density function and Γ the space of the random variables. The first two statistical moments become:

$$
\mu_{\mathcal{J}} = \mathcal{J}(\bar{\boldsymbol{\xi}}) + \frac{1}{2}\sum \left(\left.\frac{\partial^2 \mathcal{J}}{\partial \xi_i^2}\right|_{\bar{\boldsymbol{\xi}}}\right)\sigma_{\xi_i}^2
\tag{3}
$$

$$
\sigma_{\mathcal{J}}^2 = \sum \left(\left.\frac{\partial \mathcal{J}}{\partial \xi_i}\right|_{\bar{\boldsymbol{\xi}}}\right)^2 \sigma_{\xi_i}^2 + \frac{1}{2}\sum\sum \left(\left.\frac{\partial^2 \mathcal{J}}{\partial \xi_i \, \partial \xi_j}\right|_{\bar{\boldsymbol{\xi}}}\right)^2 \sigma_{\xi_i}^2 \sigma_{\xi_j}^2.
\tag{4}
$$

Equations 3 and 4 are also known as the moment method. This method is also categorized by the number of terms used in the first two statistical moments. For instance, by using only the first term, the first order first moment (FOFM), and first order second moment (FOSM) methods are defined for the mean and variance, respectively. Alternatively, if all terms of equations 3 and 4 are considered, the second order first moment (SOFM), and the second order second moment (SOSM) methods are defined for the mean and variance, respectively. Note that the previous equations only require information of the first two statistical moments of the uncertain inputs, $\boldsymbol{\xi}$, to approximate the first two moments of the system output $\mathcal{J}$ [6]. This differs from other methods, which require information of the probability density function of the uncertain inputs ξ.

The main advantage of these methods is the low computational cost. This cost depends mostly on the available methods for the calculation of the derivatives. The most common approach for derivative calculation is finite difference. More recently, automatic differentiation and adjoint approaches have been applied [104, 2] in order

to exploit their low cost in approximating sensitivity information, especially for large number of variables. Because of the low computational cost, local expansion-based methods have extensively been used in robust design; see for instance [52, 58, 91, 92, 57, 59, 104].

Despite the appealing simplicity of local expansion-based methods, their applicability is limited to small degrees of randomness of the input parameters and low degree of non-linearity of the system output. Equations 3 and 4 yield good approximations of the moments if the function $\mathcal{J}$ is approximately linear for the entire range of values of $\boldsymbol{\xi}$ [53]. Furthermore, if the function is nonlinear the above equations are only adequate for small values of variance of $\boldsymbol{\xi}$ [6]. This is because of the local validity of the Taylor expansion [42]. An alternative method to improve the accuracy is to consider higher order Taylor expansion terms such as second order terms. However, high order derivatives do not guarantee a better approximation [43] since the method validity is still local. These restrictions are a major barrier when dealing with more general problems such those that involve highly non-linear system outputs and large degrees of uncertainties.

2.2.2 Sampling methods

Sampling methods are another common type of uncertainty propagation. In this category, the Monte Carlo (MC) and quasi-Monte Carlo (quasi-MC) methods are found. In MC methods, a sequence $\boldsymbol{\xi}^1, \boldsymbol{\xi}^2, \dots, \boldsymbol{\xi}^N$ of the random vector $\boldsymbol{\xi}$ is generated according to the joint probability density function of the input random variables $\rho(\boldsymbol{\xi})$. Then, simulations are performed for each sample point to obtain the cost function $\mathcal{J}(\boldsymbol{\xi}^i)$. The first two moments are calculated according to

$$\mu_{\mathcal{J}} = \frac{1}{N} \sum_{i=1}^{N} \mathcal{J}(\boldsymbol{\xi}^i) \tag{5}$$

$$\sigma_{\mathcal{J}}^2 = \frac{1}{N-1} \sum_{i=1}^{N} \left[\mathcal{J}(\boldsymbol{\xi}^i) - \mu_{\mathcal{J}} \right]^2. \tag{6}$$

Furthermore, the probability density function $\rho(\mathcal{J})$ is approximately obtained by calculating the histogram of the cost function given a sufficiently large sample sequence.

There are several advantages of the Monte Carlo methods. Simplicity in their implementation is one of them. They only involve: a sampling method such as acceptance-rejection method for the generation of the sequence, the execution of the simulations, and finally the calculation of the statistics. Another advantage is robustness since there are not underlying assumptions of the cost function such as smoothness and locality. A third advantage is that the MC methods are insensitive to the number of random variables, i.e. size of the vector $\boldsymbol{\xi}$. Therefore, they not suffer of the so-called "curse of dimensionality." The last advantage is the potential parallelization of the method due to the independence of the sample sequence.

The main drawback of the Monte Carlo methods is, however, their slow convergence rate. The accuracy as a function of the sample size scales as $\mathcal{O}(N^{-1/2})$. Although this has no dimensionality influence, the convergence rate is extremely low and the method requires very large samples to achieve high accuracy. For instance, a factor of 4 increase in the computational cost is needed to improve the accuracy only by a factor of 2. As a result, the computational cost of the Monte Carlo method can easily become prohibited.

An improvement on the convergence rate can be obtained by quasi-Monte Carlo methods. These methods use low-discrepancy (also known as quasi-random) sequences instead of the random or pseudo-random sequences of the Monte Carlo method. In low-discrepancy sequences, the elements of a sequence are correlated to make them more uniform than random sequences [18]. As a result, quasi-Monte

17

Carlo methods exhibit an accuracy $\mathcal{O}(N^{-1}(logN)^d)$, where d is the dimension of $\boldsymbol{\xi}$. This improves the accuracy of the MC method by almost a square. However, since the dimension affects the accuracy through the logarithmic term, quasi-Monte Carlo methods are better suitable for problem with low to medium dimensionality.

2.2.3 Numerical integration-based methods

A third class of uncertainty propagation methods calculates statistical moments by direct numerical integration, using appropriate quadrature formulas. The simplest general technique for approximating multidimensional integrals is through product rule of one-dimensional quadrature rules. There are several choices for the quadrature such as Gaussian, Clenshaw-Curtis, Gaus-Patterson. By applying a tensor product formulation, the two first statistical moment are calculated according to

$$\mu_{\mathcal{J}} = \sum_{i_1=1}^{m_{i_1}} w_{i_1}^1 \ldots \sum_{i_d=1}^{m_{i_d}} w_{i_d}^d \, \mathcal{J}(\xi_{i_1}^1, \ldots, \xi_{i_d}^d) \tag{7}$$

$$\sigma_{\mathcal{J}} = \sum_{i_1=1}^{m_{i_1}} w_{i_1}^1 \ldots \sum_{i_n=1}^{m_{i_d}} w_{i_d}^d \left[\mathcal{J}(\xi_{i_1}^{i_1}, \ldots, \xi_{i_d}^d) - \mu_{\mathcal{J}} \right]^2, \tag{8}$$

where $w_{i_k}^k$, $k = 1, \ldots, d$ are the weights of the one-dimensional quadrature rule and m_{i_k} is the number of nodes of the quadrature in the kth direction.

The main advantage of these methods is that well developed one-dimensional quadrature approaches for integration can be used. The total number of function evaluations is $m = \prod_{k=1}^{d} m_{i_k}$; consequently, this number grows exponentially with the number of dimensions. Therefore, the main disadvantage of these methods is that they also suffer from the curse of dimensionality due primarily to the full product tensor approach.

2.2.4 Stochastic expansion-based methods

Another class of methods was originally developed to solve stochastic partial differential equations (SPDE). These methods address equations with stochastic inputs and

are mainly applied to computational physics problems. In this field, the stochastic Galerkin methods employ polynomial chaos expansions to represent the solution and inputs to stochastic differential equations [42]. This procedure leads to a set of new coupled partial differential equations derived from the original governing equation. These methods have shown exponential convergence and shown to be far more efficient than sampling based methods. Unfortunately, for design under uncertainty, the intrusiveness of the stochastic Galerkin method stands as the main limitation since the derived set of differential equations require efficient and robust solvers and thus modification of existing of deterministic solvers.

Non-intrusive approaches based on stochastic expansion have also been developed. The first one is a variant of the generalized polynomial chaos named the non-intrusive polynomial chaos [71] and the other one is the stochastic collocation method [76, 110]. These methods will be extensively used in this work and thus detailed explanations are postponed until later chapters .

2.2.5 Other approaches

In order to obtain low cost methods for propagating uncertainty, several other approaches that combine elements of the above mentioned methods have been proposed. A brief explanation of the most relevant method concerning the present work are given here.

2.2.5.1 Univariate dimension-reduction method

The univariate reduction method (UDR) [95] approximates a multivariate function with a linear combination of univariate functions. This process is then used to calculate multivariate statistical moments by numerical integration.

The UDR method considers the following approximation for multivariate functions

$$
\begin{aligned}
\mathcal{J}(\boldsymbol{\xi}) &= \sum_{i=1}^{d} \mathcal{J}(\overline{\xi}_1, \ldots, \xi_i, \ldots \overline{\xi}_d) - (d-1)\,\mathcal{J}(\overline{\xi}_1, \ldots, \overline{\xi}_d) \\
&= \sum_{i=1}^{d} \mathcal{J}_i(\xi_i) - (d-1)\,\mathcal{J}(\overline{\boldsymbol{\xi}}),
\end{aligned} \tag{9}
$$

where $\overline{\xi}_i$ is the mean value of the "i-th" random variable, and $\overline{\boldsymbol{\xi}}$ is a vector composed of the mean values of each of the random variables. Assuming independence of the random variables, UDR can be applied to statistical moment calculations as follows:

$$
E[\mathcal{J}^k(\boldsymbol{\xi})] = E\left[\left(\sum_{i=1}^{d} \mathcal{J}_i(\xi_i) - (d-1)\,\mathcal{J}(\overline{\boldsymbol{\xi}})\right)^k\right] \tag{10}
$$

The aforementioned decomposition allows calculation of multivariate moments in terms of moments of univariate functions, and thus a recursive formula is given in reference [95]. In general, any one-dimensional quadrature method can be used for calculating the univariate moments. The computational cost depends on the number of quadrature points taken on the one-dimensional integration and is usually $(m-1)d + 1$, where m is the number of quadrature points. If fewer points are considered in the quadrature, say 2 or 3, this method leads to a computational cost similar to local expansion methods. Thus, in simple cases, UDR can provide good accuracy at low cost.

There has been recent interest in this method due to its low cost and improved accuracy compared to local expansion methods; see for instance [85]. However, this method is restricted to multivariate functions that have very weak interaction effects between their variables. If more significant interaction effects are present, this method will certainly become inaccurate. In such scenarios, more general decomposition such as high-dimensional model representations (HDMR) [93, 94, 72] should be considered. As a matter of fact, the decomposition proposed in the UDR formulation is identical to the first order terms of the cut-HDMR decomposition. HDMR is a model for

capturing high dimensional input-output system behavior. This model represents the output of a multivariate function as a function expansion that results from a hierarchical correlated decomposition in terms of the input variables. The model is composed of $d+1$ groups of terms, where d is the dimensionality of the multivariate function. Every group represents the order of the expansion, for instance the ith-group of terms express the effect of the i variables acting on the output. According to this, the first-order terms represent the effect of single variables acting alone, the second-order terms represent the effect on the output by variables acting pairwise, and so on. According to HDMR theory, it is known that only the first order terms are not always enough to represent accurately a multivariate function; however, when developing such a family of methods, the idea was that physical systems involving multivariate function could be well represented by lower order terms, and thus avoiding the high cost in which multivariate functions can incur.

2.3   Design under uncertainty formulations

A design process that accounts for random variability is known as a design under uncertainty. The two major classes of design formulations that consider uncertainty are robust design and reliability-based design [113]. The purpose of robust design is to obtain designs that are relatively insensitive to small changes in the uncertain quantities so they perform as intended over their life cycles. In reliability-based design, given some uncertain parameters affecting responses, the main goal is to obtain design whose probability of failure is lower than some small value. Although robust and reliability-based design can follow similar mathematical formulations, the main difference is the design scenario [58].

The domain of application of these two approaches is shown in figure 1. Their applicability strongly depends on the frequency and the impact of the events. It is clear that no system is viable if variations in a regular basis can lead to catastrophe.
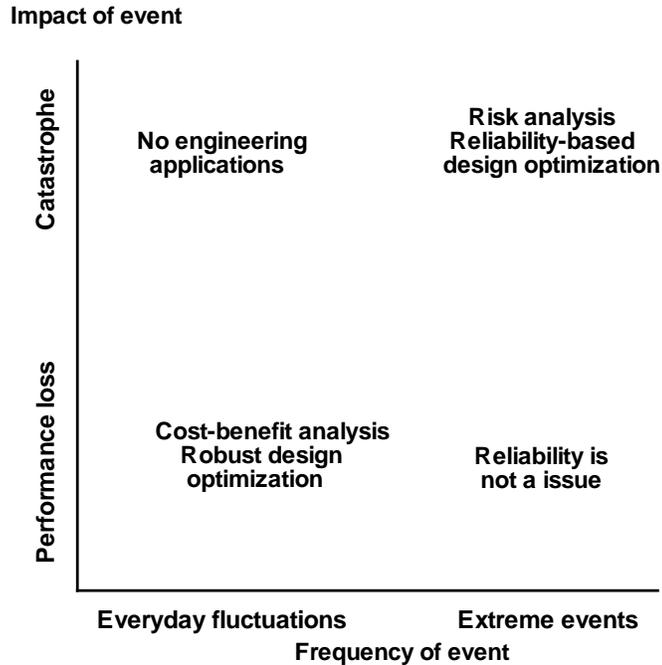
Figure 1: Uncertainty-based design domains

On the contrary, systems are preferable to be design so they are insensitive (robust) to frequent variations. In case of extreme events, it is desirable to minimize the possibility of their occurrence. This is the domain of reliability-based design.

Robust and reliability-based design are described in more detail.

2.3.1 Robust design

A robust design is a product or process whose performance does not suffer unacceptable degradation if exposed to variation due to manufacturing process, usage conditions, or design specifications. This concept can be observed in figure 2 which contrasts robust and deterministic designs [86]. The objective function exhibits a global optimum which is shown on the left side of the plot. This would be the solution if the problem if treated as a deterministic optimization. At that point, however, the objective function can vary drastically with small changes in the design variable. Therefore, the design at that point is not robust. If the variation of the design variables is considered, it is clear that the point shown on the right side is a better design

from robustness perspective.

The origins of robust design are attributed to Taguchi [105, 88], who understood quality as a minimization of the statistical variation of performance. This notion of quality has to be included in the product design, and not in later stages such as operation.
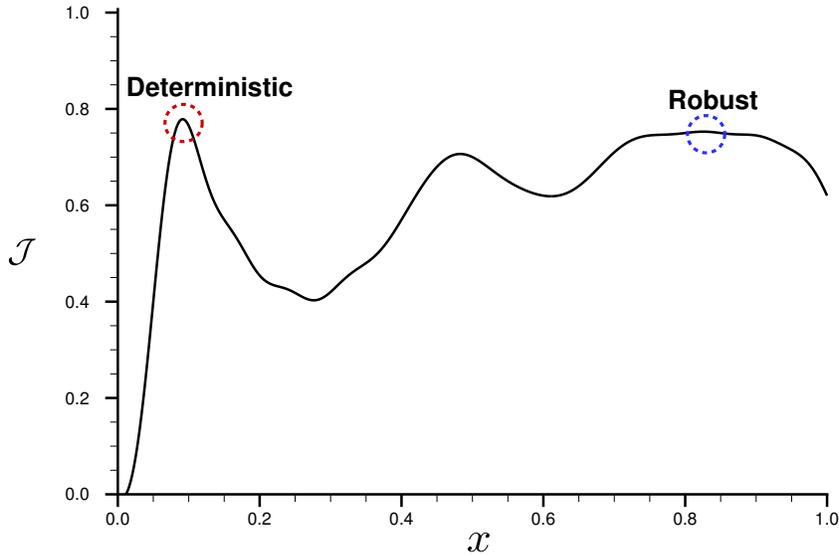
Figure 2: Robustness of the objective function

Since its introduction, robust design has been subject to many improvements. The concept was extended to simulation-based design and improved to exploit non-linear constrained optimization techniques [86]. Conceptually, robust design is classified in three types [4]. The first type identifies design variables that satisfy a set of performance requirement targets despite variations in noise factors. The second type of robust design identifies design variables values that satisfy a set of performance requirement targets despite the variation in the design variables themselves. For instance, design variable values may change during the course of the design process, so the goal is to find values that have the least impact on the system performance. A third type of robust design identifies adjustable ranges for design variables that

satisfy a a set of performance requirements targets and are insensitive to variability within the system model. In practice, robust design of the first type is commonly found. The second type has also been studied [78], but to a lesser extent.

Several methods for robust optimization have been developed; for instance, see references [4, 86]. Among them, one method for achieving robustness is to minimize the mean and standard deviation of the cost function of interest. Therefore, the optimization problem can be formulated as a multi-objective optimization problem:

$$\text{Minimize} \quad \boldsymbol{F} \quad = \quad [\,-\mu_{\mathcal{J}}\,,\,\sigma_{\mathcal{J}}\,]^T \tag{11}$$

$$\text{Subject to}$$

$$\mathcal{P}[\,g_i(\,\boldsymbol{X},\boldsymbol{\xi}\,) \leq 0)\,] \quad \geq \quad p_i, \quad i = 1,\ldots,r \tag{12}$$

$$\boldsymbol{X}_l \leq \quad \boldsymbol{X} \quad \leq \boldsymbol{X}_u$$

where $\mathcal{J}$ is the cost function, and $\boldsymbol{X}$ is the vector of design variables. The inequality constraint for g_i expresses that all constrain must be satisfied regardless of the noise in the design variables.

2.3.2 Reliability design optimization

Reliability-based design are similar to robust design, but have a different focus. Methods for reliability optimization are based on the assumption that the design space is divided in regions of success and failure. In reliability analysis, system failure conditions are expressed by limit state functions. These functions are usually non-linear relationship of the type $g(\boldsymbol{\xi}) = 0$, where $\boldsymbol{\xi}$ is a vector containing the uncertain parameters with known statistics. This equation divides the uncertain space in regions of safety and failure. Conventionally, the failure domain is described by $g(\boldsymbol{\xi}) \leq 0$. This situation is illustrated in fig. 3 for a problem involving two uncertain parameters.

Therefore, the main purpose of reliability analysis is the development of methods
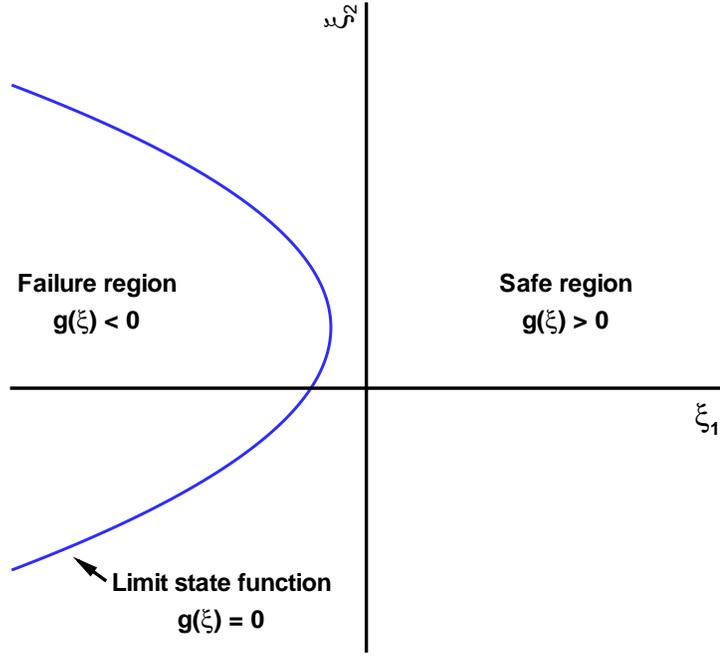
Figure 3: Reliability regions and limit state function

for calculating the probability that $g(\boldsymbol{\xi}) \leq 0$

$$\mathcal{P}[\,g(\boldsymbol{\xi}) \leq 0\,] = \int_{g(\boldsymbol{\xi}) \leq 0} \rho(\boldsymbol{\xi})\,d\boldsymbol{\xi}, \tag{13}$$

where $\rho(\boldsymbol{\xi})$ is the joint probability of the uncertain parameters.

Optimization for reliability methods are based on these safety and failure regions. The main goal is to find the best design that is sufficiently far from the failure region. Mathematically, this can be expressed as a small probability of failure. Then, the optimization problem can the be formulated as follows:

$$\text{Minimize} \qquad \mathcal{F}[\mathcal{J}(\,\boldsymbol{X},\boldsymbol{\xi}\,)] \tag{14}$$

$$\text{Subject to}$$

$$\mathcal{P}[\,g_i(\boldsymbol{X},\boldsymbol{\xi}\,) \leq 0\,] \quad \leq \quad R_{g_i}, \quad i = 1,\ldots,r.$$

25

$\mathcal{F}$ is the objective function which can be a function of the mean and standard deviation of the cost function $\mathcal{J}$. The uncertain parameter, R_{g_i} is the reliability target for the ith constraint. Equation 14 involves calculations of the probability that every constraint is less than the specified target for a particular design vector $\boldsymbol{X}$. Therefore, most of the effort resides on the accurate calculation of these tail probabilities. In practice, the first order reliability method (FORM) and the second order reliability method (SORM) are popular choices for reliability optimization due to the high computational cost incurred by calculating failure probabilities.

This chapter has summarized existing methods for uncertainty propagation methods as well as robust and reliability-based design. The discussion now focus on one particular uncertainty propagation method - stochastic expansion. This method will be applied to robust design.

CHAPTER III

STOCHASTIC EXPANSIONS

The uncertainty propagation methods reviewed in Chapter II are based in classical methods for evaluating predictions such as statistical moments of a quantity of interest or the probability of particular events. The application of these methods is limited by more or less restrictive assumptions, such as variability of the uncertain parameters ($\boldsymbol{\xi}$) or linearity of the cost function ($\mathcal{J}$). However, for more general problems in which the variability and number of uncertain parameters are large and the cost function can be highly nonlinear, the main obstacle of propagating uncertainties is the computational cost.

The main purpose of this chapter is to provide insight on one particular type of uncertainty propagation methods – stochastic expansions – that provides a balance between accuracy and computational cost. Stochastic expansions can be classified as intrusive or nonintrusive. The former acts directly on the governing equations of a physical system, and thus requires modification of existing solvers or development of new solvers. However, the latter acts on the output of the governing equations system; therefore, it allows the use of existing deterministic codes. Even though the emphasis of this thesis is on nonintrusive methods, the basic formulation of intrusive methods is also reviewed. The purpose is to explain the mathematical formulation of the nonintrusive polynomial chaos, which is the main focus for uncertainty propagation in the present work.

3.1 Background

Stochastic expansion is a more recent alternative for uncertainty propagation and consists in representing the solution u by a functional representation of the random

variables expansions of the type

$$\hat{u}\left(\boldsymbol{x},t,\omega\right)=\sum_{i=0}^{P}\alpha_i\left(\boldsymbol{x},t,\boldsymbol{\xi}\right)\Phi_i(\boldsymbol{\xi}), \qquad (15)$$

where $\hat{u}$ is the dependent random quantity, α_i are the expansion coefficients, and Φ_i are the basis functions. The ω denotes the random dependence on random input parameter $\boldsymbol{\xi}$. Such functional expansions are known as stochastic expansions. Since the introduction of the stochastic Galerkin method by Ghanem and Spanos [42] in which the Hermite polynomial chaos expansion is used to model uncertainty propagation in solid mechanics, stochastic expansion methods have been under development and scrutiny, mostly for solving stochastic partial differential equations (SPDE). The stochastic expansion methods mostly differ from each other based only on the choice of the basis functions, and by the definition of the coefficients of the expansion.

One type of functional representations is based on the generalized polynomial chaos (gPC) expansion. The polynomial chaos is based on the work of Wiener on homogeneous chaos [108] and it is essentially a spectral representation in random space. The term *chaos* as used by Wiener refers to randomness, and it has no relationship with the concept of chaos theory of non-linear dynamical systems. Uncertainty propagation methods based on this type of expansion have been developed both in the global context, employing spectral expansions spanning all the stochastic space, and in a local context, using localized spectral representations. In both cases, uncertainty is represented by a gPC expansion through a model by using the stochastic Galerkin projection to reformulate the governing equations into equations for the gPC coefficients, or by using numerical evaluations of the gPC coefficients of the model outputs employing solutions of the deterministic model. The former is also known as intrusive approaches because the original governing equations are reformulated requiring development of a new solver or modification of the original one. The latter has been named nonintrusive as the original code can be treated as a black box. The advantage of the intrusive gPC expansion is that directly finds the gPC representation of model

outputs by a one-time solution of the reformulated model. Conversely, the advantage of the nonintrusive method is the ability of using already well developed codes.

A second stochastic expansion method is the stochastic collocation (SC) method [76, 110]. Similarly to the gPC based uncertainty propagation method, exponential convergence rates can be achieved for statistical moments of interest. The main difference, however, is that unlike the gPC approach which estimates coefficients for known basis functions, SC uses interpolating functions for known coefficients. This formulation leads to a set of uncouple system of the governing equation, and thus the SC formulation is nonintrusive. In this chapter, a brief review of these methods is given.

3.2 *Mathematical Preliminaries*

Consider the following partial differential equation with random input parameters $\boldsymbol{\xi}$ given by

$$\mathcal{L}\left(\boldsymbol{x}, t, \boldsymbol{\xi}; u\right) = f\left(\boldsymbol{x}, t, \boldsymbol{\xi}\right), \quad \boldsymbol{x} \in \mathrm{D}, \tag{16}$$

subject to the boundary condition

$$\mathcal{B}\left(\boldsymbol{x}, u\right) = g(\boldsymbol{x}), \quad \boldsymbol{x} \in \partial \mathrm{D}, \tag{17}$$

defined in a physical domain $D \subset \mathbb{R}^d$, $d = 1, 2, 3$, with boundary ∂D, and $\boldsymbol{x} = (x_1, \ldots, x_d)$ as the space coordinates. In the previous equations, $u = u\left(\boldsymbol{x}, t, \omega\right)$ is the solution, and $\mathcal{L}$ is a general differential operator that may contain spatial or time derivatives as well as linear and non-linear terms. $\mathcal{B}$ is a boundary operator and, in general, can be stochastic. This operator can adopt different forms in various boundaries, for instance, $\mathcal{B} = I$, where I is the identity operator for Dirichlet boundaries, or $\mathcal{B} = n.\nabla$ for Neumann boundaries. The terms f and g are source terms which, in general, can be random as well. The vector $\boldsymbol{\xi}$ containing random parameters represents uncertainty in the system due to equation parameters, initial conditions, boundary

conditions, or even the physical domain. Due to the dependence on random parameters, the solution u is regarded as a random process and can be represented by the functional representation shown in equation 15.

The vector $\boldsymbol{\xi} = (\xi_1, \ldots, \xi_d) \in \mathbb{R}^d$ containing the uncertain parameters will be modeled by the probabilistic framework. It is assumed that the components $(\xi_i, i = 1, \ldots, d)$ of this d-variate random vector are random variables that are mutually independent of each other with probability density function $\rho_i : \Gamma_i \to \mathbb{R}^+$, where Γ_i is the support of the random parameter i. As a result, the joint probability density function of the random vector $\boldsymbol{\xi}$ is expressed as

$$\rho(\boldsymbol{\xi}) = \prod_{i=1}^{d} \rho_i(\xi_i),$$

with support

$$\Gamma = \prod_{i=1}^{d} \Gamma_i \subset \mathbb{R}^d.$$

The general procedure of solving the stochastic differential equation (Eq.16) starts by approximating the solution u by stochastic expansion (Eq.15), and then substituting it into the stochastic differential equation

$$\mathcal{L}\left(\boldsymbol{x}, t, \boldsymbol{\xi}; \sum_{i=0}^{P} \alpha_i \, \Phi_i\right) = f\left(\boldsymbol{x}, t, \boldsymbol{\xi}\right). \tag{18}$$

Next, a stochastic Galerkin projection of the above equation onto each basis Φ_k is then carried out

$$\left\langle \mathcal{L}\left(\boldsymbol{x}, t, \boldsymbol{\xi}; \sum_{i=0}^{P} \alpha_i \, \Phi_i\right), \Phi_k \right\rangle = \left\langle f\left(\boldsymbol{x}, t, \boldsymbol{\xi}\right), \Phi_k \right\rangle, \quad k = 0, 1, \ldots, P, \tag{19}$$

where $\langle \cdot, \cdot \rangle$ denotes the inner product in the Hilbert space of the variables $\boldsymbol{\xi}$ and is defined by

$$\langle g, h \rangle = \int_{\Gamma} g \, h \, W(\boldsymbol{\xi}) \, d\boldsymbol{\xi}. \tag{20}$$

In the above equation, $W(\boldsymbol{\xi})$ is the weighting function and it is identical to the joint probability density function of the random parameters, i.e. $W(\boldsymbol{\xi}) = \rho(\boldsymbol{\xi})$.

In general, Equation 19 defines an implicit system of partial differential equations describing the evolution of the expansion coefficients α_i. The solution method for the aforementioned system depends greatly on the choice of the basis function of the expansion. The main three families of methods for the solution of the stochastic differential equations are then reviewed.

3.3   *Stochastic Galerkin method*

In the stochastic Galerkin method [42] also known as the intrusive polynomial chaos, the functional expansion is a spectral expansion of suitable orthogonal eigenfunctions with weights associated with a particular density function. Following the work of Wiener [108], this spectral expansion is generally referred as the polynomial chaos expansion.

In general, the polynomial chaos expansion are defined in terms of the expansion coefficients α_i that are spectral (deterministic) coefficients, and a given basis of functions, $\{\Phi_i(\boldsymbol{\zeta})\}_{i=0}^{\infty}$, which are usually a set of multi-dimensional polynomials. These multivariate polynomials have the property of being orthogonal with respect to the probability density function ρ, satisfying the following orthogonality relation

$$\langle \Phi_i, \Phi_j \rangle = \langle \Phi_i^2 \rangle \, \delta_{ij} = \int_{\Gamma} \Phi_i(\boldsymbol{\zeta}) \, \Phi_j(\boldsymbol{\zeta}) \, \rho(\boldsymbol{\zeta}) \, d\boldsymbol{\zeta}, \tag{21}$$

where δ_{ij} is the Kronecker delta and $\langle \cdot, \cdot \rangle$ denotes the ensemble average that is the inner product in the Hilbert space determined by the measure of the random variables. Therefore, the type of the orthogonal polynomial Φ is determined by the type of the probability density function. For instance, Gaussian distributions are approximated by Hermite polynomials [42]. Other types of distributions, e.g. uniform and beta, are approximated by Legendre and Jacobi polynomials [112], respectively. Furthermore, these expansions have an infinite number of terms; in practice, however, the expansion is truncated to a finite number of terms.

By applying a polynomial chaos expansion to the stochastic Galerkin approximation of the differential equation (Eq. 19), a fully- coupled system of $P+1$ differential equations for the expansion coefficients α_i is obtained.

$$\left\langle \mathcal{L}\left(\boldsymbol{x}, t, \boldsymbol{\xi}; \sum_{i=0}^{P} \alpha_i \Phi_i\right), \Phi_k \right\rangle = \left\langle f(\boldsymbol{x}, t, \boldsymbol{\xi}), \Phi_k \right\rangle, \quad k = 0, \ldots, P. \tag{22}$$

This resulting system should further be solved in space and time using proper numerical methods for the solution of PDE's. This in turn requires the development or modification of solvers to handle this new larger system of differential equations.

The stochastic Galerkin method was introduced by Ghanem and Spanos [42] for modeling uncertainty propagation in solid mechanics. A Hermite polynomial chaos [108] expansion was used in order to model Gaussian random variables. The method was then extended to other types of random variables by Xiu *et al.* [112]. A more general group of polynomial known as the Askey family [7] were used in order to model other types of random variables. The stochastic Galerkin methods have shown to have exponential rate of convergence at fraction of the cost of sampling methods.

Since its introduction, intrusive polynomial chaos expansion based methods have been subject of research in computational fluid dynamics. Applications range from flow in porous media, thermofluids, and incompressible and compressible flow. Ghanem and Dham [41] showed the first application of the intrusive polynomial chaos expansion method to uncertain porous media by simulating the transport of water and oil in aquifer with uncertain spatial distribution of permeability. Le Maître *et al.* [70] studied the use of intrusive polynomial chaos to incompressible laminar flow at moderate Reynolds numbers for two dimensional channel flow with uncertain temperature-dependent viscosity.

Unlike incompressible flow simulation in which intrusive polynomial chaos method have been successfully applied, application to compressible flows have shown to be more challenging. Several authors [20, 19] have pointed out the method limitation when the uncertain variables lead to discontinuities in the flowfield. Supersonic nozzle

32

flows with uncertain in inlet conditions and geometry was studied by Mathelin *et al.* [76, 20]. Other canonical problems was studied as well. Lin *et al.* [73] studied supersonic flows over wedges with uncertain inflow conditions and wedge apex. In order to account for discontinuities, the multi-element generalized polynomial chaos was introduced. More recently, Poëtte [90] applied the polynomial chaos method along with decomposition of the entropic variable of the flow. This technique does not require special discretization techniques of the random space.

Other limitations of the stochastic Galerkin method have been highlighted, see for instance [25], [8]. Convergence behavior deterioration for long term integration in transient problems, difficulty in representing of nonpolynomial functions, large truncation error in high-order polynomials, and intrusiveness are the main problems of these approaches and are still subject of further research in the field of computational physics. For more general engineering problems, intrusiveness is certainly the main drawback of these type of methods. The necessity of solving larger fully couple systems of differential equations traduces on modification of current solvers or development of new solvers. This in practice can be very cumbersome and it does not allow to take advantage of specialize current solvers such as legacy codes. Therefore, the main focus in the present work is in non-intrusive methods.

3.3.1 Example - one dimensional uncertain transient heat conduction

The procedure of representing and solving stochastic differential equations by the stochastic Galerkin method is illustrated by an example of an one-dimensional transient heat condition with uncertain thermal conductivity. The equation governing heat conduction is

$$\frac{\partial T}{\partial t} - k \frac{\partial^2 T}{\partial x^2} = 0, \tag{23}$$

where the temperature $T = T(x, t; \xi)$, and $k = k(\xi)$ is the thermal conductivity which is a random variable. The main purpose is to find the probabilistic behavior of T

based on the probabilistic behavior of k.

According to equation 16, the differential operator $\mathcal{L}$ and the driving term f are then defined as

$$
\mathcal{L}(x, t, \xi; T) = \frac{\partial T}{\partial t} - k(\xi) \frac{\partial^2 T}{\partial x^2}
$$

$$
f(x, t, \xi; T) = 0.
$$

By using the polynomial chaos expansion, the thermal conductivity k, and the temperature T are represented by random processes according to

$$
k(\xi) = \sum_{i=0}^{P} \beta_i \, \Phi_i(\zeta) \tag{24}
$$

$$
T(x, t; \xi) = \sum_{i=0}^{P} \alpha_i(t, x) \, \Phi_i(\zeta), \tag{25}
$$

where ξ is the random dimension, and $\xi = \xi(\zeta)$ is a standard random variable. These expansions are then substituted into the governing Equation 23, so the following expression is obtained

$$
\frac{\partial}{\partial t} \sum_{i=0}^{P} \alpha_i(t, x) \, \Phi_i(\zeta) - \sum_{i=0}^{P} \beta_i \, \Phi_i(\zeta) \frac{\partial^2}{\partial x^2} \sum_{i=0}^{P} \alpha_i(t, x) \, \Phi_i(\zeta) = 0.
$$

The stochastic Galerkin projection (eq. 19) of the above equation onto the polynomial chaos basis can then be written as follow

$$
\left\langle \frac{\partial}{\partial t} \sum_{i=0}^{P} \alpha_i(t, x) \, \Phi_i - \sum_{i=0}^{P} \beta_i \, \Phi_i \frac{\partial^2}{\partial x^2} \sum_{i=0}^{P} \alpha_i(t, x) \, \Phi_i \, , \, \Phi_k \right\rangle = 0, \quad k = 0, \ldots, P,
$$

Since the polynomial chaos basis Φ is not function of space and time, the previous equation is then re-written as

$$
\left\langle \sum_{i=0}^{P} \Phi_i \frac{\partial}{\partial t} \alpha_i(t, x) - \sum_{j=0}^{P} \beta_j \, \Phi_j \sum_{i=0}^{P} \Phi_i \frac{\partial^2}{\partial x^2} \alpha_i(t, x) \, , \, \Phi_k \right\rangle = 0, \quad k = 0, \ldots, P.
$$

Rearranging and taking the projection to every term of the differential operator

$$
\sum_{i=0}^{P} \frac{\partial}{\partial t} \alpha_i(t, x) \, \langle \Phi_i, \Phi_k \rangle - \left\langle \sum_{j=0}^{P} \beta_j \, \Phi_j \sum_{i=0}^{P} \Phi_i \frac{\partial^2}{\partial x^2} \alpha_i(t, x) \, , \, \Phi_k \right\rangle = 0, \quad k = 0, \ldots, P.
$$

According to Eq. 21, the inner product in the first term can be expressed by the Kronecker delta, and the norm squared of the polynomial basis; whereas the second term can be written by a inner product of the three polynomial base.

$$\sum_{i=0}^{P} \frac{\partial}{\partial t} \alpha_i(t, x) \left\langle \Phi_i^2 \right\rangle \delta_{ik} - \sum_{i=0}^{P} \sum_{j=0}^{P} \left\langle \Phi_i \, \Phi_j, \Phi_k \right\rangle \beta_i \frac{\partial^2}{\partial x^2} \alpha_j(t, x) = 0, \quad k = 0, \ldots, P.$$

Finally, the stochastic Galerkin representation of the one-dimensional heat equation is given as

$$\left\langle \Phi_k^2 \right\rangle \frac{\partial}{\partial t} \alpha_k(t, x) - \sum_{i=0}^{P} \sum_{j=0}^{P} e_{ijk} \, \beta_i \frac{\partial^2}{\partial x^2} \alpha_j(t, x) = 0, \quad k = 0, \ldots, P, \tag{26}$$

where $e_{ijk} = \left\langle \Phi_i \, \Phi_j, \Phi_k \right\rangle$. $\left\langle \Phi_k^2 \right\rangle$ along with e_{ijk} are analytically determined by using the orthogonality property (Eq. 21). It can be noted that equation 26 defines a system of PDE's governing the evolution of the expansion coefficients α_k, $k = 0, \ldots, P$. This system has a similar form than the original governing heat equation. However, because of the coupling terms, the original equation is enlarged to a set of $P+1$ coupled partial differential equations. The coefficients β_i are known since it is assumed that a probabilistic model for the thermal conductivity is given. For instance, if the thermal conductivity has a Gaussian distribution with mean and standard deviation μ_k, and σ_k, respectively; k can be expressed by

$$k(\xi) = \sum_{i=0}^{P} \beta_i \, \Phi_i(\zeta) = \mu_k + \sigma_k \, \zeta(\xi). \tag{27}$$

By identifying terms, it is found that $\beta_0 = \mu_k$, $\beta_1 = \sigma_k$, and $\beta_i = 0$ for $i > 1$. The above equation is simply a mapping between the Gaussian random variable of the thermal conductivity and the standard Gaussian random variable of the polynomial chaos expansion. The set of PDE's (Eq. 26) still need to be solved in space and time using proper numerical methods for this larger set of equations.

Once the set of PDE's is solved, the polynomial chaos coefficients can be substituted back into the polynomial chaos expansion for the temperature $T(x, t; \omega)$ to

calculate its stochastic response. The mean temperature field can then be calculated by taking a first order expectation of the temperature expansion

$$\mu_T = E[\,T(x,t;\xi)\,] = \alpha_0. \tag{28}$$

The temperature field variance is similarly calculated

$$\sigma_T^2 = E[\,(\,T(x,t;\xi) - \mu_T\,)^2\,] = \sum_{i=1}^{P} \alpha_i^2 \, \langle \Phi_i^2 \rangle. \tag{29}$$

In this example, the stochastic Galerkin method was applied to a simple problem. The focus was to highlight the formulation of this intrusive approach and also its use in solving stochastic systems. Nonintrusive approaches are described in the next two sections.

3.4 Stochastic collocation method

In the stochastic collocation method [76], the main idea is to represent the uncertain quantity through interpolating functions in the random space. Therefore, the functional expansion is expressed in terms of multivariate interpolating basis functions. These basis functions are constructed on a set of strategically located nodes to gain accuracy and they have the property of being mutually orthogonal polynomials.

Given a set of prescribed nodes in the random space, $\Theta = \{\boldsymbol{\xi_i}\}_{i=0}^{P} \in \Gamma$, and the basis functions having the following property

$$\Phi_i\,(\boldsymbol{\xi_j}) = \delta_{ij}, \quad i,j = 0,\ldots,P, \tag{30}$$

the coefficients of the expansion are determined by the values of the dependent variables at the collocation points: $\alpha_i = u\,(\mathbf{x},\boldsymbol{\xi_i})$. With this choice of basis functions and coefficients, the functional expansion results on an interpolant for the dependent random quantity

$$\hat{u}\,(\mathbf{x},t,\omega) = \sum_{i=0}^{P} u\,(\mathbf{x},t,\boldsymbol{\xi_i})\,\Phi_i(\boldsymbol{\xi}). \tag{31}$$

By introducing the above expansion in the stochastic Garlekin approximation (eq. 19) and approximating the integrals by quadrature methods with weights w_i at the collocation points ξ_i as follow

$$\int_\Gamma \left[\mathcal{L}\left(\mathbf{x}, t, \omega; \hat{u}\right) - f\left(\mathbf{x}, t, \omega\right) \right] \Phi_k(\boldsymbol{\xi})\, \rho(\boldsymbol{\xi})\, d\boldsymbol{\xi} =$$

$$\sum_{i=0}^{P} w_i \left[\mathcal{L}\left(\mathbf{x}, t; u\left(\mathbf{x}, t, \boldsymbol{\xi_i}\right)\right) - f\left(\mathbf{x}, t, \boldsymbol{\xi_i}\right) \right] \Phi_k(\boldsymbol{\xi_i})\, \rho(\boldsymbol{\xi_i}), \quad k = 0, \ldots, P.$$

It is noted that in the previous equation $\Phi_k(\boldsymbol{\xi_i}) = \delta_{ki}$ (eq.30); therefore, the stochastic Garlekin approximation is transformed to the following relationship

$$\mathcal{L}\left(\mathbf{x}, t; u\left(\mathbf{x}, t, \boldsymbol{\xi_k}\right)\right) - f\left(\mathbf{x}, t, \boldsymbol{\xi_k}\right) = 0, \quad k = 0, \ldots, P, \tag{32}$$

which described a set of uncoupled deterministic solution of the differential equation shown in eq.16. Hence, the stochastic collocation method is equivalent to solving $P + 1$ deterministic problems at the respective collocation points $\Theta = \{\boldsymbol{\xi}_i\}_{i=0}^{P}$ in the random space.

The basis functions Φ are multivariate extensions of uni-dimensional basis functions ϕ. This is usually accomplished by using tensor product of uni-dimensional basis functions

$$\Phi_i(\boldsymbol{\xi}) = \phi^{i_1}(\xi) \times \ldots \times \phi^{i_n}(\xi) = \prod_{j=1}^{d} \phi^{i_j}(\xi).$$

The univariate polynomials are usually Lagrange polynomial basis, and more recently linear hat basis functions. Early works of stochastic collocation methods [76, 106] used tensor products of univariate quadrature as sets of collocation points. The use of full tensor quadratures, however, is restricted to small number of random inputs due to its exponential growth with dimensionality. In order to circumvent that problem, sparse grids were introduced in [110] as a mean to extend the stochastic collocation method to higher dimensions.

3.4.1 Statistical moments

Once a sufficiently accurate interpolant is defined, the SC method can be used to construct probability density function by sampling from the SC interpolant defined in eq. 31. Statistics of interest such as mean and variance can also be calculated as

$$\mu \;=\; \sum_{i=0}^{P} u\left(\mathbf{x}, \boldsymbol{\xi_i}\right) \int_{\Gamma} \Phi_i(\boldsymbol{\xi})\, \rho(\boldsymbol{\xi}) d\boldsymbol{\xi} \tag{33}$$

$$\sigma^2 \;=\; \sum_{i=0}^{P} u^2\left(\mathbf{x}, \boldsymbol{\xi_i}\right) \int_{\Gamma} \Phi_i(\boldsymbol{\xi})\, \rho(\boldsymbol{\xi}) d\boldsymbol{\xi} \;-\; \mu^2. \tag{34}$$

It should be noted that higher moments are calculated by integrating an interpolant of the function to the power of the order of the respective moment. For instance, the variance is obtained by an interpolant of the function u^2 rather than the function u.

3.5 Nonintrusive polynomial chaos

An alternative use of the polynomial chaos expansion that avoid solving set of fully couple partial differential equations as in the stochastic Galerkin method is the nonintrusive polynomial chaos also known as the nonintrusive spectral projection. The main advantage of these methods is that they can use deterministic codes as a black boxes, allowing utilization of current specialized solvers and legacy codes, and keeping exponential convergence rates.

In these approaches, the solution of a stochastic system is approximated by a polynomial chaos expansion as in the stochastic Garlekin method; however, the main idea is to obtain the spectral coefficients α_i by projecting the deterministic solution u onto the PC basis Φ. As previously shown by Ghanem [42] and Xiu [112], this is always possible given the correct basis. The first works reporting solution of stochastic systems as a function of polynomial chaos expansion by projecting deterministic outputs are those by Le Maître et al. [71] and Pettit et al. [87]. The former reports

stochastic fluid dynamic fields for natural convection in a 2D square cavity with uncertain temperature distributions at the boundaries, and the latter analyzes the effect of uncertain Young's modulus in the buckling problem of an aerolastic system.

The nonintrusive polynomial chaos or nonintrusive spectral projection differs from the stochastic Galerkin and stochastic collocation methods in that its derivation is not directly related to the stochastic Galerkin projection of a stochastic system. Nevertheless, the method can still be seen as producing a set of uncoupled differential equations.

3.5.1 Polynomial chaos (PC) basis

In the finite dimensional random space Γ defined above, the polynomial chaos expansion consist in representing a random function by using classical orthogonal basis of the random variables. In order to explain the PC basis, concepts of univariate classical orthogonal polynomial are reviewed first. Then, the univariate polynomial chaos basis is described. Finally, the multivariate basis is described.

3.5.1.1 Orthogonal polynomials

Orthogonal polynomials have a central role in representing random quantities in the polynomial chaos expansion method. Because of this, their basic properties are reviewed.

Consider $Q_n(x)$ be a polynomial of exact degree n. A system of polynomials $\{Q_n(x), n \in \mathbb{N}\}$ is orthogonal with respect to some measure μ if the following conditions is satisfied:

$$\int_{\mathcal{S}} Q_n(x) \, Q_m(x) \, d\mu = h_n^2 \, \delta_{nm}, \tag{35}$$

where $\mathcal{S}$ is the support of $Q_n(x)$, and h_n are nonzero constants. Additionally, the system is called orthonormal if $h_n = 1$. The measure μ usually has a weighting

function $w(x)$. Then, the previous equation is written as

$$\int_{\mathcal{S}} Q_n(x)\, Q_m(x)\, w(x)\, dx = h_n^2\, \delta_{nm}. \tag{36}$$

Another important property of orthogonal polynomials $Q_n(x)$ is that they satisfy a three-term recurrence relation

$$-x\, Q_n(x) = A_n\, Q_{n+1}(x) - (A_n + C_n)\, Q_n(x) + C_n\, Q_{n-1}(x), \quad n \geq 1,$$

where $A_n, C_n \neq 0$ and $C_n/A_{n-1} > 0$. By specifying $Q_{-1}(x) = 0$ and $Q_0(x) = 1$, any $Q_n(x)$ can be generated for known A_n and C_n.

In equation 36, the weighting function $w(x)$ defines the type of orthogonal polynomials $Q_n(x)$. Some polynomial types along with their respective weighting function are shown in table 1.

Table 1: Polynomial type and weighting function correspondence

Polynomial type $Q_n(x)$		weighting function $w(x)$	Support $\mathcal{S}$
Hermite	$H_n(x)$	$e^{-\frac{1}{2}x^2}$	$(-\infty,\ \infty)$
Legendre	$P_n(x)$	1	$[-1, 1]$
Laguerre	$L_n^{(\alpha)}(x)$	$x^\alpha\, e^{-x}$	$[0, \infty)$
Jacobi	$P_n^{(\alpha,\beta)}(x)$	$(1-x)^\alpha\, (1+x)^\beta$	$[-1, 1]$

It must be noted that the weighting functions have similar form of that of some standard probability density functions. For instance, the weighting function of the Hermite polynomial:

$$w(x) = e^{-\frac{1}{2}x^2},$$

and the probability density function (pdf) of standard normal random variable

$$\rho(x) = \frac{1}{\sqrt{2\,\pi}} e^{-\frac{1}{2}x^2},$$

40

only differs by a factor of $1/\sqrt{2\pi}$. Similarly, the weighting function of the Laguerre polynomial:

$$w(x) = x^\alpha\, e^{-x},$$

and the probability density function of standard gamma random variable

$$\rho(x) = \frac{x^\alpha\, e^{-x}}{\Gamma(\alpha+1)},$$

are only different by a factor $1/\Gamma(\alpha+1)$. The same holds for the Legendre and Jacobi polynomials whose weighting functions have similar form to those of the standard uniform and standard beta distribution, respectively. As it will be seen, this coincidence is very important in representing stochastic processes with the polynomial chaos expansion.

3.5.1.2   Univariate PC basis

Consider one-dimensional orthogonal polynomial basis

$$\{\, \phi_i(\zeta)\, \}_{i=0}^{p}, \tag{37}$$

where i is the chaos order, ϕ_i is the polynomial of chaos i^{th} of the PC basis, and p is the maximum chaos order. The chaos order i expresses the exact degree of the polynomial, and thus p expresses the maximum degree of the polynomial in the basis. These polynomials are then uniquely defined by a given univariate probability density function $\rho(\zeta)$ according to the orthogonality relation

$$\langle \phi_i, \phi_j \rangle = \int_\Gamma \phi_i(\zeta)\phi_j(\zeta)\rho(\zeta)\, d\zeta = \langle \phi_i^2 \rangle \delta_{ij}, \tag{38}$$

where δ_{ij} is the Kronecker delta. This orthogonal selection is optimal for the distribution type since the inner product weighting function and its corresponding support range Γ correspond to the probability density function.

Notice that the right hand side of the equation that defines the orthogonality relation of the univariate PC basis (eq. 38) is similar to the equation that defines

orthogonality property in orthogonal polynomials (eq. 36). Therefore, by adopting the same polynomials in the PC basis

$$\phi_i = Q_n$$
$$\phi_j = Q_m,$$

and by re-scaling the weighting function w so this becomes the standard probability density function

$$\rho = C\,w, \quad C > 0$$

the univariate polynomial chaos basis is determined. As a result, the univariate polynomial chaos basis is identical to the set of classical orthogonal polynomials. The type of the polynomial depends on the type of the random variable through the standard density function. For instance, Gaussian random variables require Hermite polynomial basis, and Uniform random variables require Legendre polynomial basis. Some of the polynomials-distribution function correspondence for some continuous and discrete random variables are shown in table 7 and 3. The first six polynomials ϕ_i and their corresponding norm squared $\langle \phi_i^2 \rangle$ for the Gaussian and uniform distribution are provided in tables 4 and 5, respectively

Table 2: Continuous random variable and basis correspondence

Random variable ζ	Polynomial type $\phi(\zeta)$	Support Γ
Gaussian	Hermite	$(-\infty, \infty)$
uniform	Legendre	$[-1, 1]$
gamma	Laguerre	$[0, \infty)$
beta	Jacobi	$[-1, 1]$

42

Table 3: Discrete random variable and basis correspondence

Random variable ζ	Polynomial type $\phi(\zeta)$	Support Γ
Poisson	Charlier	$\{0, 1, 2, \ldots\}$
binomial	Krawtchouk	$\{0, 1, 2, \ldots, N\}$
negative binomial	Meixner	$\{0, 1, 2, \ldots\}$
hypergeometric	Hahn	$\{0, 1, 2, \ldots, N\}$

$N \geq 0$ is a finite integer

Table 4: Hermite polynomials for the Gaussian random variable type

Chaos order i	Polynomial $\phi_i(\zeta)$	Norm squared $\langle \phi_i^2 \rangle = i\,!$
$i = 0$	$\phi_0 = 1$	$\langle \phi_0^2 \rangle = 1$
$i = 1$	$\phi_1 = \zeta$	$\langle \phi_1^2 \rangle = 1$
$i = 2$	$\phi_2 = \zeta^2 - 1$	$\langle \phi_2^2 \rangle = 2$
$i = 3$	$\phi_3 = \zeta^3 - 3\,\zeta$	$\langle \phi_3^2 \rangle = 6$
$i = 4$	$\phi_4 = \zeta^4 - 6\,\zeta^2 + 3$	$\langle \phi_4^2 \rangle = 24$
$i = 5$	$\phi_5 = \zeta^5 - 10\,\zeta^3 + 15\,\zeta$	$\langle \phi_5^2 \rangle = 120$
$i = 6$	$\phi_6 = \zeta^6 - 15\,\zeta^4 + 45\,\zeta^2 - 15$	$\langle \phi_6^2 \rangle = 720$

3.5.1.3 *Multivariate PC basis*

In multi-dimensional stochastic spaces Γ, the multivariate orthogonal polynomial basis is defined by a space of d-variate orthonormal polynomial of total degree at most p. In order to accomplish this, a univariate polynomial chaos basis is introduced on each dimension, ζ_k, of the d-variate vector $\boldsymbol{\zeta} = (\zeta_1, \ldots, \zeta_d)$, according to the type of random variable in each dimension. A set of basis is defined as follow

$$\{\, \phi_i(\zeta_k) \,\}_{i=0}^{p}\,, \ k = 1, \ldots, d, \tag{39}$$

Table 5: Legendre polynomials for the uniform random variable type

Chaos order i	Polynomial $\phi_i(\zeta)$	Norm squared $\langle \phi_i^2 \rangle = \frac{1}{2i+1}$
$i = 0$	$\phi_0 = 1$	$\langle \phi_0^2 \rangle = 1$
$i = 1$	$\phi_1 = \zeta$	$\langle \phi_1^2 \rangle = 1/3$
$i = 2$	$\phi_2 = (3\,\zeta^2 - 1)/2$	$\langle \phi_2^2 \rangle = 1/5$
$i = 3$	$\phi_3 = (5\,\zeta^3 - 3\,\zeta)/2$	$\langle \phi_3^2 \rangle = 1/7$
$i = 4$	$\phi_4 = (35\,\zeta^4 - 30\,\zeta^2 + 3)/8$	$\langle \phi_4^2 \rangle = 1/9$
$i = 5$	$\phi_5 = (63\,\zeta^5 - 70\,\zeta^3 + 15\,\zeta)/8$	$\langle \phi_5^2 \rangle = 1/11$
$i = 6$	$\phi_6 = (231\,\zeta^6 - 315\,\zeta^4 + 105\,\zeta^2 - 5)/16$	$\langle \phi_6^2 \rangle = 1/13$

where d is the number of random dimensions. As before, these polynomials are uniquely defined by a given univariate probability density function $\rho_k(\zeta_k)$ at each dimension as shown by the orthogonality relation Eq. 38.

The corresponding $d-$variate orthogonal polynomial is constructed by tensor product of these univariate polynomials as follow

$$\Phi_i = \phi_{i_1} \otimes \ldots \otimes \phi_{i_d} = \prod_{j=1}^{d} \phi_{i_j}, \tag{40}$$

where the tensor product is taken over all combinations of the multi-index $i = (i_1, \ldots, i_d) \in \mathbb{N}_0^d$ satisfying

$$i_1 + \ldots + i_d \leq p. \tag{41}$$

The polynomial chaos expansion has, in general, infinite number of terms. In practice, however, the expansion must be truncated to a determined total number of terms $P + 1$. This number is a function of the chaos order $p \in \mathbb{N}_0$, and the number of random dimensions d ,

$$P + 1 = \binom{d + p}{d}.$$

3.5.2 PC coefficients

Unlike the stochastic Galerkin method, in the nonintrusive polynomial chaos the PC coefficients are obtained by projecting the solution u onto the multivariate PC basis. The first step in the calculation of the coefficients is to approximate the uncertain system output by a polynomial chaos expansion

$$u\left(\mathbf{x}, t, \boldsymbol{\xi}\right) \approx \sum_{i=0}^{P} \alpha_i \, \Phi_i(\boldsymbol{\zeta}).$$

Next, the uncertain output is projected onto the polynomial chaos basis

$$\left\langle u\left(\mathbf{x}, t, \boldsymbol{\xi}\right), \Phi_k(\boldsymbol{\zeta}) \right\rangle = \left\langle \sum_{i=0}^{P} \alpha_i \, \Phi_i(\boldsymbol{\zeta}), \Phi_k(\boldsymbol{\zeta}) \right\rangle.$$

By applying the polynomial chaos orthogonality property (eq.21) to the above expression, the right hand side is simplified to

$$\left\langle u\left(\mathbf{x}, t, \boldsymbol{\xi}\right), \Phi_k(\boldsymbol{\zeta}) \right\rangle = \sum_{i=0}^{P} \alpha_i \left\langle \Phi_i^2(\boldsymbol{\zeta}) \right\rangle \delta_{ik}.$$

Finally, the expansion coefficients are obtaining by using the Kronecker delta property

$$\alpha_k = \frac{\left\langle u\left(\mathbf{x}, t, \boldsymbol{\xi}\right), \Phi_k(\boldsymbol{\zeta}) \right\rangle}{\left\langle \Phi_k^2(\boldsymbol{\zeta}) \right\rangle}, \quad k = 0, \dots, P. \tag{42}$$

The calculation of every expansion coefficient involves two terms: in the numerator, the projection of the random quantity, u, onto every polynomial of the PC basis, Φ_k, and in the denominator, the norm squared of the multivariate orthogonal polynomial.

The calculation of the latter is quite simple. Once the types of random variable are defined, the univariate basis are defined according to table 7. Next, the multivariate basis are obtained the tensor product rule (Eq. 40). Then, the norm squared is obtained analytically by using the product of univariate norms squared

$$\left\langle \Phi_k^2(\boldsymbol{\zeta}) \right\rangle = \prod_{i=1}^{d} \left\langle \phi_{m_i^k}^2(\zeta_i) \right\rangle, \tag{43}$$

where the term ϕ expresses the univariate polynomial and depends on the type of random variable.

The calculation of the former term, however, is the most computationally extensive involving calculation of multidimensional integrals.

$$\langle u\left(\mathbf{x}, t, \boldsymbol{\xi}\right), \Phi_k(\boldsymbol{\zeta})\rangle = \int_{\Gamma} u(\mathbf{x}, t, \boldsymbol{\xi}) \, \Phi_k(\boldsymbol{\zeta}) \, \rho(\boldsymbol{\zeta}) \, d\boldsymbol{\zeta}, \quad k = 0, \ldots, P. \tag{44}$$

Therefore, the primary computationally effort resides in evaluating the term in the numerator. Any standard method for multivariate integrals can be applied for this term. Some of the most common strategies are sampling methods such as Monte Carlo, and tensor product of univariate quadratures.

A different type of methods that do not rely on the solution of multivariate integrals uses linear equation system, or regression to evaluate the expansion coefficients. The main idea is to obtain at least $P + 1$ deterministic solutions based on select set of points. Then, the expansion coefficients are determined by either solving a linear system, or by regression with the deterministic solutions, and every polynomial basis evaluated at every point of the selected set. Hosder [54] uses this approach to study the effect of geometrical variability in supersonic flows over wedges. More recently, Alekseev *et al.* [3] uses a similar method along with adjoint approaches to quantify functional uncertainty in one-dimensional thermal conduction models. Even though these methods are simple and ensures an accurate representation at the set of selected points, it lacks explicit control on the error elsewhere [79], and thus this stands as the main drawback of these methods. Integration methods, on the other hand, allow control of the mean-square error. For this reason, integration methods is adopted in this research.

Integration methods, however, either require a large size sample as in the case of Monte Carlo methods or suffer from the curse of dimensionality as in tensor products of univariate quadratures. This is a strong limitation for traditional integration

methods and thus it may render these methods unusable for practical problems. In this work, this problem is addressed by adopting sparse grids methods. This type of methods is discussed in detail in the next chapter.

3.5.3 PC approximation

Given a chaos order p, the $p^{th}-$order and d uncertain parameters, the PC approximation of the random response u is obtained by projecting u onto the multivariate PC basis.

$$u\left(\mathbf{x}, t, \boldsymbol{\xi}\right) \approx \sum_{i=0}^{P} \alpha_i, \Phi_i(\boldsymbol{\zeta}),$$

where

$$P = \frac{(d+p)!}{d!\, p!} - 1.$$

In the previous equations, α_i and Φ_i are defined according to equations 40 and 60, respectively. In order to illustrate how the multivariate basis is constructed for higher stochastic dimensions, table 6 shows the terms of gPC expansion for a three-dimensional $(d = 3)$ stochastic space, and a chaos order up to $p = 3$. Note the multi-index i of the polynomials Φ_i obeys the relationship defined in eq. 41 according to the chaos order p. The univariate polynomial basis ϕ are defined according to each stochastic variable type as shown in table 1

3.5.4 Statistical moments

Given a sufficiently accurate gPC approximation, an analytical representation for the random quantity is available. Therefore, the PC method can be used to obtain probability density functions by sampling the PC expansion. Statistical moment of interest such as mean and variance can also be obtained by taking expectation to the PC expansion, and are defined as

$$\mu = \alpha_0 \tag{45}$$

$$\sigma^2 = \sum_{i=1}^{P} \alpha_i^2 \left\langle \Phi_i^2 \right\rangle \tag{46}$$

Table 6: Expansion terms for three random variables

Expansion term i	Chaos order p	Polynomial Φ_i
0	$p = 0$	$\phi_0(\zeta_1)\,\phi_0(\zeta_2)\,\phi_0(\zeta_3)$
1	$p = 1$	$\phi_1(\zeta_1)\,\phi_0(\zeta_2)\,\phi_0(\zeta_3)$
2		$\phi_0(\zeta_1)\,\phi_1(\zeta_2)\,\phi_0(\zeta_3)$
3		$\phi_0(\xi_1)\,\phi_0(\zeta_2)\,\phi_1(\zeta_3)$
4	$p = 2$	$\phi_2(\zeta_1)\,\phi_0(\zeta_2)\,\phi_0(\zeta_3)$
5		$\phi_1(\zeta_1)\,\phi_0(\zeta_2)\,\phi_1(\zeta_3)$
6		$\phi_1(\zeta_1)\,\phi_1(\zeta_2)\,\phi_0(\zeta_3)$
7		$\phi_0(\zeta_1)\,\phi_0(\zeta_2)\,\phi_2(\zeta_3)$
8		$\phi_0(\zeta_1)\,\phi_1(\zeta_2)\,\phi_1(\zeta_3)$
9		$\phi_0(\zeta_1)\,\phi_2(\zeta_2)\,\phi_0(\zeta_3)$
10	$p = 3$	$\phi_3(\zeta_1)\,\phi_0(\zeta_2)\,\phi_0(\zeta_3)$
11		$\phi_2(\zeta_1)\,\phi_0(\zeta_2)\,\phi_1(\zeta_3)$
12		$\phi_2(\zeta_1)\,\phi_1(\zeta_2)\,\phi_0(\zeta_3)$
13		$\phi_1(\zeta_1)\,\phi_0(\zeta_2)\,\phi_2(\zeta_3)$
14		$\phi_1(\zeta_1)\,\phi_1(\zeta_2)\,\phi_1(\zeta_3)$
15		$\phi_1(\zeta_1)\,\phi_2(\zeta_2)\,\phi_0(\zeta_3)$
16		$\phi_0(\zeta_1)\,\phi_0(\zeta_2)\,\phi_3(\zeta_3)$
17		$\phi_0(\zeta_1)\,\phi_1(\zeta_2)\,\phi_2(\zeta_3)$
18		$\phi_0(\zeta_1)\,\phi_2(\zeta_2)\,\phi_1(\zeta_3)$
19		$\phi_0(\zeta_1)\,\phi_3(\zeta_2)\,\phi_0(\zeta_3)$

CHAPTER IV

STATISTICAL MOMENTS BASED ON SPARSE GRIDS

It was seen in the previous chapter that most of the computational effort in propagating uncertainties with the non-intrusive polynomial chaos resides on the calculation of the expansion coefficients. This usually involves calculation of multivariate integrals. Conventional class of methods for integration include Monte Carlo and those based on tensor product of univariate quadratures. The former class require large sample size. The latter suffers from the exponential growth with dimensionality, the so-called "*curse of dimensionality.*" This is a serious limitation in the applicability of the non-intrusive polynomial chaos to practical problems such as those involving medium or large number of uncertain parameters.

The main purpose of this chapter is to describe a strategy for reducing the computational cost of calculating the coefficients of the polynomial chaos expansion. In order to achieve this, sparse grids techniques are employed. Sparse grids are efficient methods for representing multivariate functions. This technique prevents the exponential growth with number of uncertainty parameters and thus is able to alleviate the "curse of dimensionality."

In this chapter, the background of sparse grids is presented first. The emphasis here is the main aspects of its theory and implementation. Next, a strategy named gPC-SG is developed and presented. This is based on sparse grid techniques for calculating the expansion coefficients of the non-intrusive polynomial chaos. Finally, results for this strategy are shown.

4.1 Background

Conventional algorithms for numerical calculation of multivariate integrals are often limited by the so-called *curse of dimension* [10, 11], which means that the computational cost of representing an approximation for a determined accuracy ϵ increases exponentially with the number of dimensions of the considered integrand. For instance, the accuracy of classical numerical quadrature methods based on product of tensor rules scales as $\epsilon(N) = \mathcal{O}(N^{-r/d})$ [89], for functions with dimensionality d and bounded derivatives up to order r. Therefore, even for moderate number of dimensions the convergence is slow and this situation is exacerbated as the dimensionality grows.

Other methods such as Monte Carlo methods are independent of the dimensionality; however, its convergence rate is extremely slow due to the fact that its accuracy scale as $\epsilon(N) = \mathcal{O}(N^{-1/2})$. Therefore, these methods require large number of samples for acceptable degrees of accuracy. Quasi-Monte Carlo methods have accuracies that scale as $\epsilon(N) = \mathcal{O}(N^{-1}(logN)^d)$. Although this is almost half order better rate than the cost of crude Monte Carlo methods, the dimensionality causes convergence problems for high dimensions [40].

The cost dependency on the dimensionality, however, can be circumvented to some extent by restricting the class of functions under consideration. For functions having bounded mixed derivatives, sparse grid techniques can overcome this curse of dimension to a certain extent. In this technique, multivariate quadrature formulas are constructed by combining tensor products of univariate formulas. Among the possible tensor product combinations, high level tensor products in several dimensions are avoided simultaneously. As a result, the method accuracy scales as $\epsilon(N) = \mathcal{O}(N^{-r}(logN)^{(r+1)(d+1)})$. Under the considered mathematical assumptions, this technique offers better convergence than those of Monte Carlo, Quasi-Monte Carlo, and conventional methods based on full tensor products of quadratures

[40, 51, 65]

A brief explanation of the sparse grid technique is presented below. The focus here is in the main aspects of the theory and its implementation. For more detailed description, the reader is recommended to review other sources such as [14] which provides a deep review of these methods. Because sparse grids are built by using tensor product of one-dimensional interpolating formulas, the tensor product rule for multivariate function representation is also reviewed. Next, formulas for statistical moments are developed for the non-intrusive polynomial chaos, and finally results for statistical moment calculations are shown.

4.2 The tensor product rule

The tensor product rule can be considered a technique to extend to multiple dimension univariate interpolating formulas or univariate integration quadrature rules to multiple dimensions. In the case of interpolation formulas, consider one-dimensional interpolation formulas for approximating a smooth univariate formulas $f : [0, 1] \to \mathbb{R}$

$$\mathcal{U}_i(f) = \sum_{j=1}^{m_i} f(x_i^j) \, a_i^j(x), \quad i \geq 1, \tag{47}$$

defined on a set of support nodes

$$\mathcal{X}_i = \{x_i^j \mid x_i^j \in [0, 1], \, j = 1, \, \ldots, m_i\}, \tag{48}$$

where the sub index $i \in \mathbb{N}$ denotes the interpolation level, m_i is the number of nodes for the interpolation level, and $a_i^j(x) \in C[0, 1]$ is the univariate basis function associated with the node j.

The tensor product over univariate interpolation formulas with different levels of accuracy in each dimension indicated by the multi-index $|\mathbf{i}| = (i_1, \ldots, i_d)$ is defined as

$$(\mathcal{U}_{i_1} \otimes \ldots \otimes \mathcal{U}_{i_d})(f) = \sum_{j_1=1}^{m_{i_1}} \ldots \sum_{j_d=1}^{m_{i_d}} f\left(x_{i_1}^{j_1}, \ldots, x_{i_d}^{j_d}\right) \left(a_{i_1}^{j_1} \otimes \ldots \otimes a_{i_d}^{j_d}\right), \tag{49}$$

where the tensor product of univariate basis function is defined as

$$a_{i_1}^{j_1} \otimes \ldots \otimes a_{i_d}^{j_d} = \prod_{k=1}^{d} a_{i_k}^{j_k}(x_k) \tag{50}$$

The product rule evaluates the multivariate function f at the full grid of points $\mathcal{X}_{i_1} \otimes \ldots \otimes \mathcal{X}_{i_d}$. In d dimensions, the product rule requires $m = \prod_{k=1}^{d} m_{i_k}$. This computational cost, in general, grows exponentially with the number of dimensions; for instance, consider the case in which the number of nodes are the same in all directions, the product rule therefore requires m_i^d evaluations of the multivariate function f. This exponential growth of the computational cost with the number of dimensions is known as "curse of dimensionality" of multivariate function representation. In order to illustrate the construction of full grid of points $\mathcal{X}_1 \otimes \ldots \otimes \mathcal{X}_d$, two-dimensional product rules of univariate nodal set are shown in figure 4.
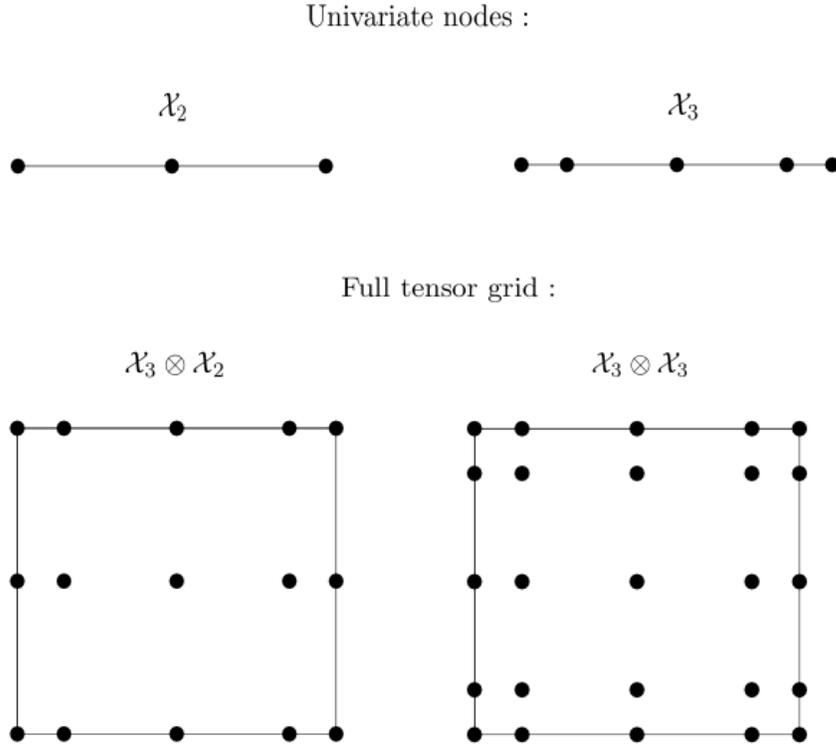

Figure 4: Full tensor grids: $\mathcal{X}_3 \otimes \mathcal{X}_2$, and $\mathcal{X}_3 \otimes \mathcal{X}_3$

4.3 Sparse Grids

Sparse grids are efficient methods to represent multivariate functions. This technique take advantage of the function smoothness and simultaneously prevents the exponential growth with dimensionality. Since its introduction by Smolyak [103], they have been subject of study for multivariate interpolation [81, 9], multivariate integration [39, 80], and discretization of partial differential equations (PDE's) [1, 16]. These methods are also known under various names, such as the Boolean method [26], and the discrete blending method [50]. These approaches can yield several order of magnitude reduction in the number of points required to achieve the same level of accuracy as the full tensor grid approach. This in turn can drastically alleviate the curse of dimensionality.

4.3.1 Smolyak's construction

The main idea of the Smolyak algorithm is to approximate a multivariate function by constructing a sparse interpolant that linearly combines tensor products of one-dimensional interpolating formulas while avoiding the use of high level interpolation formulas on several dimensions simultaneously.

The Smolyak tensorization algorithm builds on a sequences of one-dimensional interpolation formulas for approximating a smooth univariate function as defined by equations 47, and 48. The Smolyak algorithm approximates a multivariate function, $f(\mathbf{x}) : [0,1]^d \rightarrow \mathbb{R}$, by a sparse interpolant $A_{q,d}$ constructed by tensor products of univariate interpolating formulas, the Smolyak construction is then given by

$$A(q,d) = \sum_{q-d+1 \leq |\mathbf{i}| \leq q} (-1)^{q-|\mathbf{i}|} \binom{d-1}{q-|\mathbf{i}|} (\mathcal{U}_{i_1} \otimes \ldots \otimes \mathcal{U}_{i_d}), \qquad (51)$$

with $A(d-1,d) = 0$, and where d is the number of dimensions and $q \geq d$ is a parameter associated with sparse grid level $l = q - d$. The multi-index $\mathbf{i} = (i_1, \ldots, i_d) \in \mathbb{N}^d$

satisfies the following relationship

$$|\mathbf{i}| = \sum_{k=1}^{d} i_k, \tag{52}$$

here $i_k \in \mathbb{N}$ is the univariate interpolation level along the k direction. The tensor product of univariate interpolating functions is defined as

$$(\mathcal{U}_{i_1} \otimes \ldots \otimes \mathcal{U}_{i_d})(f) = \sum_{j_1=1}^{m_{i_1}} \ldots \sum_{j_d=1}^{m_{i_d}} f\left(x_{i_1}^{j_1}, \ldots, x_{i_d}^{j_d}\right) \left(a_{i_1}^{j_1} \otimes \ldots \otimes a_{i_d}^{j_d}\right). \tag{53}$$

The smolyak construction builds a sparse interpolant by adding combination of univariate interpolating formulas of level i_k subject to the constrain that the multi-index, i.e. the total sum of univariate interpolation levels across all dimensions $|\mathbf{i}| = i_1 + \ldots i_d$, has values between $q - d + 1$ and q.

This linear combination of tensor product of univariate formulas in the Smolyak construction leads to an efficient interpolation method that requires significantly fewer support nodes than conventional interpolation strategies on full tensor grids. The difference in the number of support nodes can be several orders of magnitude with increasing problem dimension. Furthermore, the asymptotic error decay of the full tensor grid interpolation with increasing grid resolution is preserved up to a logarithmic factor.

4.3.2 Univariate basis functions

The computation of the sparse interpolant involves tensor product operations of univariate basis functions of one-dimensional interpolation formulas. Several types of univariate basis function has been proposed. Some of them are based on piecewise functions, high-order basis function, other studied basis are interpolets and multiwavelets. The approximation properties of these basis function have been extensively studied, see for instance [14, 9]. In this work, the focus is on only few types of basis such as the Lagrangian characteristic polynomials and piecewise basis functions.

4.3.2.1 One-dimensional nodal sets

The univariate interpolation formulas (eq. 47) are defined over sets of specified nodes $\mathcal{X}_i = \{x_i^1, \ldots, x_i^{m_i}\} \subset [0, 1]$. Although several choices of nodal sets have been defined, nested nodal sets $\mathcal{X}_{i-1} \subset \mathcal{X}_i$ are more advantageous [39] because extending the interpolation level from $i - 1$ to i only requires function evaluations at the nodes that are unique to the level i. The node differential between levels is denoted by $\Delta\mathcal{X}_i$, and it is defined as $\Delta\mathcal{X}_i = \mathcal{X}_i \setminus \mathcal{X}_{i-1}$.

One of the choices of univariate nodal sets for high-order polynomials is the Chebyshev Gauss-Lobatto nodes. This is because, the non-equidistant nodes are required in order to avoid undesirable oscillations in high-order polynomials and also because of the necessity of nesting sets.

$$
m_i = \begin{cases} 1, & \text{if } i = 1 \\ 2^{i-1} + 1, & \text{if } i > 1 \end{cases}
$$

$$
x_i^j = \begin{cases} \frac{1}{2} & \text{for } j = 1, & \text{if } m_i = 1, \\ \frac{1}{2}\left[1 - \cos\left(\pi \frac{j-1}{m_i - 1}\right)\right] & \text{for } j = 1, \ldots, m_i, & \text{if } m_i > 1. \end{cases}
$$

Another choice for linear basis functions is the Clenshaw-Curtis nodes. This type of nodal set is defined in equidistant nodes and also complies the nesting property,

$$
m_i = \begin{cases} 1, & \text{if } i = 1 \\ 2^{i-1} + 1, & \text{if } i > 1 \end{cases}
$$

$$
x_i^j = \begin{cases} \frac{1}{2} & \text{for } j = 1, & \text{if } m_i = 1, \\ \frac{j-1}{m_i - 1} & \text{for } j = 1, \ldots, m_i, & \text{if } m_i > 1. \end{cases}
$$

Both type of nodal sets have shown the slowest increase with interpolation level compared to other nested rules [65], and thus they are adopted in this study.

4.3.2.2 Basis functions

Lagrange basis have been shown to be effective to represent functions that are sufficiently smooth. They provide high order interpolation with fast error decay with increasing number of nodes given the correct set of nodes. Specific type of nodal sets are required in order to avoid undesirable oscillations due to Runge's phenomenon such as the Chebyshev Gauss-Lobatto nodes. These polynomial basis are defined globally, meaning that the support range is $[0, 1]$ and that information of all the nodes are considered to construct every basis functions. These basis functions are shown in figure 5(a) for an interpolation level $i = 3$ with total number of nodes $m_i = 5$, observe that the value of the basis function is $a_i^j = 1$ at the respective node, and goes to zero at every node that is different from the node associated to the basis $a_i^k = 0$, for $k \neq j$, obeying the property $a^j(x_k) = \delta_{jk}$.

$$a_i^j(x) = \begin{cases} 1, & \text{if } i = 1 \\ \prod_{k=1,k\neq j}^{m_i}(x - x_i^k)(x_i^j - x_i^k), & \text{if } i > 1. \end{cases}$$

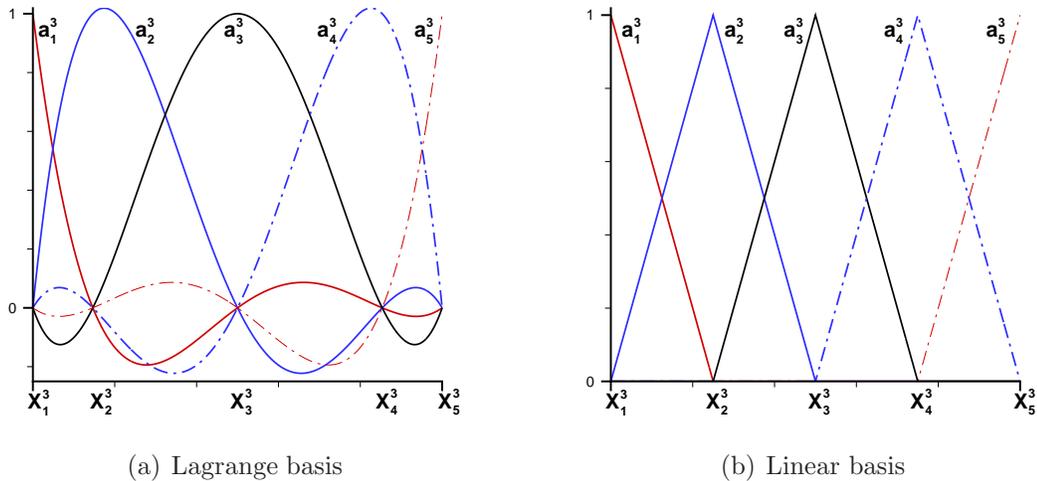(a) Lagrange basis   (b) Linear basis

Figure 5: Basis functions at Chebyshev-Gauss-Lobatto grid fig.(a) , and Cleshaw-Curtis grid fig.(b)

The idea behind piecewise basis functions is to give some capabilities to the basis functions of resolving local futures due to the locality of the support. A general approach for constructing high-order polynomial piecewise basis function was developed in [15, 17]. Among all the piecewise basis function, the linear is probably the simplest. Although it offers slower error decay as compared to other high order polynomial basis, these basis have shown to be capable of resolving local features such as discontinuities [74]. The linear basis is shown in figure 5(b) for a interpolation level $i = 3$ on equidistant Cleshaw-Curtis nodes, note that the local support of the basis which only involves the neighboring nodes.

$$a_i^j(x) = \quad 1, \quad \text{for } i = 1, \text{and}$$

$$a_i^j(x) = \begin{cases} 1 - (m_i - 1)|x - x_i^j|, & \text{if } |x - x_i^j| < \frac{1}{m_i - 1}, \\ 0, & \text{otherwise,} \end{cases} \quad \text{for } i > 1$$

4.3.3 Multivariate basis functions

Multivariate basis functions are achieved by using tensor products of univariate basis functions as given by

$$a_{i_1}^{j_1} \otimes \ldots \otimes a_{i_d}^{j_d} = \prod_{k=1}^{d} a_{i_k}^{j_k}(x_k),$$

where a_i^j is the basis function of the one-dimensional interpolation formula. The type of multivariate basis function depends only on the type of univariate basis as defined previously.

4.3.3.1 Multi-dimensional nodal sets

The sparse interpolant needs to be computed over a set of sparse nodes. Consider $\mathcal{X}_i$, the univariate set of points used to interpolate the one-dimensional interpolating formula $\mathcal{U}_i$. The function that defines the multivariate set of sparse nodes is then

defined by

$$\mathcal{H}(q,d) = \bigcup_{q-d+1 \leq |\mathbf{i}| \leq q} (\,\mathcal{X}_{i_1} \otimes \ldots \otimes \mathcal{X}_{i_d}\,). \tag{54}$$

One of the most of important feature of sparse grids that allow efficient representation of multivariate functions is the nested nature of the univariate set of nodes defined in the construction of the sparse interpolant. The appropriate selection of the univariate set of points can ensure that the set of points are nested $\mathcal{X}_{i-1} \subset \mathcal{X}_i$. This nested property of some univariate set of nodes has similar effect in multi-dimensions. Thus, increase of the sparse set of nodes from q to $q-1$, the number of nodes are increased only by the differential nodes given by

$$\Delta\mathcal{H}(q,d) = \bigcup_{|\mathbf{i}|=q} (\,\Delta\mathcal{X}_{i_1} \otimes \ldots \otimes \Delta\mathcal{X}_{i_d}\,). \tag{55}$$

As a result, the sparse of nodes can be written only by adding the differential nodes from level to level.

$$\mathcal{H}(q,d) = \bigcup_{|\mathbf{i}| \leq q} (\,\Delta\mathcal{X}_{i_1} \otimes \ldots \otimes \Delta\mathcal{X}_{i_d}\,). \tag{56}$$

Some of the nested univariate of nodes include the Clenshaw-Curtis nodes and the Gauss-Lobatto nodes. However, it has been shown in [65] that is the Clenshaw-Curtis nodes that increases the least with the number of dimension and thus it is adopted in this work.

The construction of the sparse multi-dimensional nodal set in two dimensions $(d = 2)$ is illustrated in figure 6. An sparse interpolation level $l = 2$ $(q = 4)$ is considered. The nodes for the sequence of univariate interpolation formulas $\mathcal{X}_1, \mathcal{X}_2$, and $\mathcal{X}_3$ are shown in top of the figure 6. The sparse grid combine tensor products of lower degree $\mathcal{X}_{i_1} \otimes \mathcal{X}_{i_2}$ such that the multi-index $|\mathbf{i}| = i_1 + i_2$ has values between $q - d + 1$ and q, i.e. $3 \leq i_1 + i_2 \leq 4$, as shown by equation 51. The nodes of these tensor products as well as the resulting sparse grid are shown in the lower part of the figure
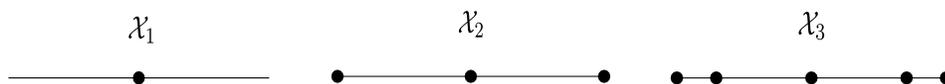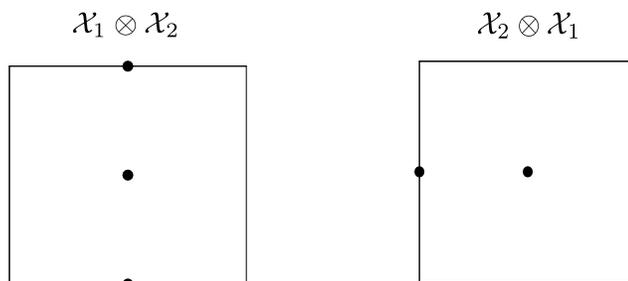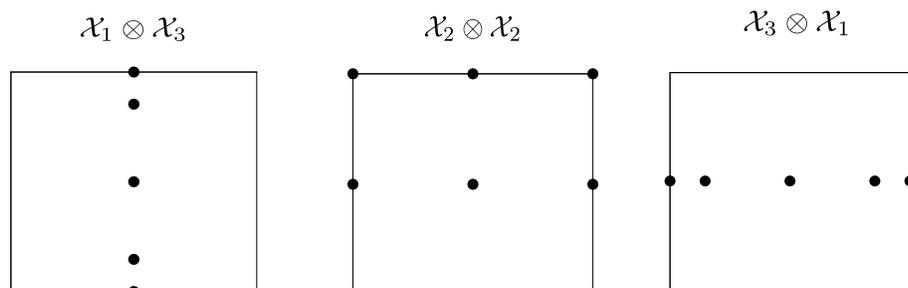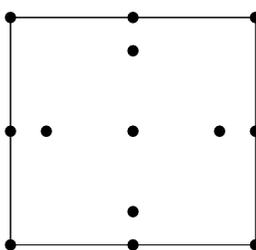
Figure 6: Construction of a sparse grid in two dimension, $q = 4$, and $d = 2$

4.3.4 Accuracy of the sparse grid approximation

Consider multivariate functions f, $f(\mathbf{x}) \in \mathbb{R}$, with $\mathbf{x} = (x_1, \ldots, x_d)$ defined in the d-dimensional unit interval $\Omega = [0, 1]^d$; and function mixed derivatives

$$D^\alpha f = \frac{\partial^{|\boldsymbol{\alpha}|}}{\partial x_1^{\alpha_1} \ldots \partial x_1^{\alpha_d}}, \tag{57}$$

where $\alpha \in \mathbb{N}_0^d$ denotes a d-dimensional multi-index with norm $|\boldsymbol{\alpha}| = \sum_{i=1}^{d} \alpha_i$.

4.3.4.1 Polynomial sparse grid approximation

High order basis function are usually obtained by employing Lagrange characteristic polynomials. For this type of basis, if the function mixed derivatives are continuous, i.e. $\alpha_i \le r \; \forall i$, the approximation error is derived in [81], and is given by

$$||f - A(q,d)||_\infty = \mathcal{O}\left(N^{-r}|\log N|^{(r+2)(d-1)+1}\right), \tag{58}$$

where $N = N(q,d)$ is the number of nodes required by the sparse representation $A(q,d)$.

4.3.4.2 Piecewise multilinear sparse grid approximation

For the multivariate basis function based on linear functions, if the function mixed derivatives are at most twice continuous respect to any variable, i.e. $\alpha_i \le 2 \; \forall i$ the error approximation error [81] is given by

$$||f - A(q,d)||_\infty = \mathcal{O}\left(N^{-2}|\log_2 N|^{3(d-1)}\right) \tag{59}$$

where N is defined as above.

4.4 The gPC-SG strategy

The gPC-SG is introduced here as a mean to alleviate the curse of dimensionality of traditional integration methods. The main idea behind this strategy is to represent the gPC coefficients:

$$\alpha_k = \frac{\langle u(\mathbf{x},t,\boldsymbol{\xi}), \Phi_k(\boldsymbol{\zeta})\rangle}{\langle \Phi_k^2(\boldsymbol{\zeta})\rangle} = \frac{1}{\langle \Phi_k^2(\boldsymbol{\zeta})\rangle} \int_\Gamma u(\mathbf{x},t,\boldsymbol{\xi}) \, \Phi_k(\boldsymbol{\zeta}) \, \rho(\boldsymbol{\zeta}) \, d\boldsymbol{\zeta}, \quad k = 0, \dots, P,$$

as a sparse representation. As a consequence the number of function (u) evaluations in the coefficient integrand, shown in the above equation, is reduced. Once the coefficients are obtained, the polynomial chaos expansion can be used to obtain statistics of interest. For instance, independent samples can be drawn to obtain probability

density functions (pdf) of the stochastic response u. Moreover, statistical moments such as mean and variance can also be obtained. These quantities are a central aspect of design under uncertainty.

There are two main aspects that allow the development of the gPC-SG strategy. The first one is the mutual independence among random variables. Consider d independent random variables $\{\xi_k\}_{k=1}^{d}$ with individual probability density function $\rho(\xi_k)$, and defined in the random space $\Gamma_k \in \mathbb{R}$, then the joint probability density function of $\boldsymbol{\xi} = (\xi_1, \ldots, \xi_d)^{\intercal}$ is defined as

$$\rho = \prod_{k=1}^{d} \rho(\xi_k) \tag{60}$$

with support $\Gamma = \Gamma_1 \times \ldots \times \Gamma_d \in \mathbb{R}^d$.

The second aspect is the product tensorization structure of the generalized polynomial chaos and sparse grids. The multivariate basis of both methods are extension of univariate basis function to multivariate cases. It will be shown that both the mutual independence of the random variables and the product tensorization structure of the multivariate basis functions facilitate sparse representation of the generalized polynomial chaos coefficients.

4.4.1 gPC-SG coefficients

In the polynomial chaos, the multivariate basis Φ is a product tensorization of the univariate gPC basis functions ϕ. This in turn allows simplifications on the calculation of the coefficients of the gPC expansion if the stochastic response is expressed by a sparse interpolant, i.e. $f(\boldsymbol{\xi}) \approx A(q,d)$. Then, the polynomial chaos expansion coefficients (Eq. 60) can be expressed as follow

$$\alpha_l = \frac{1}{\langle \Phi_l^2(\boldsymbol{\zeta}) \rangle} \int_{\Gamma} A(q,d)\, \Phi_l(\boldsymbol{\zeta})\, \rho(\boldsymbol{\xi})\, d\boldsymbol{\xi}, \tag{61}$$

where Φ is the gPC multivariate basis and $\rho(\boldsymbol{\xi})$ is the joint probability density function. Note that the argument of gPC basis and the random variables are different;

this is because the gPC basis is defined over supports of standard random variables, whereas the actual random variable can be defined at any arbitrary support. The previous equation needs first to be transformed to space of the standard random variables ζ

$$\alpha_l = \frac{1}{\langle\, \Phi_l^2(\boldsymbol{\zeta})\,\rangle} \int_\Gamma A(q,d)\, \Phi_l(\boldsymbol{\zeta})\, \rho^*(\boldsymbol{\zeta})\, d\boldsymbol{\zeta}, \tag{62}$$

where $\rho^*(\boldsymbol{\zeta})$ expresses the joint probability function for the standard random variables. By substituting the expression for the sparse grid interpolant (Eq. 51), the gPC multivariate basis (Eq. 40) and the joint probability density function (Eq. 60), the expansion coefficient is expressed as follow:

$$
\begin{aligned}
\alpha_l \;=\; & \frac{1}{\langle\, \Phi_l^2(\boldsymbol{\zeta})\,\rangle} \int_\Gamma \sum_{q-d+1\leq|\mathbf{i}|\leq q} (-1)^{q-|\mathbf{i}|} \binom{d-1}{q-|\mathbf{i}|} \sum_{j_1=1}^{m_{i_1}} \cdots \sum_{j_d=1}^{m_{i_d}} f(\boldsymbol{\xi}_{\mathbf{j}}^{\mathbf{i}}) \times \\
& \prod_{k=1}^{d} a_{i_k}^{j_k}(\eta) \prod_{k=1}^{d} \phi_{l_k}(\zeta) \prod_{k=1}^{d} \rho_k^*(\zeta)\, d\boldsymbol{\zeta}.
\end{aligned} \tag{63}
$$

Note that the last three terms are products of the sparse grid univariate basis, the univariate gPC basis, and the individual probability density function of the standard random variable; therefore, these terms can be expressed as only one product of univariate integrals comprised by the sparse grid univariate basis, the gPC basis, and the individual probability density function. This results in

$$\alpha_l = \frac{1}{\langle\, \Phi_l^2(\boldsymbol{\xi})\,\rangle} \sum_{q-d+1\leq|\mathbf{i}|\leq q} (-1)^{q-|\mathbf{i}|} \binom{d-1}{q-|\mathbf{i}|} \sum_{j_1=1}^{m_{i_1}} \cdots \sum_{j_d=1}^{m_{i_d}} f(\boldsymbol{\xi}_{\mathbf{j}}^{\mathbf{i}}) \prod_{k=1}^{d} \mathcal{I}_{i_k}^{j_k}, \tag{64}$$

where

$$\mathcal{I}_{i_k}^{j_k} = \int_{\Gamma_k^*} a_{i_k}^{j_k}(\eta)\, \phi_{l_k}(\zeta)\, \rho_k^*(\zeta)\, d\zeta \tag{65}$$

is a one-dimensional integral of the univariate sparse grid basis, the gPC basis and the individual probability density function. Because the sparse grid univariate basis in $a \in [0,1]$, the argument η needs to be mapped the support of the standard random

variable of the gPC expansion, Γ_i^*. This can be simply accomplished by a linear mapping. Moreover, the collocation points ξ_j^i at which the function is evaluated need to be transformed to be in agreement with the standard random variables. For instance, the following transformation

$$\xi = \mu_\xi + \sigma_\xi \zeta \tag{66}$$

$$\xi = a + (\zeta + 1)\frac{(b-a)}{2} \tag{67}$$

is needed for a normal random variable $\mathcal{N}(\mu, \sigma)$, and for a uniform variable $U(a, b)$, respectively.

The formula developed in equations 64 and 65 for the calculation of the gPC coefficients are very convenient since they allow fast calculation of polynomial chaos expansion. The individual one-dimensional integral (Eq.65) can be calculated accurately given the individual probability density functions. Moreover, these calculations can be done off-line since given the distribution of the random variable, the univariate gPC basis is known. Moreover, for every sparse grid level, the univariate basis is also known.

Once the polynomial chaos expansion is obtained, uncertainty can be propagated by either obtaining probability density functions or statistical moments of any other from the expansion. For instance, for the first two statistical moments are obtained by taking expectations of the expansion which leads the following relationships:

$$\mu = \alpha_0 \tag{68}$$

$$\sigma^2 = \sum_{i=1}^{P} \alpha_i^2 \langle \Phi_i^2 \rangle. \tag{69}$$

4.5   gPC-SG statistical moments comparison

In order to show the effectiveness of the polynomial chaos expansion - sparse grid based method (gPC-SG), a comparison between this method and other uncertainty propagation methods is presented in this section. The other methods considered are

the Monte-Carlo method (MC), the local expansion method (LE), and the univariate reduction method (UDR).

The moments are calculated for certain analytical functions chosen from the Genz test package [38]. This set of functions was developed for evaluating the performance of multidimensional integration [39, 80], and multi-dimensional interpolation [81, 9] schemes. It is composed of six families of functions defined on the hypercube $[0, 1]^d$. The parameter $\mathbf{c} = (c_1, \ldots, c_d)$ increases monotonically the difficulty of the function, whereas $\mathbf{w} = (w_1, \ldots, w_d)$ acts a shift parameter. The parameters $\mathbf{w}$ are randomly chosen from $[0, 1]$. The parameters $\mathbf{c}$ are chosen randomly from $[0, 1]$ as well, but are normalized such that $\sum_{i=1}^{d} c_i = b$, where b depends on the function as shown in table 7. A tenth-dimensional ($d = 10$) example is considered. The tenth random variables x_i are considered to be independent and identically distributed according to a uniform distribution $U(0, 1)$.

The uncertainty propagation approaches are set up as follows. The coefficients of the polynomial chaos expansion are determined by a chaos order of $p = 6$ and the multivariate integrals involved in their calculation are carried out by sparse grid techniques with levels up to 4. For the local expansion method, the derivatives involved in the variance calculation are performed by one sided (forward) finite difference. The univariate reduction method are calculated by according to a three point Gauss-Legendre quadrature for the unidimensional integration.

The relative error of the calculation of the first two statical moments for the product peak and Gaussian test functions as a function of the number of evaluations are shown in figures 7 and 8. For all the examined test functions, the faster decrease of the relative error of the gPC-SG method compared to the Monte Carlo method is evident. Indeed, this approach leads to order of magnitude reduction in the number of evaluations compared to sampling based methods. The higher values of relative error of the Monte Carlo method is strongly dependent on its convergence rate which

Table 7: Genz test functions

Name	Function	b
Oscillatory	$f(\mathbf{x}) = \cos\left(2\pi w_1 + \sum_{i=1}^{d} c_i x_i\right)$	9.00
Product peak	$f(\mathbf{x}) = \prod_{i=1}^{d} \left[c_i^{-2} + (x_i - w_i)^2\right]^{-1}$	7.25
Corner peak	$f(\mathbf{x}) = \left(1 + \sum_{i=1}^{d} c_i x_i\right)^{-(d+1)}$	1.85
Gaussian	$f(\mathbf{x}) = \exp\left[-\sum_{i=1}^{d} c_i^2 (x_i - w_i)^2\right]$	7.03
Continuous	$f(\mathbf{x}) = \exp\left(-\sum_{i=1}^{d} c_i |x_i - w_i|\right)$	20.04
Discontinuous	$f(\mathbf{x}) = \begin{cases} 0 & \text{if } x_1 > w_1 \text{ or } x_2 > w_2, \\ \exp\left(\sum_{i=1}^{d} c_i x_i\right), & \text{otherwise.} \end{cases}$	4.30

always scale as $\mathcal{O}(N^{-1/2})$.

It can also be noticed that low computational cost approaches such as the UDR and LE lead the highest relative error among all approaches. The local expansion method although is the cheapest computationally requiring only $d+1$ function evaluations (as defined by the one-sided finite difference) is the most inaccurate. The reason for this is that the local validity of these method prevent them of giving more accurate results for complicated functions and larger degrees of uncertainty. Although it has been suggested that for more complicated responses the accuracy of the method can be improved by considering higher order derivatives, these higher order derivatives
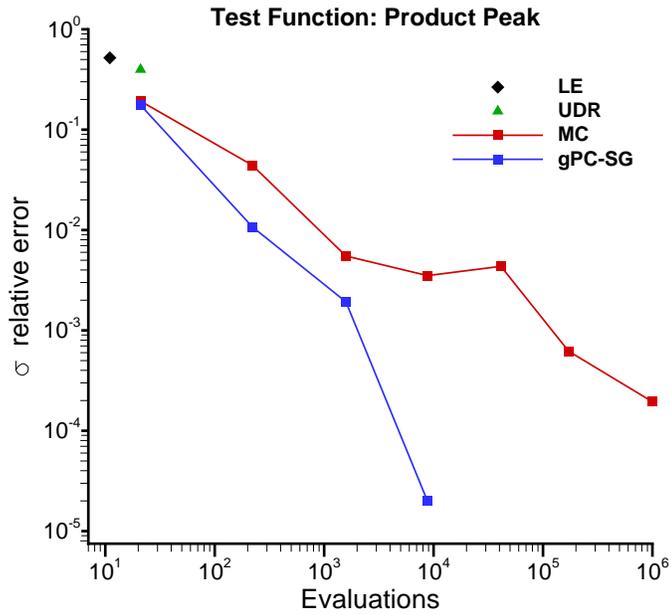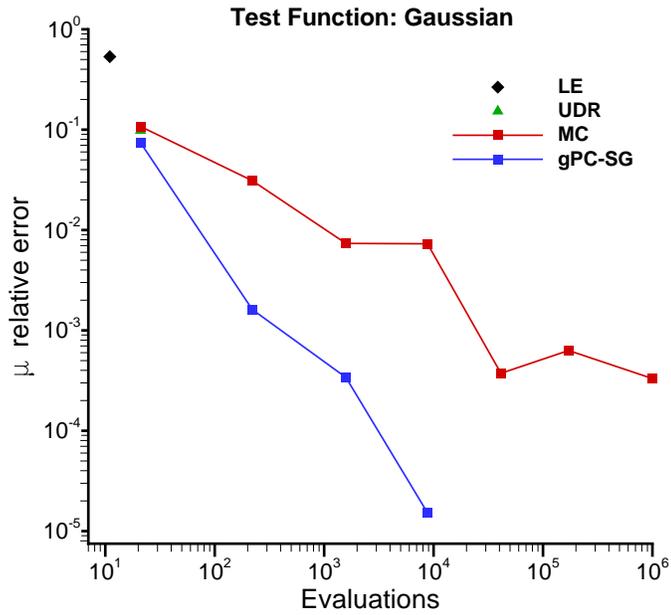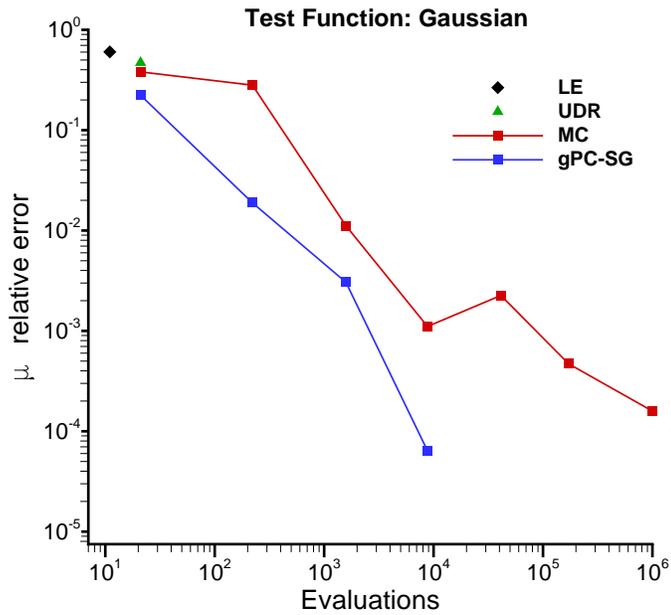
(a) Mean
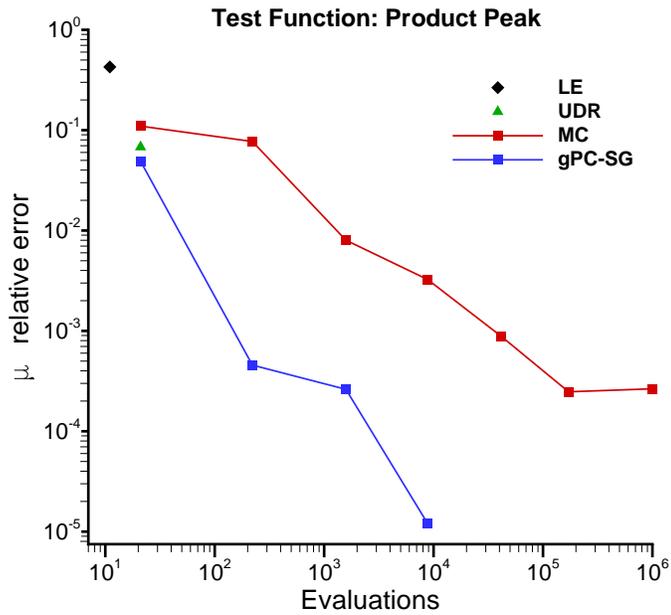
(b) Standard deviation

Figure 7: Statistical moment comparison: Product peak function figs. (a) & (b)

do not ensure improvement of the variance due to the local assumption [43]. In the

univariate decomposition reduction method, the three point quadrature considering

(a) Mean

(b) Standard deviation

Figure 8: Statistical moment comparison: Gaussian functions figs. (a) & (a)

leads to a computational cost of $2d + 1$. This expense is the same as the first sparse

grid level considered for the gPC-SG method. In spite of having the same cost, the

gPC-SG has a lower relative error. An explanation for this lies in the fact that even though the UDR moments take into consideration the individual density function by assuming, in this case, Gauss-Legendre quadrature for the uniform random variables, the method still relies on simple quadrature calculations. The gPC-SG formulation explicitly considers the individual density functions, in this case by the Legendre chaos basis, and approximate the moments through efficient multidimensional integration of the expansion coefficients. The accuracy on the UDR method can be improved by considering more points in the one-dimensional quadratures; however, since the method is based on one-dimensional representation of multi-variate functions, it can not deal with more complicated functions, and thus is restricted to lower dimensionality functions, i.e. functions whose simplicity is such that allows them to be represented by a linear combinations of one-dimensional functions only.

CHAPTER V

STOCHASTIC EXPANSION-BASED ROBUST OPTIMIZATION

In the previous chapter, an uncertainty propagation strategy based on stochastic expansions called gPC-SG was presented. In this chapter, this UP is used with an adaptive sampling formulation for multi-objective problems in order to develop two strategies for robust design: 1) a single level robust optimization strategy and 2) a bi-level robust optimization strategy.

The first strategy uses the gPC-SG approach with an adaptive sampling formulation for multi-objective problems. Adaptive sampling is a technique to sequentially select each sample point based on information from previously sampled data. This approach is especially efficient when dealing with expensive simulations. This efficiency makes adaptive sampling a promising method to be incorporated into design under uncertainty.

The second strategy is similar, but uses two levels of fidelity of the uncertainty propagation method. The use the above strategy is promising since it combines an efficient UP method for the uncertain parameters and an efficient method for sampling the design space, high computational expenses of propagating uncertainties for highly non-linear cost functions and large degrees of uncertainty is unavoidable. In order to mitigate this possible scenario, a bi-level gPC-SG based robust optimization strategy is developed. The main idea behind this strategy is that the optimization objectives are obtained by propagating uncertainties with two different levels of accuracy (fidelity). Such a bi-level accuracy strategy is then included within a robust design formulation.

In general, uncertainties can be propagated by using different methods featuring different degrees of accuracy (fidelity) and computational cost. A low-fidelity method is cheaper to evaluate, but less accurate. Conversely, a high-fidelity method is computationally intensive, but accurate. By using a bi-level strategy in a robust design formulation, more can be learned about the statistics of interest by additionally calculating them with a less accurate uncertainty propagation method. This in turn may reduce the use of the high fidelity uncertainty propagation method and hence can decrease the overall computational cost.

The process of representing an output model by using lower-fidelity information is usually called a multi-fidelity or variable-fidelity method. This approach has been mostly applied to deterministic optimization with expensive analysis and, to lesser extent, to surrogate modeling of computational and experimental data. In this thesis, the multi-fidelity idea is applied to a different problem: design under uncertainty.

It is emphasized that multi-fidelity modeling is applied to the propagation method in robust design rather than the fidelity of physics modeling. Unlike deterministic optimization which only requires one evaluation of the cost function per design, robust design optimization may require moderate or high number of samples of the cost functions at every design point. This is because the optimization objectives usually involves the first two statistical moments which are an outcome of propagating uncertainties through the cost function. The computational cost can even be higher if the degrees of uncertainty are large, the cost function is highly non-linear, or the cost function is evaluated by expensive analysis codes. Therefore, managing two different levels of accuracy of the uncertainty propagation method can be useful for reducing the overall number of calls of the involved cost function.

The main idea of multi-fidelity approaches is to correct the low fidelity data with as little high fidelity data as possible. In deterministic design optimization, several methods have been proposed for multi-fidelity modeling. Some methods are based

on local approximations and others on global modeling [63]. Local approximation-based methods correct the low fidelity model so agreement is achieved with the high fidelity model in the vicinity of a single design point. Conversely, global methods seek to provide a global representation of the system model by constructing global calibration models. Some of these approaches include sequential kriging [55] and co-kriging [36], both of which were derived from the autoregressive method [64]. A third class includes methods based on space mapping [12]. These methods are better suited for problems in which the different fidelity models are defined in different input spaces [100].

In this chapter, the background of adaptive sampling is presented first. In the first section, the necessary elements such as Gaussian process (GP) modeling, and sampling criteria such as expected improvement are reviewed. In addition, dependent or correlated Gaussian process are reviewed and discussed as a mean for multi-fidelity modeling. Then, robust design strategies are developed and presented. Finally, the usefulness of these strategies are tested in canonical problems.

5.1 Adaptive sampling

In a typical design problem decisions such as how and where to sample are made and fixed in advance. Such a criteria may require dense sample of points over the entire design space for acceptable quality of surrogate models. This, however, can be wasteful if the objectives of the design problem are expensive. Moreover, the surrogate models can be either unnecessarily accurate in unpromising regions of the design space, or inaccurate in promising regions. In contrast, adaptive sampling is a sample technique that uses the acquired data (observations) in order to adjust or infer the next sample points as the design problem is being run. As a result, this technique is able to concentrate points in regions of interest.

In design, there are two main components in adaptive sampling. The first is the

71

representation (surrogate) of the output model as a predictive distribution. The use of predictive distribution in turn allows the development of criteria for sampling which is the second component.

A brief explanation of the necessary methods for adaptive technique is presented next. Gaussian processes are defined first as a mean to model outputs as predictive distributions. Expected improvement is then next reviewed as a criteria for placing sample adaptively. These two concepts are the main constituents of the multi-objective optimization part of the single level gPC-SG based robust optimization strategy. Dependent Gaussian processes are also reviewed as mean to combine output models of different fidelity. This is technique is used in the multi-objective optimization part of the bi-level gPC-SG based robust optimization strategy in which outputs of two different uncertainty propagation method are used.

5.1.1   Gaussian process modeling

Gaussian process (GP) modeling is a technique for inferring likely values of an output model f for a new input $\mathbf{x}^*$. Unlike surrogate models which predict a single value for the output model f, this technique represents the output model as a predictive distribution.

Consider training data $\mathcal{D}$ consisting of N input vectors paired with responses : $\{(\mathbf{x}_i, y_i), i = 1, \ldots, N\}$, a Gaussian process expresses uncertainty over the value of the response variable by using a normal distribution with mean, and variance equal to $\hat{f}(\mathbf{x})$, and $\hat{s}^2(\mathbf{x})$, respectively.

$$f(\mathbf{x}) \sim \mathcal{N}(\hat{f}(\mathbf{x}), \hat{s}^2(\mathbf{x})), \tag{70}$$

where f is GP model for the output. This type of modeling is illustrated in figure 9 for a one-dimensional training data set consisting of five points shown as red circles. At any arbitrary point x^*, the model is given by a predictive Gaussian distribution as

shown by the blue solid line. This predictive feature of GP model can also be visualized in the entire range of the independent variable by plotting the mean prediction and a confidence interval of 99.7%, $\hat{f} \pm 3\hat{s}(x)$; these are expressed by the solid and dashed lines, respectively. It must be noted that the variance of the model represents the uncertainty in the value of the model output based on the current data. Therefore, the variance value is zero at the training data points in the absence of noise in the training data responses.
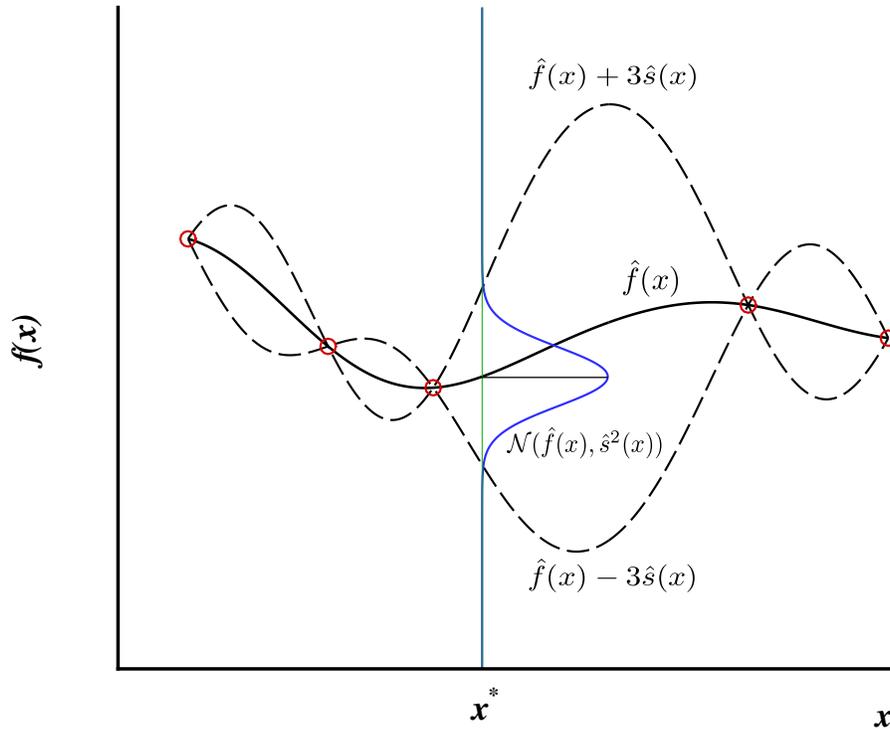

Figure 9: Gaussian process (GP)

Although the study of Gaussian processes may seem new due to its use in the machine learning community, its origin date backs to the 1940s with the works of Wiener-Kolmogorov in prediction theory and time series analysis [75, 97]. Later, approaches known as kriging [77] were developed in the geostatistics field for data interpolation [24]. Although kriging derivation and interpretation is somewhat different

to the methods considered by the machine learning community, kriging is identical to a Gaussian process regression. In the statistical community, the use of Gaussian processes to define prior distributions over functions dates back to 1978, when O'Hagan [84] applied the theory to one-dimensional curve fitting. More recently, in the machine learning field, Gaussian processes have been studied and developed for supervised learning [109].

Although several formulations for Gaussian process models exist, the GP process adopted in this study is kriging. This method has been scrutinized within the design optimization community and it is now a well established method for data regression and interpolation. In many works, kriging has been strictly applied as an interpolator; see for instance references [22, 21]. However, the main advantage of kriging and other Gaussian process models is their predictive capabilities [35] which allow adaptive sampling. It is precisely this capability of GP modeling that makes them an important element in this work. The kriging model is in explained in greater detail.

5.1.1.1 Kriging model

There are several types of kriging model, but this thesis will focus on a simple type used in engineering design literature. The kriging model can be expresses as follows

$$\hat{f}(\mathbf{x}) = \beta + z(\mathbf{x}), \tag{71}$$

where β is a constant and z is a stationary Gaussian random function. $z(\mathbf{x})$ gives a localized deviation from the global model and has zero mean and covariance

$$\text{Cov}\left[z(\mathbf{x}^i), z(\mathbf{x}^j)\right] = \sigma^2 R(\mathbf{x}^i, \mathbf{x}^j), \tag{72}$$

where

$$R(\mathbf{x}^i, \mathbf{x}^j) = \exp\left(-\sum_{m=1}^{d} \theta_m \,|\, \mathbf{x}_l^i - \mathbf{x}_l^j\,|^2\right). \tag{73}$$

In the above equation, R is the correlation function between two sampled data points. Then, the Gaussian process as shown in Eq. (70) is given as

$$\hat{f}(\mathbf{x}) = \hat{\beta} + \boldsymbol{r}^T \boldsymbol{R}^{-1} \left(\boldsymbol{Y} - \mathbf{1}\hat{\beta} \right) \tag{74}$$

$$\hat{s}(\mathbf{x}) = \left[1 - \boldsymbol{r}^T \boldsymbol{R}^{-1} \boldsymbol{r} + \left(1 - \mathbf{1}^T \boldsymbol{R}^{-1} \boldsymbol{r} \right) \left(\mathbf{1}^T \boldsymbol{R}^{-1} \mathbf{1} \right)^{-1} \right] \sigma^2, \tag{75}$$

where $\boldsymbol{Y}$ is the column vector of the response data, $\mathbf{1}$ is a column vector filled with ones. $\boldsymbol{R}$ is the correlation matrix whose elements, $R_{ij} = R(\mathbf{x}^i, \mathbf{x}^j)$, are defined by the correlation function. $\boldsymbol{r}^T$ is the correlation vector between the point $\mathbf{x}$ and the sampled data. Its elements $r_i = R(\mathbf{x}, \mathbf{x}^i)$ are also defined by the correlation function. The value of β is calculated by maximizing the natural log of the likelihood function

$$L = \frac{1}{(2\pi\sigma^2)^{n/2} \, |\boldsymbol{R}|^{1/2}} \exp \left[-\frac{(\boldsymbol{Y} - \mathbf{1}\beta)^T \boldsymbol{R}^{-1} (\boldsymbol{Y} - \mathbf{1}\beta)}{2\sigma^2} \right], \tag{76}$$

resulting in

$$\hat{\beta} = \left(\mathbf{1}^T \boldsymbol{R}^{-1} \mathbf{1} \right)^{-1} \left(\mathbf{1}^T \boldsymbol{R}^{-1} \boldsymbol{Y} \right) \tag{77}$$

$$\hat{\sigma}^2 = (\boldsymbol{Y} - \mathbf{1}\beta)^T \boldsymbol{R}^{-1} (\boldsymbol{Y} - \mathbf{1}\beta) / n. \tag{78}$$

$\boldsymbol{\theta}$ is a vector of element θ_m from Eq.73. These are called the hyper-parameters, and are found by maximizing the concentrated log in-likelihood function

$$\ln L = - \left(n \ln \hat{\sigma}^2 + \ln \boldsymbol{R} \right) / 2. \tag{79}$$

5.1.2 Expected Improvement

Given a data set of current sample points a kriging model can be used to find the most promising point to evaluate next in a adaptive sampling scheme.

If the model constructed to represent our data provides a predictive distribution for the response at any location, then it can be used to quantify the improvement over our current best sample. Such a criterion is known as the expected improvement [61],

75

and it was initially developed in the context of gradient-free optimization of black-box functions with probabilistic surrogate models.

The general idea behind expected improvement is to take advantage of the response predictive distribution to find the best new point on which conduct the next analysis, given the current data. Consider the problem of minimizing: $y(x)$ respect to x given the data $\mathcal{D} = \{(y_i, x_i) \mid i = 1, \ldots, n\}$. For a Gaussian process model, at any test point x^*, a predictive normal distribution with mean $\hat{y}$ and variance $\hat{s}^2$ is available as shown in the vertical direction of Fig. 10. It is noted that significant part of the predictive distribution falls below the current best sample as shown by the shaded area. The expectation of the prediction at any location x respect to our current best sample can be quantified. This is known as the expected improvement criterion, $E[I]$.

If y_{min} is our current best response, the improvement at any arbitrary point x is defined as

$$I(x) = \max(y_{min} - f, 0). \tag{80}$$

Then, the expected improvement is simply the expectation of I and it is given as follow

$$E[I(\mathbf{x})] = E[\max(y_{min} - f, 0)] = \int_{-\infty}^{y_{min}} (y_{min} - f)\, \mathcal{N}(\hat{f}, \hat{s}^2)\, df + \int_{y_{min}}^{\infty} (0)\, \mathcal{N}(\hat{f}, \hat{s}^2)\, df.$$

where $\mathcal{N}$ is a normal probability density distribution with mean and variance $\hat{f}$, and $\hat{s}^2$, respectively. Further developing the previous equation, it becomes

$$E[I(\mathbf{x})] = \int_{-\infty}^{y_{min}} (y_{min} - f)\, \frac{1}{\hat{s}}\, \phi\left(\frac{f - \hat{f}}{\hat{s}}\right) df + \int_{y_{min}}^{\infty} (0)\, \frac{1}{\hat{s}}\, \phi\left(\frac{f - \hat{f}}{\hat{s}}\right) df.$$

In the previous equation, the second integral in the above equation vanishes. Then, the equation has the following closed form:

$$E[I(\mathbf{x})] = \left(y_{min} - \hat{f}\right) \Phi\left(\frac{y_{min} - \hat{f}}{\hat{s}}\right) + \hat{s}\phi\left(\frac{y_{min} - \hat{f}}{\hat{s}}\right), \tag{81}$$

where Φ and ϕ are the standard normal cumulative distribution and the standard normal density function, respectively.

$$
\begin{aligned}
\phi(t) &= \frac{1}{\sqrt{2\pi}} \exp\left(-\frac{t^2}{2}\right) \\
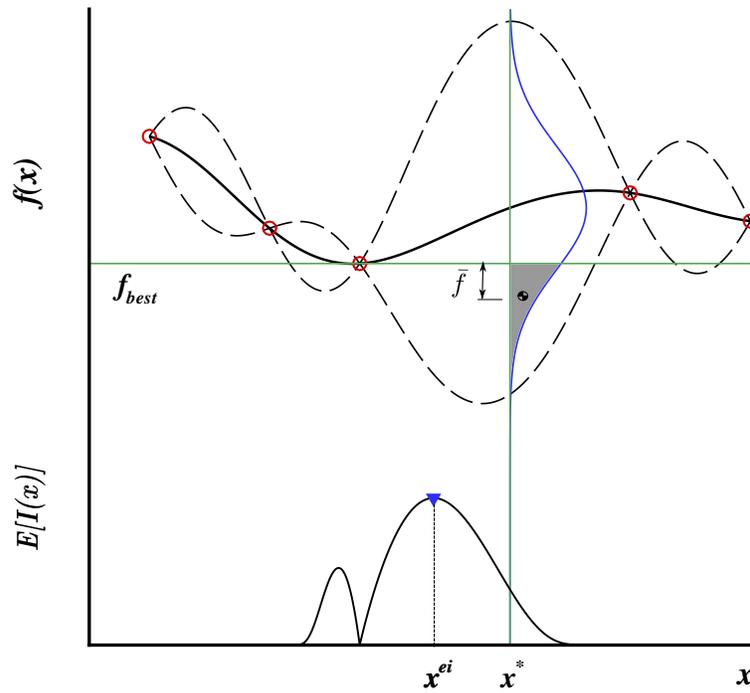\Phi(t) &= \frac{1}{2}\left[1 + \operatorname{erf}\left(\frac{t}{\sqrt{2}}\right)\right].
\end{aligned}
$$

Figure 10: Expected improvement

The expected improvement expresses how much the current best point can be improved at any location x. Therefore, it is of interest to find the location where the expected improvement is maximum. This location in turn serves as a new sample point x^{ei}. As a result, this criteria guides the sampling process towards more likely regions while searching for a global minimum. This situation is also illustrated in Figure 10 where the $E[I(x)]$ is plotted in the lower part of the figure, and its maximum location is shown. It must also be noted that the expected improvement is maximum

77

when the value of the mean prediction of the model, $\hat{f}$, is less than or close to the current best response, f_{best}, and the predictive standard deviation, $\hat{s}$, is large. Conversely, the expected improvement is almost negligible if the mean of the model prediction is higher and the predictive standard deviation is small.

Another interpretation of the expectation of improvement is from a geometrical standpoint. Let $\hat{f}$ represent the centroid distance from the current best response f_{best}, and $P[I]$ represent the shaded area; these are shown in Fig.10. Then, $E[I(x)]$ can be seen as the first moment of the shaded area respect to the horizontal line through the current best response. This first moment can be calculated as the product of the shaded area and its centroid distance from the current best response

$$E[I(\mathbf{x})] = \bar{f}\,P[I]. \tag{82}$$

The shaded area, $P[I]$, expresses the probability of improving over the minimum value of the current data at the location, and it is expressed as

$$P[I(\mathbf{x})] = P(f(\mathbf{x}) < f_{min}) = \int_{-\infty}^{f_{min}} \frac{1}{\hat{s}}\,\phi\left(\frac{f - \hat{f}}{\hat{s}}\right)\,df. \tag{83}$$

This integral has also a closed form

$$P[I(\mathbf{x})] = P(f(\mathbf{x}) < f_{min}) = \Phi\left(\frac{f_{min} - \hat{f}}{\hat{s}}\right). \tag{84}$$

This geometrical interpretation will be important in the next section to understand the derivation of the expected improvement criteria for multi-objective problems.

5.1.3 Multi-objective expected improvement

So far, the expected improvement has been explained only for single objective problems, but recall that the robust design formulation is multi-objective: maximize mean and minimize the variance.

The multi-objective expected improvement (MO-EI) is a measure for adaptive sampling that involves two objectives. It was developed by Keane [62] and is also

adopted in this work. Consider an initial Pareto set, $\mathcal{D}^* = \{(f_i^*, g_i^*) \,|\, i = 1, \ldots, m\}$, from an initial data set of two different objectives functions f and g. By assuming independence between the two objectives, they can be modeled by the prediction of Gaussian processes. The join probability distribution function $\rho(f, g)$ for the predicted responses is then simply defined as the product of the individual distributions as follow
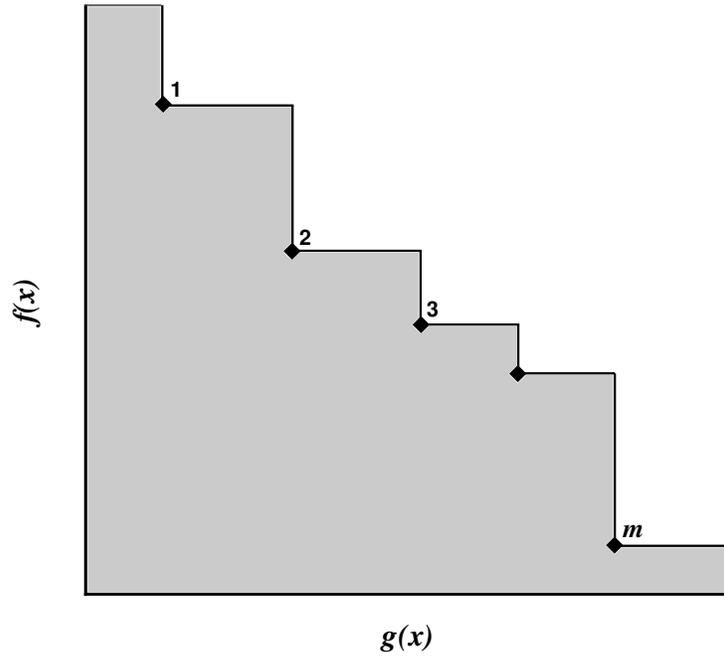

Figure 11: Multi-objective expected improvement

$$\rho(f, g) = \rho(f)\,\rho(g) = \mathcal{N}(\hat{f},\, \hat{s}_f^2)\,\mathcal{N}(\hat{g},\, \hat{s}_g^2). \tag{85}$$

The probability of a single point $(\,f(\mathbf{x}), g(\mathbf{x})\,)$ of augmenting or dominating the current Pareto set is defined as

$$P[I(\mathbf{x})] = P\left(f(\mathbf{x}) < f^* \cup g(\mathbf{x}) < g^*\right). \tag{86}$$

The right hand side of the previous equation is defined by integrating the joint probability distribution function $\rho(f, g)$ over the shaded area located at the left of the

current Pareto set as shown in figure 11.

$$P[I(\mathbf{x})] = \int_{-\infty}^{f_1^*} \int_{-\infty}^{\infty} \rho(f,g)\, df\, dg + \sum_{i=1}^{m-1} \int_{f_i^*}^{f_{i+1}^*} \int_{-\infty}^{g_i^*} \rho(f,g)\, df\, dg$$
$$+ \int_{f_m^*}^{\infty} \int_{-\infty}^{f_m^*} \rho(f,g)\, df\, dg. \tag{87}$$

The above integrals have closed form as shown below

$$P[I(\mathbf{x})] = \Phi(z_{f_1^*}) + \sum_{i=1}^{m-1} \left[\Phi(z_{f_{i+1}^*}) - \Phi(z_{f_i^*}) \right] \Phi(z_{g_i^*})$$
$$+ \left[1 - \Phi(z_{f_m}) \right] \Phi(z_{g_m}), \tag{88}$$

where $\Phi(.)$ represents the standard normal cumulative distribution, whereas z_f and z_g are defined as follow

$$z_{f_k^*} = \frac{f_k^* - \hat{f}}{\hat{s}_f} \tag{89}$$

$$z_{g_k^*} = \frac{g_k^* - \hat{g}}{\hat{s}_g}. \tag{90}$$

Similar to the single objective expected improvement, the multi-objective improvement is defined as the product of the probability of improvement and the distance to the centroid area as follow

$$E[I(\mathbf{x})] = P[I(\mathbf{x})] \sqrt{(\bar{f}(\mathbf{x}) - f_{min}^*)^2 + (\bar{g}(\mathbf{x}) - g_{min}^*)^2}, \tag{91}$$

where (f_{min}^*, g_{min}^*) is the closet member of the Pareto set $\mathcal{D}^*$ to the centroid; $\bar{f}$ and $\bar{g}$ are the coordinates, in objective space, of the centroid and are defined as

$$\bar{f}(x) = \left(\int_{-\infty}^{f_1^*} \int_{-\infty}^{\infty} \hat{f}\, \rho(f,g)\, df\, dg + \sum_{i=1}^{m-1} \int_{f_i^*}^{f_{i+1}^*} \int_{-\infty}^{g_i^*} \hat{f}\, \rho(f,g)\, df\, dg \right.$$
$$\left. + \int_{f_m^*}^{\infty} \int_{-\infty}^{f_m^*} \hat{f}\, \rho(f,g)\, df\, dg \right) / P[I] \tag{92}$$

$$\bar{g}(x) \;=\; \left(\int_{-\infty}^{f_1^*} \int_{-\infty}^{\infty} \hat{g}\, \rho(f,g)\, df\, dg + \sum_{i=1}^{m-1} \int_{f_i^*}^{f_{i+1}^*} \int_{-\infty}^{g_i^*} \hat{g}\, \rho(f,g)\, df\, dg \right.$$

$$\left. + \int_{f_m^*}^{\infty} \int_{-\infty}^{f_m^*} \hat{g}\, \rho(f,g)\, df\, dg \right) \Big/ P[I] \tag{93}$$

This situation is illustrated in figure 12 in which the centroid coordinate as well as its distance to closest member are shown. Working out the integrals in the above equation, the centroid coordinates have the following closed form

$$\bar{f}(x) \;=\; \Big\{ \hat{f}\, \Phi(z_{f_1^*}) - \hat{s}_f\, \phi(z_{f_1^*}) +$$

$$\sum_{i=1}^{m-1} \left[\hat{f}\, (\, \Phi(z_{f_{i+1}^*}) - \Phi(z_{f_i^*})\,) - \hat{s}_f\, (\, \phi(z_{f_{i+1}^*}) - \phi(z_{f_i^*})\,) \right] \Phi(z_{g_i^*})$$

$$+ \left[\hat{f}\, (\, 1 - \Phi\, (z_{f_m})\,) + \hat{s}_f\, \phi\, (z_{f_m}) \right] \Phi\, (z_{g_m}) \Big\} \Big/ P[I], \tag{94}$$

$$\bar{g}(x) \;=\; \Big\{ \hat{g}\, \Phi(z_{f_1^*}) +$$

$$\sum_{i=1}^{m-1} \left[\Phi(z_{f_{i+1}^*}) - \Phi(z_{f_i^*}) \right] \left[\hat{g}\, \Phi(z_{g_i^*}) - \hat{s}_g\, \phi(z_{g_i^*}) \right]$$

$$+ \left[1 - \Phi(z_{f_m^*}) \right] \left[\hat{g}\, \Phi(z_{g_m^*}) - \hat{s}_g\, \phi(z_{g_m^*}) \right] \Big\} \Big/ P[I], \tag{95}$$

where $\phi(.)$ and $\Phi(.)$ represent the standard normal distribution function and its cumulative distribution, respectively; whereas z_f and z_g are defined according to equations 89 and 90, respectively.

5.1.4 Dependent or correlated Gaussian process

The Gaussian processes discussed above considers a single output. Nevertheless, there may be cases in which a model have several outputs, or a single output can be described by several models. The latter, for instance, can be the case in which a physical model can be described by several level of fidelity. One mean to deal with these cases is to treat every output independently and model each of them with
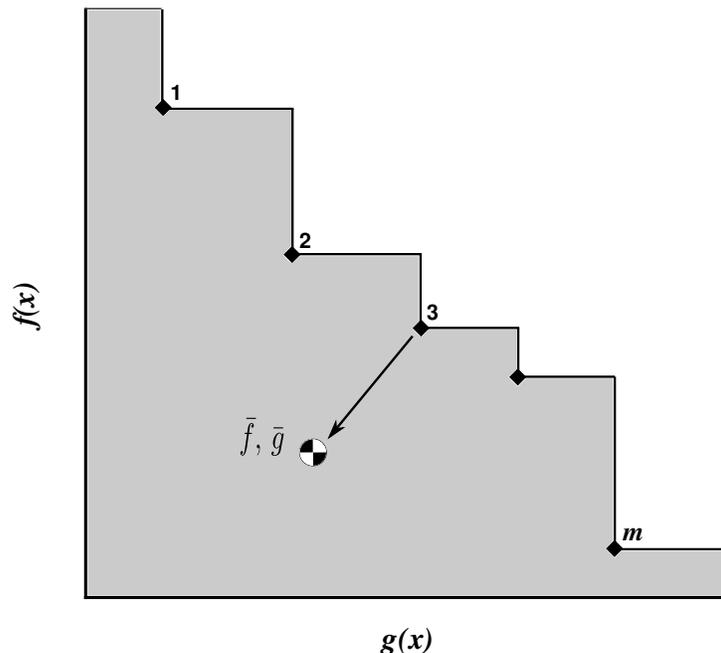
81

Figure 12: Multi-objective expected improvement

a Gaussian process. Such a treatment is known as multi-kriging [97]. However, a model that assumes independence can not exploit any similarities. For those cases, formulations that are capable of correlating model outputs are advantageous. Such as formulation are known as dependent or correlated Gaussian processes.

Dependent Gaussian processes has been recently introduced in the machine learning community [13]. Most of the work in this field relay on convolution processes for defining the covariance functions [13, 5]. Although this framework is mathematically elegant, there are parameters and functions to be defined, and thus this may limit its practicality for more general problems. An early type of methods that correlates model outputs are those from the geostatistics community. Most of the methods are based on the linear model of coreogionalization (LMC) [49]. In these methods, the outputs are assumed to be linear combinations of a set of one or more "random functions". Methods like co-kriging [24] are formulated by this approach.

In the present study a specific implementation of co-kriging by Forrester *et al.* [36] is adopted. This implementation has been successfully applied before to deterministic optimization of a civil aircraft wing [36], and to the blending of experimental and computational data [66]. A brief description of this co-kriging formulation is next presented.

5.1.4.1   co-kriging model

Consider two different output functions : a high fidelity, y_h, and a low fidelity, y_l with data defined over points $\boldsymbol{X}_h$ and $\boldsymbol{X}_l$, respectively. The combined set of data for these two model is represented as follow :

$$\boldsymbol{X} = \begin{bmatrix} \boldsymbol{X}_l \\ \boldsymbol{X}_h \end{bmatrix},$$

with responses

$$\boldsymbol{Y} = \begin{bmatrix} \boldsymbol{Y}_l \\ \boldsymbol{Y}_h \end{bmatrix}.$$

It is assumed that the locations of the high fidelity data is a subset of the low fidelity data, $\boldsymbol{X}_h \in \boldsymbol{X}_l$.

By assuming an additive scaling model, the high fidelity data can be represented by a sum of the low fidelity model "l" multiplied by a scaling factor ρ and another process y_Δ which expresses the difference between "y_h" and "$\rho\,y_l$." This is represent as follow :

$$y_h = \rho\,y_l + y_\Delta. \tag{96}$$

A central difference with kriging is that in the co-kriging model the covariance matrix between the Gaussian processes for the outputs y_h and y_l has a more complex structure. This involves not only auto-covariance matrices, but also cross-covariance

matrices

$$C = \begin{bmatrix} C_{ll} & C_{lh} \\ C_{hl} & C_{hh} \end{bmatrix},$$

where the auto-covariance matrices are defined by

$$C_{ll} = \sigma_l^2 \, R_l(X_l, X_l) \tag{97}$$

$$C_{hh} = \rho^2 \, \sigma_l^2 \, R_l(X_h, X_h) + \sigma_\Delta^2 \, R_\Delta(X_h, X_h), \tag{98}$$

and the cross-covariance matrix

$$C_{lh} = \rho \, \sigma_l^2 \, R_l(X_l, X_h). \tag{99}$$

In the above expression R_l and R_Δ are the correlation matrices. The elements of these matrices are defined similar as for Kriging (Eq. 73); however, the subscripts l and d refer to the hyperparameters θ_l and θ_Δ of the model l and Δ, respectively.

Independence is assumed between the Gaussian processes for the model of the low fidelity and the difference model. The parameters of the former model, β_l and σ_l^2, are found by maximizing its log likelihood function

$$\ln L_l = -\frac{1}{2} \left(n_l \ln \sigma_l^2 + \ln |R_l(X_l, X_l)| \right) - \tag{100}$$

$$\frac{1}{2} [\, Y_l - \mathbf{1} \, \beta_l \,]^T \, R_l^{-1}(X_l, X_l) \, [\, Y_l - \mathbf{1} \, \beta_l \,] \, \sigma_l^{-2}, \tag{101}$$

resulting in

$$\hat{\beta}_l = \left[\mathbf{1}^T \, R_l^{-1}(X_l, X_l) \, \mathbf{1} \right]^{-1} \, \left[\mathbf{1}^T R_l^{-1}(X_l, X_l) \, Y_l \right] \tag{102}$$

$$\hat{\sigma}_l^2 = \left[Y_l - \mathbf{1} \, \hat{\beta}_l \right]^T \, R_l^{-1}(X_l, X_l) \left[Y_l - \mathbf{1} \, \hat{\beta}_l \right] \, n_l^{-1}. \tag{103}$$

Substitution of the above two expressions for $\hat{\beta}_l$ and $\hat{\sigma}_l^2$ into the log likelihood function gives the concentrated ln-likelihood

$$\ln L_l = -\frac{1}{2} \left(n_l \ln \hat{\sigma}_l^2 + \ln |R_l(X_l, X_l)| \right). \tag{104}$$

The vector of hyperparameters $\boldsymbol{\theta}_l$ is found by maximizing this equation. The Gaussian process for the difference model is defined by data of the model "h" and "l" at the common locations $\boldsymbol{X}_h$ as follow:

$$\boldsymbol{Y}_{\boldsymbol{\Delta}} = \boldsymbol{Y}_h - \rho\,\boldsymbol{Y}_l(\boldsymbol{X}_h). \tag{105}$$

The ln-likelihood is then defined as

$$\ln L_{\Delta} \;=\; -\frac{1}{2}\left(\,n_h \ln \sigma_{\Delta}^2 + \ln|\boldsymbol{R}_{\boldsymbol{\Delta}}(\boldsymbol{X}_h,\boldsymbol{X}_h)|\,\right) -$$
$$\frac{1}{2}\,[\,\boldsymbol{Y}_{\boldsymbol{\Delta}} - \mathbf{1}\,\beta_{\Delta}\,]^T\,\boldsymbol{R}_{\boldsymbol{\Delta}}^{-1}(\boldsymbol{X}_h,\boldsymbol{X}_h)\,[\,\boldsymbol{Y}_{\boldsymbol{\Delta}} - \mathbf{1}\,\beta_{\Delta}\,]\,\sigma_{\Delta}^{-2}.$$

The parameters β_{Δ} and σ_{Δ}^2 which are found by maximizing the above function, and results in the following expressions :

$$\hat{\beta}_{\Delta} \;=\; \left[\mathbf{1}^T\,\boldsymbol{R}_{\boldsymbol{\Delta}}^{-1}(\boldsymbol{X}_h,\boldsymbol{X}_h)\,\mathbf{1}\right]^{-1}\left[\mathbf{1}^T\boldsymbol{R}_{\boldsymbol{\Delta}}^{-1}(\boldsymbol{X}_h,\boldsymbol{X}_h)\,\boldsymbol{Y}_{\boldsymbol{\Delta}}\right]$$
$$\hat{\sigma}_{\Delta}^2 \;=\; \left[\boldsymbol{Y}_{\boldsymbol{\Delta}} - \mathbf{1}\,\hat{\beta}_{\Delta}\right]^T\boldsymbol{R}_{\boldsymbol{\Delta}}^{-1}(\boldsymbol{X}_h,\boldsymbol{X}_h)\left[\boldsymbol{Y}_{\boldsymbol{\Delta}} - \mathbf{1}\,\hat{\beta}_{\Delta}\right]\,n_h^{-1}.$$

The vector of hyperparameters $\boldsymbol{\theta}_{\boldsymbol{\Delta}}$ and the scaling factor $\hat{\rho}$ are found by maximizing the concentrated ln-likelihood function which found by substituting the parameters $\hat{\beta}_{\Delta}$ and $\hat{\sigma}_{\Delta}^2$ into the ln-likelihood function

$$\ln L_{\Delta}^* = -\frac{1}{2}\left(\,n_h \ln \hat{\sigma}_{\Delta}^2 + \ln|\boldsymbol{R}_{\boldsymbol{\Delta}}(\boldsymbol{X}_h,\boldsymbol{X}_h)|\,\right). \tag{106}$$

5.1.4.2   co-kriging prediction

Predictions at new points are obtained by evaluating the following expression for the function mean and variance

$$\hat{f}_h \;=\; \hat{\beta} + \boldsymbol{c}^T\,\boldsymbol{C}^{-1}\left[\boldsymbol{Y} - \mathbf{1}\hat{\beta}\right] \tag{107}$$
$$\hat{s}_h^2 \;=\; \rho^2\,\sigma_l^2 + \sigma_{\Delta}^2 - \boldsymbol{c}^T\,\boldsymbol{C}^{-1}\,\boldsymbol{c}, \tag{108}$$

where the parameter β is calculated as follows

$$\hat{\beta} = \left[\mathbf{1}^T\,\boldsymbol{C}^{-1}\,\mathbf{1}\right]^{-1}\left[\mathbf{1}^T\boldsymbol{C}^{-1}\,\boldsymbol{Y}\right], \tag{109}$$

85

$\boldsymbol{C}$ is the co-kriging covariance matrix

$$
\boldsymbol{C} \;=\; \begin{bmatrix} \hat{\sigma}_l^2 \boldsymbol{R}_l(\boldsymbol{X}_l, \boldsymbol{X}_l) & \hat{\rho}\,\hat{\sigma}_l^2\,\boldsymbol{R}_l(\boldsymbol{X}_l, \boldsymbol{X}_l) \\[2mm] \hat{\rho}\,\hat{\sigma}_l^2 \boldsymbol{R}_l(\boldsymbol{X}_h, \boldsymbol{X}_l) & \hat{\rho}^2\,\hat{\sigma}_l^2\,\boldsymbol{R}_l(\boldsymbol{X}_h, \boldsymbol{X}_h) + \hat{\sigma}_\Delta^2\,\boldsymbol{R}_\Delta(\boldsymbol{X}_h, \boldsymbol{X}_h) \end{bmatrix}
$$

and the vector $\boldsymbol{r}$ is defined as

$$
\boldsymbol{r} \;=\; \begin{bmatrix} \hat{\rho}\,\hat{\sigma}_l^2\,\boldsymbol{r}_l(\boldsymbol{X}_l, \boldsymbol{X}) \\[2mm] \hat{\rho}^2\,\hat{\sigma}_l^2\,\boldsymbol{r}_l(\boldsymbol{X}_h, \boldsymbol{X}) + \hat{\sigma}_\Delta^2\,\boldsymbol{r}_\Delta(\boldsymbol{X}_h, \boldsymbol{X}) \end{bmatrix}
$$

5.2 gPC-SG based robust optimization

Several formulations for robust design optimization have been proposed [86]. Among them, one method for achieving robustness is to treat the optimization problem as multi-objective problem: maximizing some measure of mean performance and at the same time minimizing its variation. This type of formulation necessarily leads to study and construction of Pareto sets.

Currently, there are two popular approaches for constructing Pareto sets. The first and most simple method considers a weighting function to combine the mean performance and its variation into a single quantity. This quantity is next defined as the objective of a single optimization problem. Then, an optimization process is carried out to determine the design that satisfy the problem. By repeating this process several times with different values of the weighting functions, a Pareto set can be constructed. Although this approach take full advantage of well establish methods for deterministic optimization, it also present some problems. The weighting function is not know a priori. Moreover, it is difficult to know how to alter the weighting function, so enough spread in the Pareto front is achieved. The second more popular approach is those based on multi-objective genetic algorithms. Although these methods are able find the Pareto front accurately, the main drawback is that large numbers of evaluations of the objectives are needed.

In the presented gPC-SG based robust optimization strategies, a relatively more recent approach based on adaptive sampling for multi-objective problems is considered. More specifically, the multi-objective expected improvement [62] described in the previous section is adopted as a mean to efficiently approximate the Pareto front.

Under a multi-objective formulation, a robust design problem can be written as follow

$$\text{Minimize} \quad \boldsymbol{F} \; = \; [-\mu_{\mathcal{J}}, \, \sigma_{\mathcal{J}}]^T,$$

$$\text{Subject to}$$

$$\mathcal{P}\left[\mathcal{C}(\boldsymbol{X}, \boldsymbol{\xi}) \leq 0\right] \; \geq \; p$$

$$\boldsymbol{X}_l \leq \; \boldsymbol{X} \leq \boldsymbol{X}_u$$

where $\boldsymbol{F}$ is the vector objectives which is composed of the mean and standard deviation of the cost function $\mathcal{J}$, $\boldsymbol{X}$ is the vector of design variables whereas $\boldsymbol{\xi}$ is the vector of uncertain parameters, $\mathcal{C}$ is any constrain that, in general, can be not only function of the design variables, but also of the stochastic variables. If this is the case, the constrain must be expressed as inequality of the probability of the constrain be greater than a certain threshold value p. Finally, $\boldsymbol{X}_l$ and $\boldsymbol{X}_u$ are the lower and upper limits of the design vector, respectively.

5.2.1 Single level gPC-SG based robust optimization

In the single level gPC-SG based robust optimization strategy, the optimization objectives are approximated by Gaussian processes modeling the mean performance and variation of the cost function $\mathcal{J}$, i.e

$$\mu_{\mathcal{J}} \; \sim \; \mathcal{N}(\hat{\mu}_{\mathcal{J}}, \hat{s}^2_{\mu_{\mathcal{J}}}),$$

$$\sigma_{\mathcal{J}} \; \sim \; \mathcal{N}(\hat{\sigma}_{\mathcal{J}}, \hat{s}^2_{\sigma_{\mathcal{J}}}),$$

where $\hat{\mu}_{\mathcal{J}}$ and $\hat{\sigma}_{\mathcal{J}}$ are the mean predictor of the GP describing the mean and standard deviation of the cost function, whereas $\hat{s}_{\mu_{\mathcal{J}}}$ and $\hat{s}^2_{\sigma_{\mathcal{J}}}$ express the uncertainty of the respective GP.

The data of these statistical moments ($\mu_{\mathcal{J}}$ and $\sigma_{\mathcal{J}}$) are obtained by the gPC-SG uncertainty propagation approach described in the previous chapter. In these approach the cost function $\mathcal{J}(\boldsymbol{X}, \boldsymbol{\xi})$ is represented by a generalized polynomial chaos expansion and the first two moments are obtained by taking expectation of the expansion, resulting in

$$
\begin{aligned}
\mu_{\mathcal{J}} &= \alpha_0, \\
\sigma_{\mathcal{J}}^2 &= \sum_{i=1}^{P} \alpha_i^2 \langle \Phi_i^2 \rangle.
\end{aligned}
$$

The Pareto front approximation method is carried by the the multi-objective expected improvement criterion (*MO-EI*) described earlier in this chapter. The two objectives f and g as defined in the *MO-EI* section are taken as the mean and the standard deviation of the cost function, i.e. :

$$
\begin{aligned}
f &= \mu_{\mathcal{J}} \\
g &= \sigma_{\mathcal{J}}.
\end{aligned}
$$

By using the predictive capabilities of the Gaussian processes for both objectives, the *MO-EI* function is maximized. The coordinate in design space having this maximum is the most likely point to increase or dominate the current Pareto set, and hence it is taken as the next sample point. The procedure involved in this strategy is summarized in algorithm 1.

5.2.2 Bi-level gPC-SG based robust optimization

In the bi-level gPC-SG based robust optimization approach, two uncertainty propagation methods with different levels of accuracy are considered. A low fidelity UP may be inaccurate, but its computational cost is low. In contrast, a high fidelity UP is accurate; however, its computational cost can be high. The main idea is that the use of data from a low UP method can help to correct the data of high fidelity UP.

As a result, less use of the high fidelity UP is expected. This in turn may reduced the number of function calls of analysis codes compared to the single level strategy.

A bi-fidelity representation of the mean and standard deviation of the cost function $\mathcal{J}$ is achieved via an additive scaling model for each moment as follow

$$\mu_{\mathcal{J}_h} = \rho\,\mu_{\mathcal{J}_l} + \mu_\Delta, \tag{110}$$

$$\sigma_{\mathcal{J}_h} = \rho\,\sigma_{\mathcal{J}_l} + \sigma_\Delta, \tag{111}$$

where the subindex h and l express the source of the data either from the high or low UP method, the subindex Δ, however, expresses the difference between the high fidelity data and the low fidelity data times a scaling factor ρ. Note that the above equations are the equivalent to the data modeling for the co-kriging model (Eq.96).

Next, four Gaussian processes are defined for approximating the data of the low fidelity UP (l) and the difference data (Δ).

$$\mu_{\mathcal{J}_l} \sim \mathcal{N}(\hat{\mu}_{\mathcal{J}_l}, \hat{s}^2_{\mu_{\mathcal{J}_l}}),$$

$$\sigma_{\mathcal{J}_l} \sim \mathcal{N}(\hat{\sigma}_{\mathcal{J}_l}, \hat{s}^2_{\sigma_{\mathcal{J}_l}}),$$

$$\Delta\mu_{\mathcal{J}} \sim \mathcal{N}(\hat{\Delta}\mu_{\mathcal{J}}, \hat{s}^2_{\Delta\mu_{\mathcal{J}}}),$$

$$\Delta\sigma_{\mathcal{J}} \sim \mathcal{N}(\hat{\Delta}\sigma_{\mathcal{J}}, \hat{s}^2_{\Delta\sigma_{\mathcal{J}}}).$$

These Gaussian process are related to the high fidelity h data by the co-kriging formulation. This results in another Gaussian process for the high fidelity data :

$$\mu_{\mathcal{J}_h} \sim \mathcal{N}(\hat{\mu}_{\mathcal{J}_h}, \hat{s}^2_{\mu_{\mathcal{J}_h}}),$$

$$\sigma_{\mathcal{J}_h} \sim \mathcal{N}(\hat{\sigma}_{\mathcal{J}_h}, \hat{s}^2_{\sigma_{\mathcal{J}_h}}),$$

where $\hat{\mu}_{\mathcal{J}_h}$ and $\hat{s}^2_{\mu_{\mathcal{J}_h}}$ are the predictor and data error of the cost function mean $\mu_{\mathcal{J}}$, whereas $\hat{\sigma}_{\mathcal{J}_h}$ and $\hat{s}^2_{\sigma_{\mathcal{J}_h}}$ are the predictor and data error of the cost function deviation $\sigma_{\mathcal{J}}$. These predictors and data error are calculating according to co-kriging prediction equations (equations 107 and 108).

The high fidelity data, in general, can be obtained from any accurate method such as Monte Carlo. In this work, however, a UP strategy based on the generalized

polynomial chaos (gPC) was presented. This approach was shown to accurately propagate uncertainties, but a fraction of computational cost of Monte Carlo methods. Because of these, the gPC-SG strategy is chosen as the high fidelity UP. Again the first two moments are giving by the following expressions:

$$
\begin{aligned}
\mu_{\mathcal{J}_h} &= \alpha_0, \\
\sigma^2_{\mathcal{J}_h} &= \sum_{i=1}^{P} \alpha_i^2 \langle \Phi_i^2 \rangle.
\end{aligned}
$$

There are several choices for the low fidelity uncertainty propagation method. The choice of the low UP method should consider the computational cost. It desirable to keep this cost as low as possible. Because of this, local expansion (LE) based method stands as the best choice since its cost depends only on the cost of computing the derivatives respect to the stochastic variables. However, other choices are also possible such as the unidimensional reduction method (UDR) described in chapter 2. The main point is to keep the cost close to the cost of the local based methods. In this work, a LE method is used to usefulness of the bi-level approach with canonical function in the next section. In chapter VI, the gPC-SG approach with level one ($l = 1$) of the sparse grid integration method is considered as the low fidelity UP. This level of the sparse grid integration ensure its lowest computational cost that is similar to calculating derivatives with a central difference scheme. The main advantage of using the gPC-SG with $l = 1$ of the SP integration technique is that no extra computation are needed for the low level UP as is the case with the LE method. This is due to the nested nature of the sparse grid integration method.

Similar to the single level approach, in the bi-level approach, the Pareto front approximation method is carried by the the multi-objective expected improvement criterion (*MO-EI*). The robust optimization objectives f and g section are taken as

the mean and the standard deviation of the cost function, i.e. :

$$f = \mu_{\mathcal{J}_h}$$

$$g = \sigma_{\mathcal{J}_h}.$$

Since the moments are modeled by using Gaussian processes, the *MO-EI* function can be maximized. The coordinate in design space having this maximum is the most likely point to increase or dominate the current Pareto set, and hence it is taken as the next sample point. Algorithm 2 summarizes the procedure of performing robust design with the bi-level strategy.

5.2.3 Stopping criteria

Several strategies for stopping optimization problems have been proposed. For instance, a threshold based criteria was defined in [61] in which the expected maximum improvement function falls below a determined value. This criteria, however, can be deceived if the particular data leads to a very thin variance and hence to a very small value of the expected improvement. Therefore, the algorithm can be terminated prematurely.

Instead of a general stopping rule, one may find more useful to adopt a criteria based on the particular problem of interest. For instance, the expected improvement can be run until a limit number of samples is reached. This is argument was made in [67] as a more realistic stand for early design since the interest is to glean information about favorable regions of the design space from a limit computational budget rather than the global optimum itself.

The latest criteria is adopted in the presented work since very often designers are constrained by the available computational power, or a time frame for completing analysis.

Algorithm 1: Single-level robust design strategy

---

1. Set chaos order, p, and sparse grid level, l.

2. Set initial sample for design space:

$$\mathbf{x} \;=\; \{x_1, \ldots, x_n\}$$

3. Calculate objectives for the initial design set by propagating uncertainties ($\boldsymbol{\xi}$)

$$
\begin{aligned}
\mu_{\mathcal{J}} &= \{\mu_{\mathcal{J}_1}, \ldots, \mu_{\mathcal{J}_n}\} \\
\sigma_{\mathcal{J}} &= \{\sigma_{\mathcal{J}_1}, \ldots, \sigma_{\mathcal{J}_n}\}
\end{aligned}
$$

where

$$
\begin{aligned}
\mu_{\mathcal{J}_k} &= \mu_{\mathcal{J}}(x_k, \boldsymbol{\xi}) = \alpha_0, \\
\sigma_{\mathcal{J}_k} &= \sigma_{\mathcal{J}}(x_k, \boldsymbol{\xi}) = \left(\sum_{i=1}^{P} \alpha_i^2 \langle \Phi_i^2 \rangle \right)^{1/2}, \quad k = 1, \ldots, n,
\end{aligned}
$$

is obtained by gPC-SG.

4. While $Niter < Niter_{max}$

   (a) Build independent GP models for $\mu_{\mathcal{J}}$ and $\sigma_{\mathcal{J}}$

   (b) Maximize multi-objective expected improvement, $MO-EI(\mathbf{x})$, for finding the next sample point x_{n+1}

   (c) Propagate uncertainties ($\boldsymbol{\xi}$) for the new design point

$$
\begin{aligned}
\mu_{\mathcal{J}_{n+1}} &= \mu_{\mathcal{J}}(x_{n+1}, \boldsymbol{\xi}) = \alpha_0, \\
\sigma_{\mathcal{J}_{n+1}} &= \sigma_{\mathcal{J}}(x_{n+1}, \boldsymbol{\xi}) = \left(\sum_{i=1}^{P} \alpha_i^2 \langle \Phi_i^2 \rangle \right)^{1/2}.
\end{aligned}
$$

   (d) Add new design point x_{n+1} to the design set

$$
\begin{aligned}
\mathbf{x} &= \{x_1, \ldots, x_{n+1}\} \\
\mu_{\mathcal{J}} &= \{\mu_{\mathcal{J}_1}, \ldots, \mu_{\mathcal{J}_{n+1}}\} \\
\sigma_{\mathcal{J}} &= \{\sigma_{\mathcal{J}_1}, \ldots, \sigma_{\mathcal{J}_{n+1}}\}
\end{aligned}
$$

   (e) $Niter = Niter + 1$

5. End

<div align="center">**Algorithm 2:** Bi-level robust design strategy</div>

1. Set chaos order, p, and sparse grid level, l.

2. Set initial sample for the design space, $(\mathbf{x}_h \in \mathbf{x}_l)$:

$$
\begin{array}{c|c}
\text{high fidelity } (h) & \text{low fidelity } (l) \\
\mathbf{x}_h = \{x_1, \ldots, x_{nh}\} & \mathbf{x}_l = \{x_1, \ldots, x_{nl}\}
\end{array}
$$

3. Calculate objectives for the initial design set by propagating uncertainties $(\boldsymbol{\xi})$

$$
\begin{array}{c|c}
\text{high fidelity } (h) & \text{low fidelity } (l) \\
\mu_{\mathcal{J}}^{h} = \{\mu_{\mathcal{J}_1}^{h}, \ldots, \mu_{\mathcal{J}_{nh}}^{h}\} & \mu_{\mathcal{J}}^{l} = \{\mu_{\mathcal{J}_1}^{l}, \ldots, \mu_{\mathcal{J}_{nl}}^{l}\} \\
\sigma_{\mathcal{J}}^{h} = \{\sigma_{\mathcal{J}_1}^{h}, \ldots, \sigma_{\mathcal{J}_{nh}}^{h}\} & \sigma_{\mathcal{J}}^{l} = \{\sigma_{\mathcal{J}_1}^{l}, \ldots, \sigma_{\mathcal{J}_{nl}}^{l}\}
\end{array}
$$

where the high fidelity UP is gPC-SG:

$$
\mu_{\mathcal{J}_k}^{h} = \mu_{\mathcal{J}}(x_k, \boldsymbol{\xi}) = \alpha_0,
$$

$$
\sigma_{\mathcal{J}_k}^{h} = \sigma_{\mathcal{J}}(x_k, \boldsymbol{\xi}) = \left(\sum_{i=1}^{P} \alpha_i^2 \langle \Phi_i^2 \rangle\right)^{1/2}, \quad k = 1, \ldots, n.
$$

and the low fidelity UP is either the LE method or gPC-SG $(l = 1)$

4. While $Niter < Niter_{max}$

   (a) Build independent correlated GP models for $\mu_{\mathcal{J}}^{h}$ and $\sigma_{\mathcal{J}}^{h}$

   (b) Maximize $MO - EI(\mathbf{x})$ for finding the next sample point x_{n+1}

   (c) Propagate uncertainties $(\boldsymbol{\xi})$ for the new design point

$$
\mu_{\mathcal{J}_{n+1}}^{h} = \mu_{\mathcal{J}}(x_{n+1}, \boldsymbol{\xi}) = \alpha_0,
$$

$$
\sigma_{\mathcal{J}_{n+1}}^{h} = \sigma_{\mathcal{J}}(x_{n+1}, \boldsymbol{\xi}) = \left(\sum_{i=1}^{P} \alpha_i^2 \langle \Phi_i^2 \rangle\right)^{1/2}.
$$

   (d) Add new design point x_{n+1} to the design set

$$
\begin{array}{c|c}
\text{high fidelity } (h) & \text{low fidelity } (l) \\
\mathbf{x}_h = \{x_1, \ldots, x_{nh+1}\} & \mathbf{x}_l = \{x_1, \ldots, x_{nl+1}\} \\
\mu_{\mathcal{J}}^{h} = \{\mu_{\mathcal{J}_1}^{h}, \ldots, \mu_{\mathcal{J}_{nh+1}}^{h}\} & \mu_{\mathcal{J}}^{l} = \{\mu_{\mathcal{J}_1}^{l}, \ldots, \mu_{\mathcal{J}_{nl+1}}^{l}\} \\
\sigma_{\mathcal{J}}^{h} = \{\sigma_{\mathcal{J}_1}^{h}, \ldots, \sigma_{\mathcal{J}_{nh+1}}^{h}\} & \sigma_{\mathcal{J}}^{l} = \{\sigma_{\mathcal{J}_1}^{l}, \ldots, \sigma_{\mathcal{J}_{nl+1}}^{l}\}
\end{array}
$$

   (e) $Niter = Niter + 1$

5. End

5.3 Canonical problems

In this section the performance of the proposed approaches is addressed on some pre-
liminary canonical problems. An algebraic function subjected to random coefficients
is considered as a test problem. This choice is made based on its simplicity on im-
plementation and time of execution. In the next chapter, the approaches are applied
to engineering test cases such as the robust optimization problem of an airfoil at low
Reynold number and the robust design of transonic wing of bussines jet.

Firstly, the performance of the gPC-SG approach is addressed by comparing the
first two moments with those obtained by a quasi-Monte Carlo (quasi-MC) method.
Moreover, the Pareto fronts obtained with both approaches are also compared.

Secondly, the single and bi-level gPC-SG based robust optimization method per-
formance are compared. Finally, the performance of the bi-level approach for different
degrees of uncertainty and non-linearity the random coefficients is presented. The aim
here is to give support to the third research question: *"how is the bi-level strategy
affected by levels of non-linearity and uncertainty?"*.

The algebraic test problem is two-dimensional in spacial variables, $\boldsymbol{X}$, and stochas-
tic variables, $\boldsymbol{\xi}$. The algebraic test problem is shown in equation 112, and is based
on a test problem for multi-objective problems presented in [34]; however, linear,
quadratic, cubic and mixed terms are added to the original test problem.

$$
\begin{aligned}
\mathcal{J}(\boldsymbol{X},\boldsymbol{\xi}) \;=\;\; & a_0 + a_1\, x_1\, x_2 + \; a_2\left[\mathcal{C}_1\, x_1 + \mathcal{C}_1\, x_2\right] + a_3\left[\mathcal{C}_1\, x_1^2 + \mathcal{C}_2\, x_2^2\right] \\[4pt]
& + a_4\left[\mathcal{C}_1\,(\,x_1 - 0.5\,)^3 + \mathcal{C}_1\,(\,x_2 - 0.5\,)^3\right] \\[4pt]
& + a_5\,\mathcal{C}_1\,\exp(-\frac{1}{4}\left[(x_1 - 1.25)^2 + (x_2 - 1.00)^2\right]\,) \\[4pt]
& + a_6\,\mathcal{C}_2\,\exp(-\frac{1}{4}\left[(x_1 + 1.25)^2 + (x_2 + 0.75)^2)\right]\,) \qquad (112)
\end{aligned}
$$

where a_i are constants. Randomness is introduced into the function, f, by uncertain
coefficients $\mathcal{C}_1(\xi_1)$ and $\mathcal{C}_2(\xi_2)$ which are functions of the random variables.

5.3.1 Computational cost comparison

In order to measure the effectiveness of the single and bi-level strategies, two metrics are defined to quantify the proximity of the non-dominated designs to the actual Pareto front. The actual Pareto front is always assumed to be obtained by a quasi-Monte Carlo method and multi-objective genetic algorithm (MO-GA). These two metrics are defined as follow :

1. The first one is the distance d of a non-dominated design to the actual Pareto front. This distance is defined as the minimum of the distances between a non-dominated design and the designs comprising the actual Pareto front. For a non-dominated design $(\mu_{\mathcal{J}}^k, \sigma_{\mathcal{J}}^k)$, the distance is defined as

$$d_k = \min \sqrt{(\mu_{\mathcal{J}}^k - \mu_{\mathcal{J}}^i)^2 + (\sigma_{\mathcal{J}}^k - \sigma_{\mathcal{J}}^i)^2}, \ \ i = 1, \ldots, N_a, \tag{113}$$

where N_a is the number of designs comprising the the actual front as calculated by the quasi-MC method.

2. The second metric is the average distance of the non-dominated set of designs to the actual Pareto front.

$$d_{avg} = \frac{1}{N^*} \sum_{k=1}^{N^*} d_k, \tag{114}$$

where N^* is the number of non-dominated design.

A non-dominated design is considered to lay on the actual Pareto front if its distance to the actual front is lower than a certain threshold. For this problem, the threshold is set to $d \leq \delta$.

5.3.2 gPC-SG performance

The gPC-SG strategy ability for estimating the statistical moments is first tested. Next, its accuracy for robust optimization is addressed. In order to avoid any effect of

the Pareto front approximation, the gPC-SG strategy is coupled to a multi-objective genetic algorithm.

The uncertain coefficients, $\mathcal{C}(\xi)$, of the analytical test case function are defined by the following functions :

$$\mathcal{C}_i^1 = \xi_i^2 + \frac{1}{2} \left[1 + \sin(12\,\xi_i) \right], \quad i = 1, 2. \tag{115}$$

The above function are dependend on ξ which are uniform random variables defined according to

$$\xi_i = U(\,\mu_{\xi_i} - \sqrt{3}\,\sigma_{\xi_i},\ \mu_{\xi_i} + \sqrt{3}\,\sigma_{\xi_i}\,),$$

where μ_ξ and σ_ξ are the random variable mean and the standard deviation with values given by

$$\mu_{\xi_i} = 0.25\,\pi$$

$$\sigma_{\xi_i} = 0.15\,\pi.$$

Comparisons between the gPC-SG and the quasi-Monte Carlo method are shown in figure 13. In this figure, contours of the mean (left column) and standard deviation (right column) of the analytical test function $\mathcal{J}(\boldsymbol{X}, \boldsymbol{\xi})$ are shown. The contours calculated by the gPC-SG are shown in figures 13(a) and 13(b) for a chaos order $p = 10$ and sparse grid integration level of $l = 3$. These parameters requires a number of sample points of 29 at every point of the $\boldsymbol{X}$ space. The quasi Monte Carlo contours are shown in figures 13(c) and 13(d) for a number of 2×10^3 sample points using a Halston sequence at every location in the $\boldsymbol{X}$ space. The cost for these approaches are also shown in table 8. It can be noticed that there is a good agreement between both the contour plots of the moments. Indeed, the contour plots seem to be almost identical. However, the gPC-SG is able obtain the moments at a fraction of the computational cost of the quasi-MC.

In order to quantify the agreement between the approaches, the percent error of the gPC-SG respect to the quasi-MC method is shown in figures 13(e) and 13(f). The
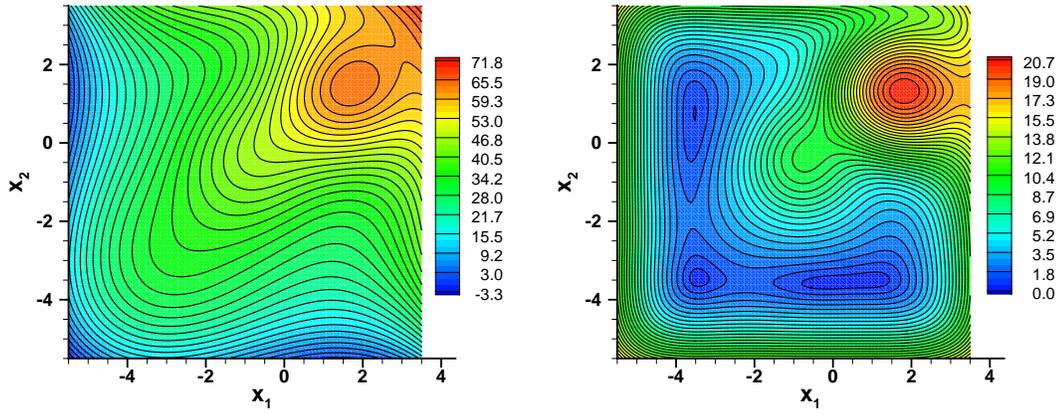
(a) Mean - gPC

(b) Std. deviation - gPC
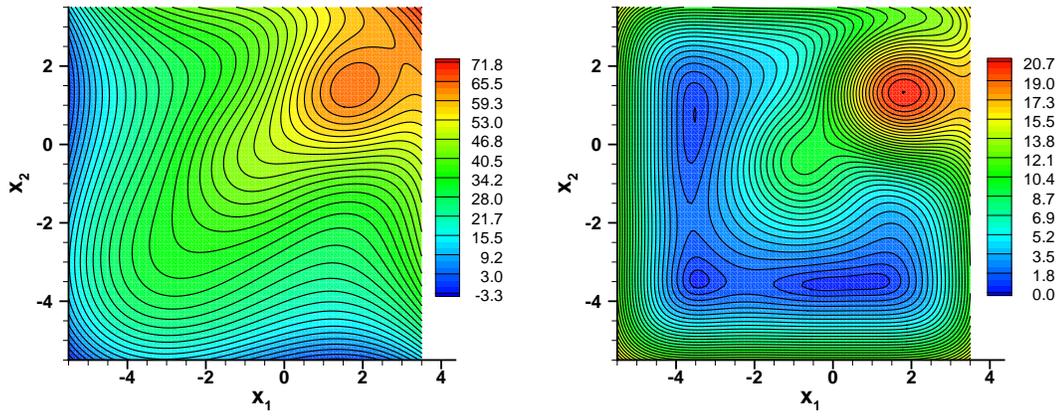
(c) Mean - qMC

(d) Std. deviation - qMC
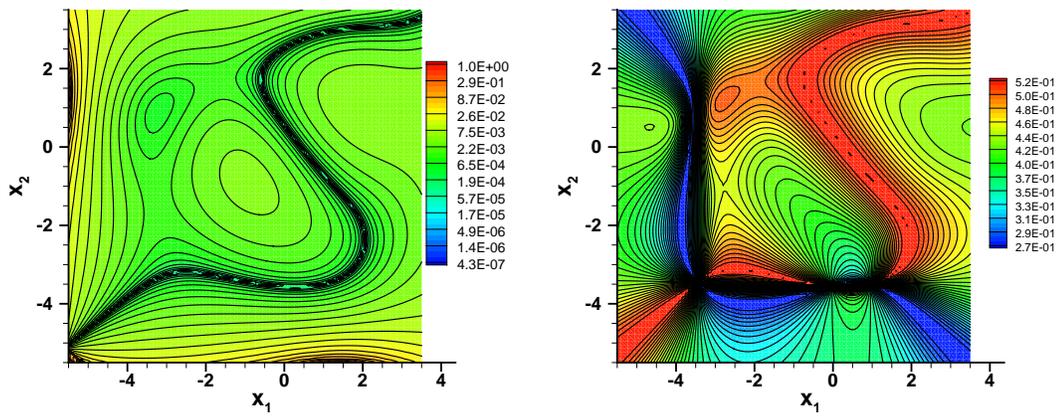
(e) Mean percent error (%)

(f) Std. deviation percent error (%)

Figure 13: Comparison of the mean (left column) and standard deviation (right column) of $\mathcal{J}$ using a quasi-MC and the gPC-SG approaches

contour of the mean of the test function has an average percent error 0.0070 %, while its maximum percent error is 0.9 %. The standard deviation has a mean percent error of 0.40 % and maximum percent error of 0.50 %. It is noticed that standard deviation has larger errors. This in general true for the gPC method as higher moments requires either higher chaos order, p, or higher integration levels, l. Nevertheless, as it will be seen next. The accuracy of the gPC-SG is accurate to approximate the Pareto front for multi-objective problems based on the mean and the standard deviation of the given cost function, $\mathcal{J}$.

Table 8: Computational cost of propagating uncertainties

UP method	Scaling cost	Computational cost
quasi-MC	–	2×10^3
gPC-SG ($p = 10$, $l = 3$)	–	29
LE (FOFM and FOSM)	$d + 1$	3

5.3.2.1 gPC-SG and MO-GA for robust optimization

Previously, it was shown the usefulness of gPC-SG to propagate uncertainties accurately at low computational cost compared to more expensive methods such as Monte Carlo. However, the main purpose in this work is to use the proposed UP strategy for robust design as formulated as a multi-objective optimization problem. Because of this, the gPC-SG method has to necessarily be tested for this type of problems. In order to isolate the effect of the Pareto front approximation method, the gPC-SG strategy is used in conjunction with a multi-objective genetic algorithm (MO-GA).

The multi-objective optimization problem is formulated as described earlier involving the simultaneous minimization of the negative of the mean and standard

deviation of the cost function $\mathcal{J}$

$$\text{Minimize} \quad \boldsymbol{F} \;=\; [\,-\mu_{\mathcal{J}}\,,\,\sigma_{\mathcal{J}}\,]^{T} \tag{116}$$

$$\text{Subject to}$$

$$\boldsymbol{X}_{l} \leq \;\boldsymbol{X}\; \leq \boldsymbol{X}_{u}.$$

In addition to gPC-SG and quasi-MC, a local expansion method (LE) such as FOFM and FOSM is considered. The set-up of the multi-objective genetic algorithm consists of an initial population of 800 samples in the $\boldsymbol{X}$ space, the population is 1000 and the number of generations is 200 for all the different UP methods considered.

The Pareto fronts and the non-dominated designs as calculated by MO-GA in conjunction with the three UP methods are shown in figure 14(a) and 14(b), respectively. It is noticed that the gPC-SG front lays the closest to the quasi-MC front which is considered to be the actual Pareto front. Indeed, the gPC-SG front, shown in red, overlays the actual front that is shown in black. This result is not coincidence, but rather expected since the contours of the first and second moment, shown in fig.13, for both UP methods are in good agreement.

The local expansion (LE) method, however, departs the most from the actual Pareto front. This method tends to overpredict the mean of the test function for any value of the standard deviation. It is clear that for this test case function the degree of non-linearity of the random coefficients, $\mathcal{C}$ (equation 115), is high enough to make invalid the locality assumption (Taylor expansion) in which the LE method is based on. As result, this UP method is not able to place more non-dominated points closer to the actual Pareto front.

5.3.3 Single-level and Bi-level gPC-SG performance

The main purpose of the above results was to shown the ability of the gPC-SG strategy for reproducing the results obtained by the quasi-MC for a robust design optimization problem. Although accurate, the use of multi-objective genetic algorithm (MO-GA)
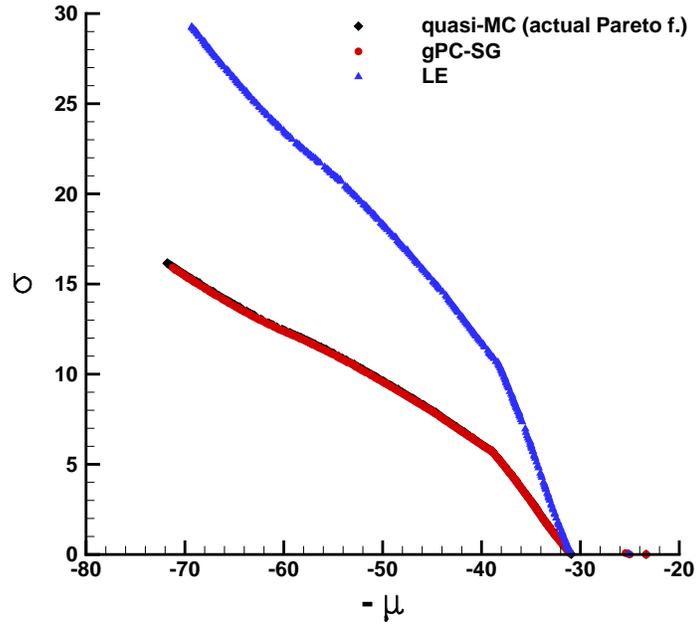
(a) Pareto front
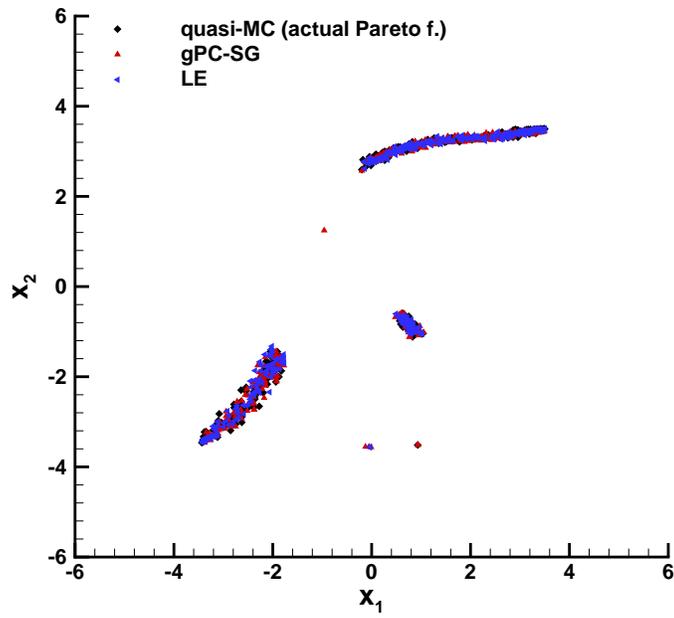
(b) Non-dominated designs

Figure 14: MO-GA based robust optimization of $\mathcal{J}$

suffer from long run times due to the large size of the population and also number of generations needed to find the Pareto front. Therefore, its cost can easily become intractable if the optimization objectives are expensive to evaluate.

In order to reduce the high computational cost in which robust design may incur, the single and bi-level approach proposed earlier are tested. Both strategies use the gPC-SG for uncertainty propagation and the multi-objective expected improvement (MO-EI) formulation for approximating the Pareto front. However, the bi-level strategy considers two levels of fidelity of the UP method.

The search of the Pareto front by employing both approaches is shown in figure 15 after 5, 10, and 20 adaptive samples. As a reference the Pareto front found by the quasi-MC and the MO-GA from the previous section is also shown and is considered the actual front. The single-level strategy has an initial number of points of 4 obtained by the gPC-SG approach with a chaos order $p = 10$, and sparse grid integration level $l = 3$. The bi-level strategy is initialized with the same 4 points of the single-level for the high fidelity UP, additionally 20 points of the low fidelity UP. These are obtained by a LE method (FOFM and FOSM) using a one-sided finite difference. The cost of propagating uncertainties for these three methods are shown in table 8. The kriging models for both, the single and bi-level strategies, are tuned after every new sample update by maximizing the corresponding likelihood function with a genetic algorithm.

From figure 15, it is noted that as the number of adaptive samples increases both strategies are able to place points closer to the actual Pareto front. For instance, by 5 adaptive samples as shown in fig. 15(a), the single-level strategy has already placed one sample in a near location of the actual front. By 10 adaptive samples, fig 15(c), there are 2 samples in a very near location of the actual front. Moreover, the non-dominated set symbolized by the blue circles is located closer to the Pareto front. By 20 adaptive samples, fig 15(e), there are a couple of samples lying exactly at the Pareto front and the non-dominated set is even closer to the actual front.

For the bi-level strategy, the non-dominated set are shown for adaptive samples of 5, 10, and 20 in figures 15(b), (d), & (f), respectively. At 5 adaptive samples, the bi-level strategy is able to place two samples exactly at the Pareto front. By 10 adaptive samples, the number of non-dominated design at the actual front has increased to 5, and the non-dominated set is located close to the actual front. Finally, for 20 adaptive samples there are 8 member of the non-dominated set lying at the actual Pareto front. In general, it is noticed that the bi-level strategy places more samples in the proximity of the actual Pareto front for any number of adaptive iterations.

5.3.3.1   Computational cost

Even though it was shown that the bi-level strategy approximates the actual Pareto front with fewer number of adaptive samples that the single-level strategy, this conclusion may turn out to be unfair since the bi-level strategy has initially more information than the single-level. Therefore, what actually needs to be measured is the computational cost which is given by the total number of function calls.

In order to quantify this cost, the two metrics:

i. Number of non-dominated designs lying at the actual Pareto front,

ii. Average distance of the non-dominated set to the actual Pareto front,

as defined in section 5.3.1 are used. For this problem the threshold for considering a non-dominated design as lying at the actual Pareto front is $\delta = 0.1$.

The number of non-dominated designs at the actual Pareto front as a function of the computational cost (number of function calls) is shown in figure 16(a). It must be noted that the bi-level has a higher initial cost since in addition to the high UP samples, it requires a larger samples of the low fidelity UP. Moreover, every adaptive sample has a slighlty higher cost due to the expense of calculating the objective with both levels of fidelity. Both strategies tend to place more non-dominated points as the number of adaptive samples increases. Nevertheless, it can be seen that for any
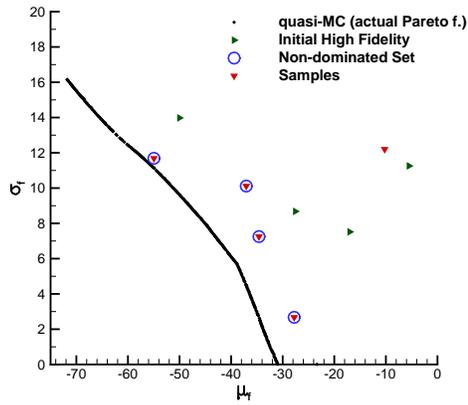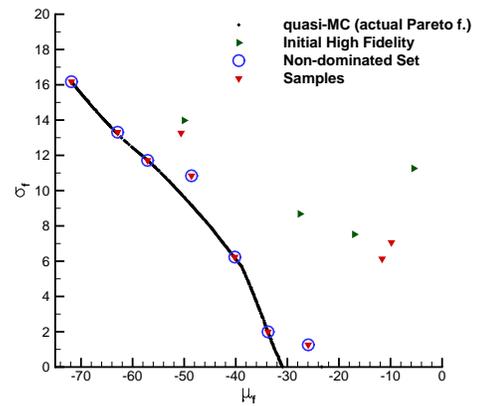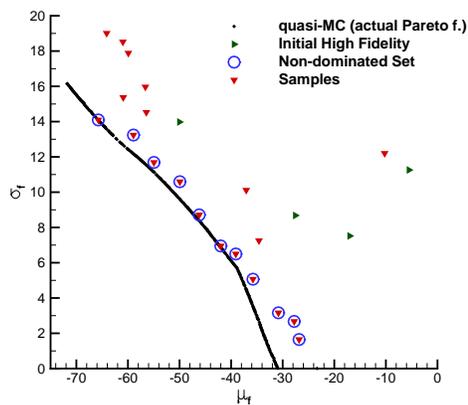
(a) Single-level, 5 samples
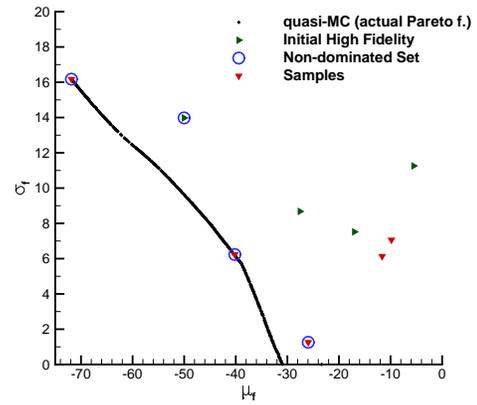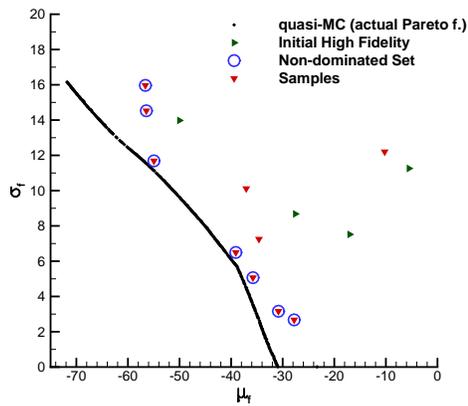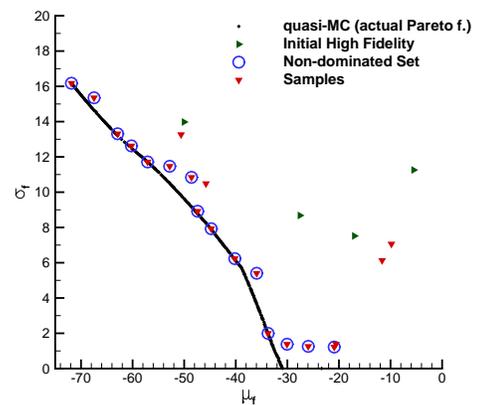
(b) Bi-level, 5 samples

(c) Single-level, 10 samples
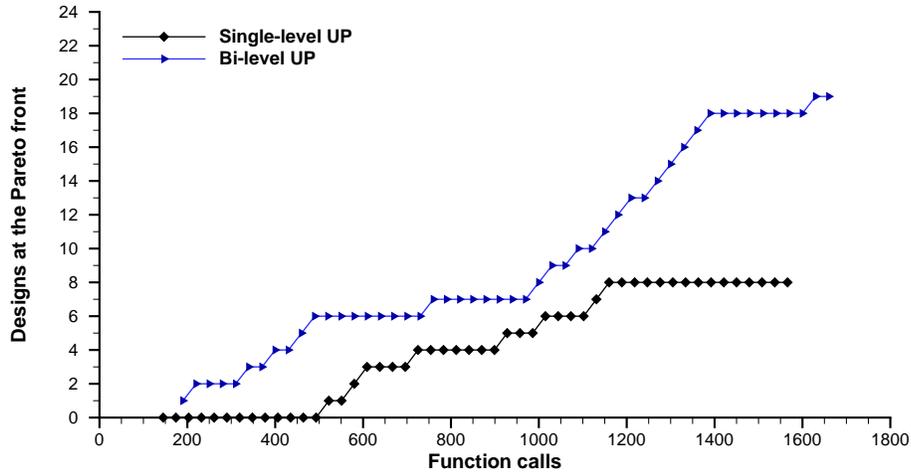
(d) Bi-level,10 samples

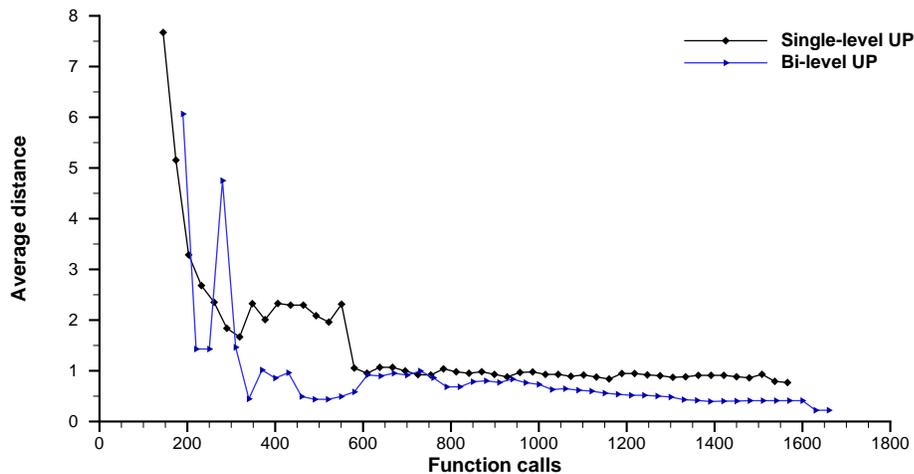(e) Single-level, 20 samples

(f) Bi-level, 20 samples

Figure 15: Non-dominated designs found by the single and bi-level gPC-SG based UP (figs. (a), (c), (e)), and the single level approach only (figs. (b), (d), (f))

determine budget (number of function calls), the bi-level strategy has more non-dominated points lying at the Pareto front.

(a) Designs at the Pareto front

(b) Average distance

Figure 16: Single and bi-level computational cost comparison for the random coefficients $\mathcal{C}^1$

Another mean to measure the effectiveness of the single and bi-level strategy is the average distance of the non-dominated set to the actual Pareto front. The average distance as a function of the computational cost is shown in figure 16(b). It is noticed that the general trend of this quantity is to decrease as the computational

cost of sampling adaptively increases although some variation can be seen for the fewer first adaptive samples. It is also noted that for the most part of the plot the average distance of the bi-level strategy is shorter than that of the single-level strategy. There is sudden increase of the average distance at the 4th adaptive sample. Behavior like this can happen with both approaches when a non-dominated point is placed in unexplored area of the objective space. If the point is still far from the actual Pareto front, the average distance increases.

5.3.4 Performance with degree of non-linearity and uncertainty

In this subsection the performance assessment with cost function, $\mathcal{J}$, non-linearity and degree of uncertainty is addressed. These tests serve as a mean to corroborate theoretical expected trends, and aim to give support to the predictions of the third research question: *"how is the bi-level strategy affected by levels of non-linearity and uncertainty?"*.

5.3.4.1 Degree of non-linearity

In order to test the performance with non-linearity, in addition to the random coefficient $\mathcal{C}^1$ defined previously in equation 115, the two following random coefficients:

$$\mathcal{C}_i^2 \quad = \quad \frac{1}{4}(\xi_i - b_0)^3 - 4\,(\xi_i - b_0) + 1 \tag{117}$$

$$\mathcal{C}_i^3 \quad = \quad \xi_i \tag{118}$$

are defined. The coefficient, $\mathcal{C}^2$, is a third order polynomial in the random variable ξ, whereas $\mathcal{C}^3$ is linear. Three different robust optimization cases are carried out with the analytical test function defined previously (equation 112) with each of these three coefficients.

The single level strategy only uses the gPC-SG UP method whereas the bi-level uses not only the gPC-SG, but also a LE method. For both strategies, the gPC-SG was

Table 9: gPC-SG computational cost

| SG level	Computational cost
$l = 3$	29
$l = 2$	13
$l = 1$	5

set up according to a chaos order of $p = 10$; however, the sparse grid integration level was set $l = 3$, $l = 2$, and $l = 1$ for the random coefficients $\mathcal{C}^1$, $\mathcal{C}^2$ and $\mathcal{C}^3$, respectively. The cost of the integration level, i.e. cost of the high fidelity propagator, is shown in table 9.

The effects of non-linearity with the computational cost are shown in figure 17 and 18. Similar to the previous test, the actual Pareto front was obtained by using a multi-objective genetic algorithm and quasi Monte Carlo method with the same settings of the previous example. The number of non-dominated points for the different coefficients, $\mathcal{C}$, are shown in figure 17. It is noted that as the non-linearity is decreased, the number of designs points at the Pareto front tend to get closer together for both strategies. For instance, for $\mathcal{C}^1$, the most non-linear coefficient shown in figure 17(a), the distance between the curves of the single and bi-level approach can be as high as 300 functions calls, whereas for the coefficient $\mathcal{C}^2$ shown in 17(b), the distance can be as high as 180 functions calls. For these two random coefficients, the computational cost of running the high fidelity propagator is such that bi-level approach offers the advantage of approximating the Pareto faster than the single level, i.e. fewer function calls are needed in order to place the same number of non-dominated points. Conversely, for the linear coefficient $\mathcal{C}^3$ shown in 17(c), the curves are located closer together, and both strategies seem to perform similarly.
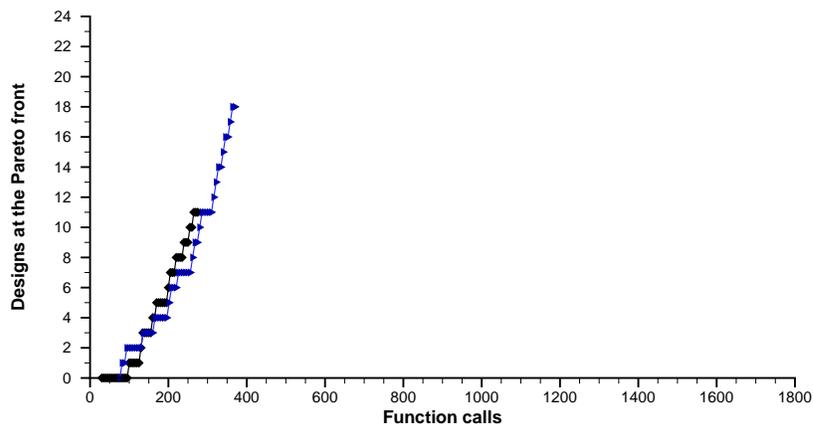
The average distance from the non-dominated set to the actual Pareto front is shown in figure 18. A shorter average distance of the bi-level strategy is observed for
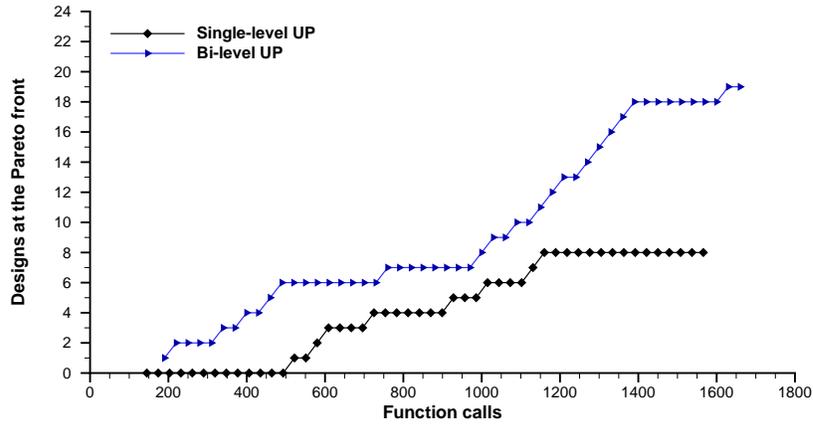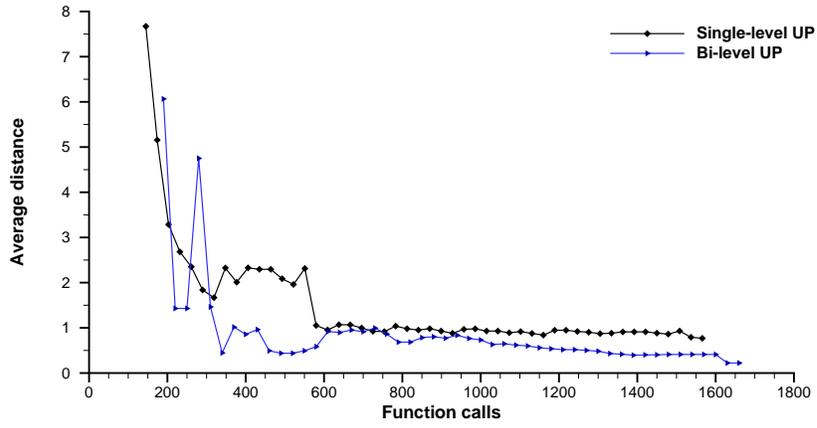
(a) Random coefficient: $\mathcal{C}^1$
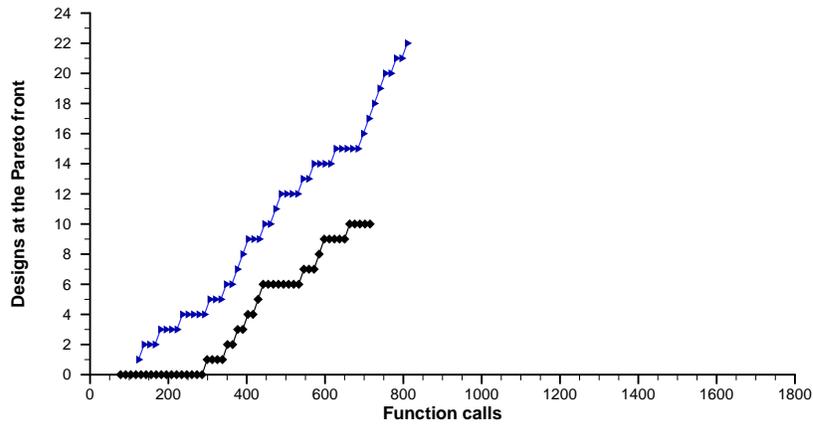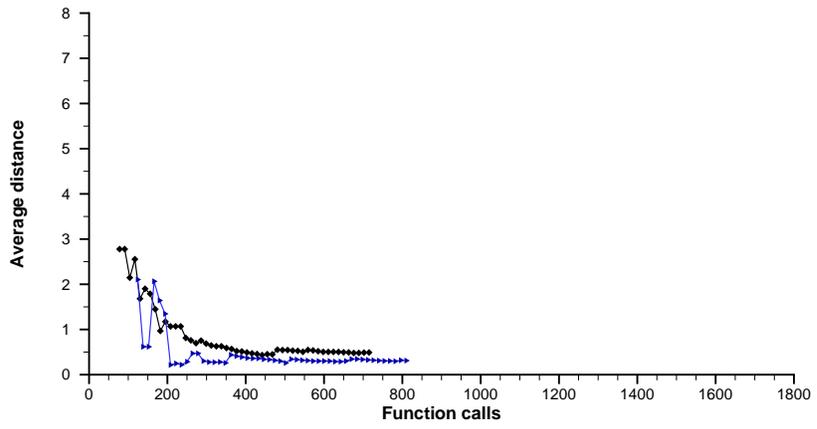

(b) Random coefficient: $\mathcal{C}^2$
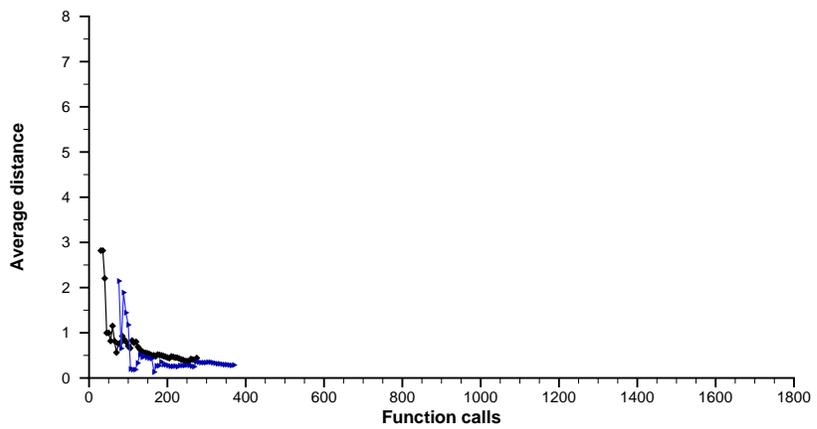

(c) Random coefficient: $\mathcal{C}^3$

Figure 17: Number of non-dominated designs at the Pareto front for different $\mathcal{C}$

(a) Random coefficient: $\mathcal{C}^1$

(b) Random coefficient: $\mathcal{C}^2$

(c) Random coefficient: $\mathcal{C}^3$

Figure 18: Average distance to the Pareto front for different $\mathcal{C}$

the case of the most non-linear coefficient $\mathcal{C}^1$ as shown in figure 18(a). The difference between the distance of both strategies is the largest for computational cost lower than 600 function calls. Although this difference decreases for larger computational cost, the distance of the bi-level strategy is still shorter than that of the single level strategy. A similar trend can be observed for the cubic coefficient $\mathcal{C}^2$ although the discrepancy of the average distance is much shorter for computational budgets larger than 350 function calls. For the linear coefficient $\mathcal{C}^3$, there distance of the bi-level strategy is still shorter; however, the discrepancy is much smaller.

5.3.4.2   Degree of uncertainty

The effects of the level of uncertainty are tested by varying the standard deviation. The results for the coefficient $\mathcal{C}^1$ obtained from the gPC-SG performance part (section 5.3.2) are taken as the baseline case, and two other cases consisting of 30% and 8% of the standard deviation are considered here.

The UP of the single-level and the high fidelity UP of the bi-level strategy is the gPC-SG with a chaos order of $p = 10$. However, each of these cases are carried out with different integration levels of the sparse grid. Levels of $l = 3$, 2, and 1 are considered for the 100%, 30%, and 8.5% cases, respectively. This choice of integration levels lead to computational costs that was already described in table 9.

The computational cost in which the two strategy incur are assessed in terms of the two metrics described earlier. For this purpose, it is considered that the actual Pareto front is that obtained by a multi-objective genetic algorithm and the quasi-Monte Carlo method.

The effects of the level of uncertainty with the computational cost is shown in figures 19 and 20. The number of non-dominated designs for the different cases are shown in figure 19. In general, as the level of uncertainty is decreased, the number of points at the Pareto front (curves) for each strategy tend to get closer. The average
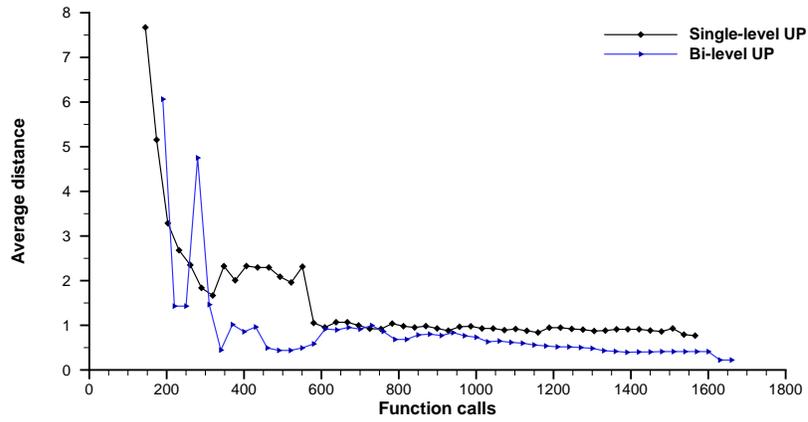
109
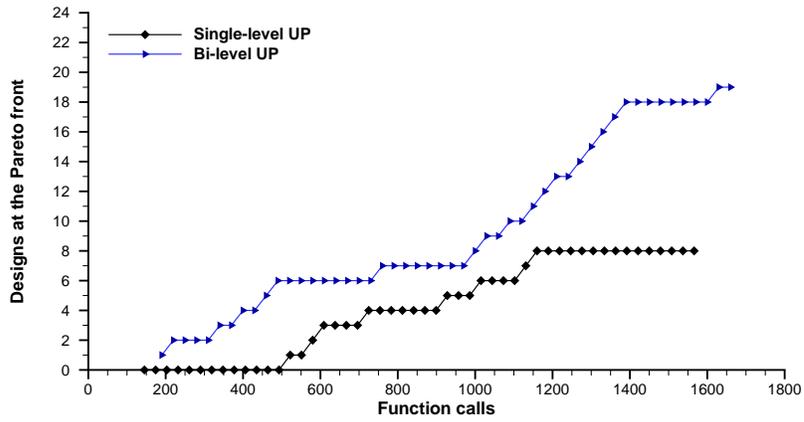
(a) Uncertainty level: 100%
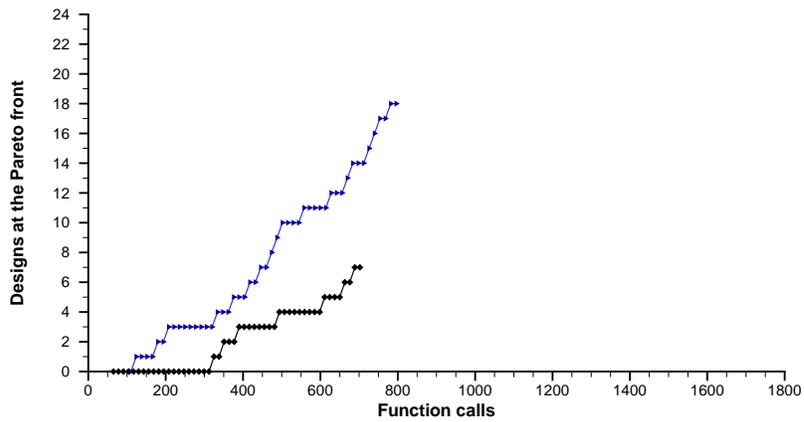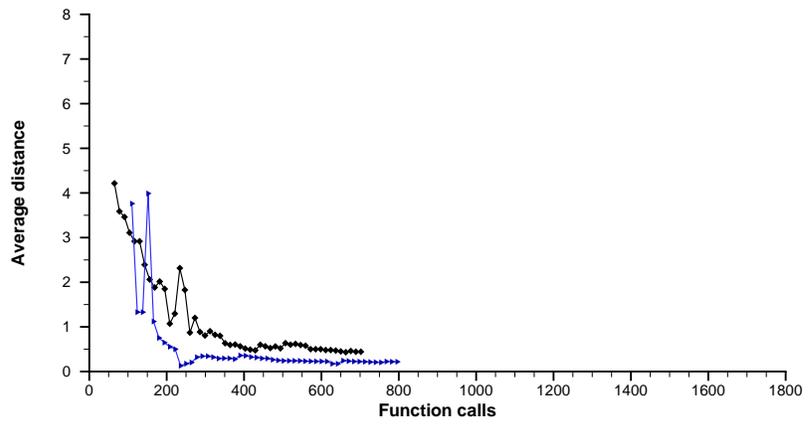

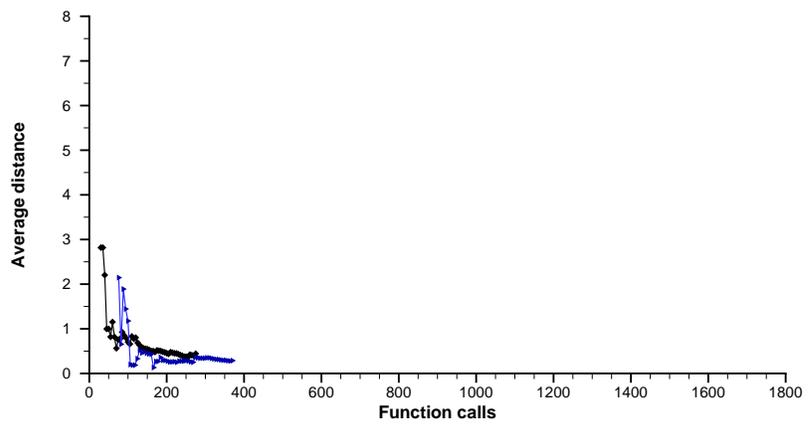(b) Uncertainty level: 30%
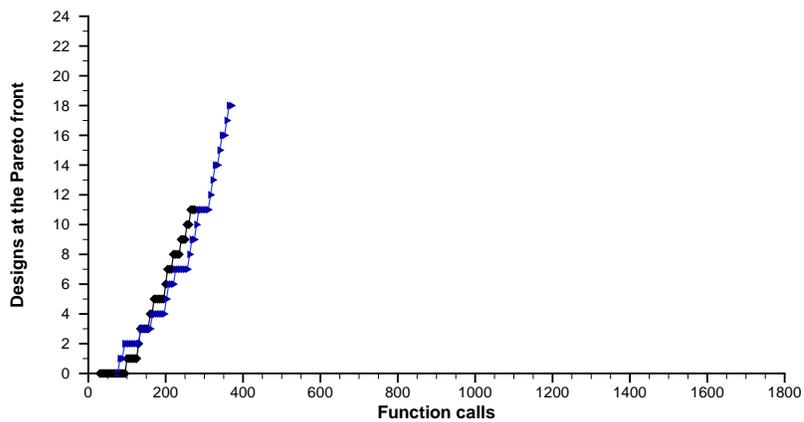
(c) Uncertainty level: 8%

Figure 19: Non-dominated designs at the Pareto front for different uncertainty levels

(a) Uncertainty level: 100%

(b) Uncertainty level: 30%

(c) Uncertainty level: 8%

Figure 20: Average distance to the Pareto front for different uncertainty levels

distance is shown in figure 20 and it is observed that as the level of uncertainty decreases, the average distance of these two strategy approach each other. For the levels of uncertainty of 100% and 30% shown in figures 20(a) and 20(b), the distance of the bi-level strategy is noticeable shorter than that of the single level. However, for the smallest level of uncertainty shown in figure 20(c), both strategies have comparable average distance.

In summary, it can be concluded that the trend for levels of uncertainty as well as for non-linearity is similar. As a result, the benefit of the bi-level strategy decreases as the non-linearity of the cost function $\mathcal{J}$ and the levels of uncertainty in the stochastic variables decreases.

It must be point out that this behavior is not expected to be continuous. First, for the study of the effect of non-linearity, it is difficult to find a mean to vary non-linearity continuously. Even if this could be done, the performance of the bi-level strategy would not be gradual. This is because the performance mostly depends on the relatively cost between of the high and low fidelity UP. While the cost of the low fidelity UP depends on the dimensionality of the stochastic space for the LE method, the cost of the high fidelity UP, which is the gPC-SG, depends on the level of the sparse grid integration (l) which by definition discrete. Consequently, changing from one level to another involves a discrete change on the computational cost.

A similar explanation applies to the levels of uncertainty study. Although the uncertainty level can be vary continuously, the performance of the bi-level strategy is not expected to change gradually. Again, this is because of the sparse grid level which is discrete. As a result, there must be certain range in uncertain that may require a determine sparse grid level, while other ranges may a require a different level.

CHAPTER VI

ROBUST AERODYNAMIC DESIGN

In this chapter, the polynomial chaos - sparse grid (gPC-SG) based UP strategy detailed in Chapter IV and the two strategies for robust optimization described in Chapter V are applied to aerodynamic robust design. The main purpose is to achieve minimum sensitivity of the optimal aerodynamic performance with respect to uncertain operating conditions.

The strategies are successfully tested in a low Reynolds number airfoil robust optimization. It is found that results found by the gPC-SG strategy are in good agreement with that of more expensive methods such as the quasi-Monte Carlo method. However, The gPC-SG accomplish this at smaller cost. Furthermore, it is verified that the two robust optimization strategies are able to approximate well the actual Pareto. Both approaches are able to place designs at the actual front as well as reduce the average distance of the non-dominated set to the Pareto front.

Finally, the results of the robust design of a transonic wing are presented. The main purpose of this last test case is to show the applicability of the methods to practical design applications. Since this last test case involves more expensive analysis, comparisons with the actual solution such as that given by a quasi-Monte Carlo method and a multi-objective genetic algorithm are not given here. Nevertheless, this does not contradict the studies of the research hypothesis and predictions performed earlier.

6.1 Formulation of the robust optimization problem

The robust optimization problem is formulated as multi-objective optimization problem

$$\text{Minimize} \quad \boldsymbol{F} \;=\; [\, f_1\,,\, f_2\,]^{\mathsf{T}} \tag{119}$$

$$\text{Subject to}$$

$$\boldsymbol{X}_l \leq \;\boldsymbol{X}\; \leq \boldsymbol{X}_u$$

where $\boldsymbol{F}$ is the vector of objectives, and $\boldsymbol{X}$ is the vector of design variables whose upper and lower bounds are $\boldsymbol{X}_l$, and $\boldsymbol{X}_u$, respectively. In robust optimization, the main purpose is the maximization of some average performance and simultaneously the minimization of the performance variation. As result, the vector of objectives is defined as

$$\boldsymbol{F} = \begin{bmatrix} -\mu_{\mathcal{J}} \\[4pt] \sigma_{\mathcal{J}} \end{bmatrix},$$

where $\mathcal{J}$ is a functional expressing some cost function. These objective are generally defined as the first statistical moments of the cost function

$$\mu_{\mathcal{J}} \;=\; \int_{\Gamma} \mathcal{J}(\boldsymbol{X},\boldsymbol{\xi})\, \rho(\boldsymbol{\xi})\, d\boldsymbol{\xi},$$

$$\sigma_{\mathcal{J}}^2 \;=\; \int_{\Gamma} (\, \mathcal{J}(\boldsymbol{X},\boldsymbol{\xi}) - \mu_{\mathcal{J}})^2\, \rho(\boldsymbol{\xi})\, d\boldsymbol{\xi}$$

where $\boldsymbol{\xi} \in \Gamma$ represents a vector containing the uncertain parameters that are considered mutually independent, and $\rho(\boldsymbol{\xi})$ is the joint probability density function of the uncertain parameters.

6.2 Airfoil case

As a first test case, the robust optimization of a low Reynolds number airfoil is considered. The cost function is assumed to be lift over drag coefficient, i.e. $\mathcal{J} = L/D$. An AG-24 sailplane airfoil is used as a baseline airfoil for the optimization process.

Geometrical airfoil parameters such as thickness and camber locations, and others are considered as design variables. These variables are contained in the vector of design variables, $\boldsymbol{X}$. In order to create new airfoils, these parameters are adjusted in the geometry design module of XFOIL. Operating conditions such as Reynolds number and the lift coefficient c_l are considered uncertain, and they are contained in the vector of stochastic variables, $\boldsymbol{\xi}$. These two vectors are defined as follow

$$\boldsymbol{X} = \begin{bmatrix} max.\ camber\ location \\ max.\ thickness\ location \end{bmatrix}, \quad \boldsymbol{\xi} = \begin{bmatrix} c_l \\ Re \end{bmatrix}.$$

The lower and upper bound vectors of the design variables, expressed as percentage of the airfoil chord, are $\boldsymbol{X_l} = [\,35\,,\,20\,]^\intercal$ and $\boldsymbol{X_u} = [\,70\,,\,33\,]^\intercal$. The stochastic variables have uniform distributions with variations of $\pm\,0.08$, and $\pm\,0.25 \times 10^5$ over the mean values of 0.6 and 2.5×10^5, respectively.

6.2.1 Deterministic code

The deterministic solver used in this study is XFOIL [28]. It is an interactive code for the analysis and design of low Reynolds number airfoils. It is a two-dimensional potential flow solver with boundary layer interaction, having the capability of computing both inviscid and coupled viscous-inviscid boundary layer flows. It is based on a boundary layer integral formulation that employs a two-equation lagged dissipation integral method for both laminar and turbulent flows. The laminar viscous layer formulation involves a transition prediction based on the spatial amplification theory in which a linear model that accounts for the growth of the amplitude n of the most amplified Tollmien-Schlichting wave is employed. The wake is modeled by using the same two-equation formulation of the boundary layers. The inviscid flowfield, however, is calculated by using a linear-vorticity panel method. The drag is obtained by using the wake momentum thickness of the downstream region. The velocity at any point of the airfoil surface and its wake is corrected by using the Karman-Tsien

compressibility factor. This is in turn incorporated into the viscous formulation yielding a nonlinear elliptic system which is further solved by a full-newton method. A more detailed description of XFOIL and its mathematical formulation is presented in appendix A.

6.2.2   Results

In this section, results for the robust optimization of low Reynolds number airfoil are presented. The results are divided in two parts. In the first part, the main purpose is to test the accuracy of the proposed generalized polynomial chaos-sparse grid (gPC-SG) based UP strategy for a Robust design problem without having any influence of the Pareto front approximation method. In order to accomplish this, the Pareto front approximation is carried out by employing a multi-objective genetic algorithm (MO-GA), and the optimization objectives $\boldsymbol{F} = [\,-\mu_{\mathcal{J}},\, \sigma_{\mathcal{J}}\,]^{\mathsf{T}}$ are calculated by four different uncertainty propagation methods: a quasi-Monte Carlo (quasi-MC) method, a local expansion-based method (LE), the univariate dimension-reduction method (UDR), and the proposed gPC-SG strategy.

In the second part, the single-level and bi-level robust design strategies are applied to the same robust design problem. In order to quantify their effectiveness the two metrics: (1) number of designs at the Pareto front and (2) the average distance of the non-dominated set to the actual front are used. The actual Pareto front is assumed to be that one found by the quasi-MC and the MO-GA method.

6.2.2.1   MO-GA based robust optimization

The accuracy of the gPC-SG strategy is studied here. In order to isolate the influence of the robust optimization method, the Pareto front is approximated by using a multi-objective genetic algorithm (MO-GA). The set up of the multi-objective genetic algorithm is 200 generations and a population of 500 for all cases. In addition, an initial population of 250 is considered. Among all the methods considered, methods

116

such as the local expansion (LE) based method and univariate dimension-reduction method (UDR) can be the most inaccurate; however, they have the lowest computational cost. For instance, the cost of the LE method depends only on the cost of calculating the derivatives with the uncertain parameters. These derivatives can be calculated by one-side finite differences which for this two-dimensional case leads to 3 function calls per design. The univariate integration method used for UDR is a three point Gauss-Legendre quadrature which leads to a cost of 5 function calls per design.

The most accurate and at the same time the most expensive method considered is the quasi-Monte Carlo method. Due to its theoretical better convergence for few number of uncertain parameters, the quasi-MC is preferred instead of the crude Monte Carlo method. The number of samples (function calls) considered is 10^3. The proposed gPC-SG strategy is set to a chaos order $p = 6$, and sparse grid integration level of $l = 3$. These values give a computational cost of 29 function calls per design. The computational cost per design of propagating uncertainties is summarized in the table 10 for the four considered methods.

**Table 10:** Computational cost of propagating uncertainties

UP method	Scaling cost	Function calls
LE (FOFM and FOSM)	$d+1$	3
UDR	$2d+1$	5
gPC-SG	–	29
quasi-MC	–	10^3

The corresponding Pareto fronts are shown in figure 21(a). For comparison purposes, it is assumed that the Pareto front found by the quasi-MC method is the actual Pareto front. It is noted that among all the UP methods the front found by the LE method is located the farthest from the actual Pareto front. This method

117

tends to overpredict the mean performance for any value of the standard deviation. Moreover, most of the variation in the mean performance occurs in a very small region for values $\mu_{L/D} \approx 81$. In that region, the mean performance becomes extremely sensitive to variations in the operating conditions. In contrast, the mean performance is pretty insensitive for mean performance values $\mu_{L/D} \leq 81$. By comparing to the actual Pareto front, it is clear that for this particular problem the local validity of the Taylor expansion prevents this approach from placing non-dominated designs that approximate more accurately the actual front.

The Pareto front found by the UDR method is the second to be located the farthest from the actual Front. Although there is a small region in which it is closer to the actual front, for mean performance values in the range between $76.5 \leq \mu_{L/D} \leq 78$, anywhere else the UDR misses the actual front. Moreover, in those regions the UDR front lays closer to the LE front. The UDR assumption of approximating a multivariate function by univariate ones works only in some regions of the design space in which the simplicity of the cost function, L/D, with the stochastic parameters is such that this assumption holds, for instance the region in which the non-dominated design closer to actual front. However, in other locations in the design space this assumption is not longer valid.

Conversely, the Pareto front calculated by the gPC-SG strategy is located the closest to the actual Pareto front. Indeed, the gPC-SG front seems to overlay the Pareto front found by the quasi-MC. Therefore, there is a good agreement between these two methods. Similar to the quasi-MC, the gPC-SG strategy leads to more modest performance, having a more gradual variation of the mean performance with the standard deviation. This gradual variation is actually an expected trend since the objectives are outcomes from statistical moments (average values) that are calculated in the space of the uncertain operating parameters. This is in contrast to the LE and UDR method in which the statistics are defined locally or by univariate representation
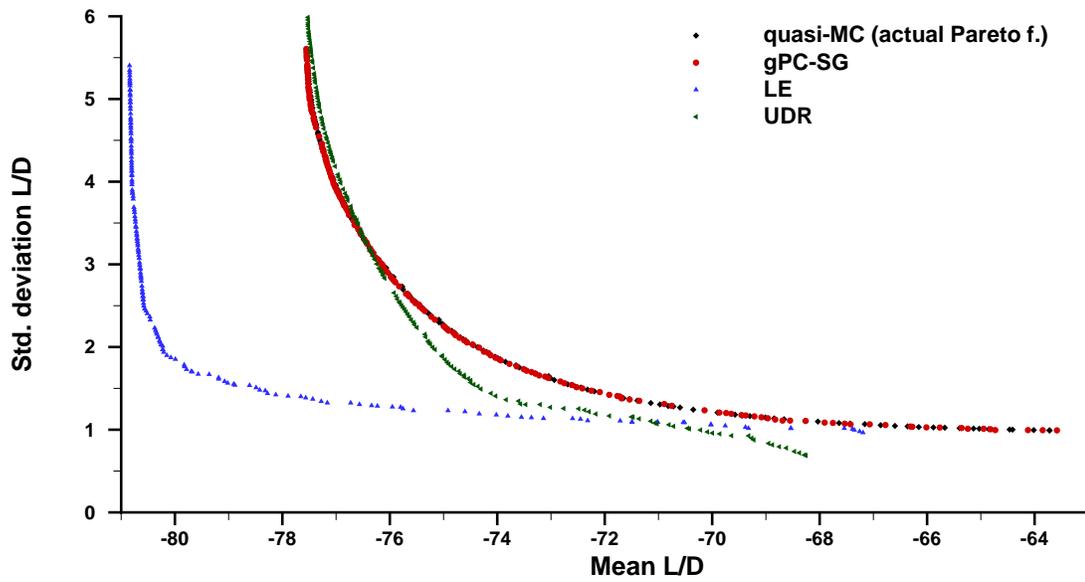
(a) Pareto front
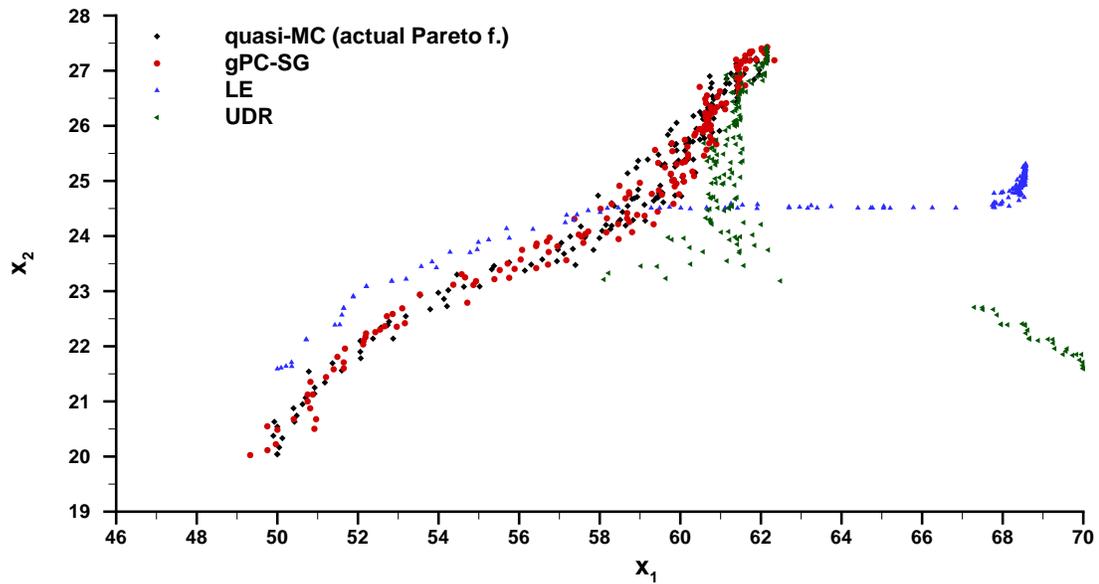
(b) Non-dominated designs

Figure 21: MO-GA based robust design

of the cost function.

The non-dominated designs for the uncertainty propagation methods are shown in figure 21(b). The non-dominated designs for the LE method tend to be clustered in very small regions of the design space, including the right boundary of the maximum camber location. Moreover, their locations differ significantly front those of the actual non-dominated designs (quasi-MC). The UDR non-dominated design also differ from the actual ones except for a small region for high values of the maximum thickness. In contrast, the quasi-MC and the gPC-SG methods predict designs that are located in the same region. Also these designs are more spread out over the design space.

Local expansion-based (LE) methods such as the FOFM-FOSM method allow cheap calculation of robust objectives and for this reason they have been extensively used in robust design optimization. However, the presented airfoil robust design problem shows that the underlying assumptions of these methods make them prone to be inaccurate for some types of problems. Therefore, more general methods for uncertainty propagation are needed. The proposed gPC-SG strategy was shown to give results that are in good agreement with highly cost UP methods such as the quasi-Monte Carlo method, whereas at a considerable lower computational cost.

6.2.2.2   *Single-level and Bi-level gPC-SG based robust optimization*

The main purpose of MO-GA robust optimization was to shown the efficiency of the gPC-SG strategy for propagating uncertainties for a robust design problem of an engineering application. Although very effective, the use of multi-objective genetic algorithms is usually expensive due to long run times resulting from high number of designs and generations needed. The computational cost is even increased if the analysis function are expensive to evaluate. Moreover, if the calculation of the optimization objectives requires several samples as in the case of design under uncertainty, the cost can be even higher and it may render these methods unusable. Therefore, in

addition to efficient uncertainty propagation methods, robust design requires efficient formulations to sample the design space.

The single-level and bi-level robust design strategies proposed in the previous chapter are applied to the low Reynold airfoil case as a mean to tackle the high computational cost in which robust design may incur. The single-level strategy only uses a high fidelity uncertainty propagation method that is the gPC-SG. The bi-level strategy, however, uses two different levels of accuracy of the UP method. It also uses the gPC-SG as the high fidelity UP, but in addition considers the information of a lower fidelity UP which, in general, drives the efficiency.

Unlike the analytical test cases in the previous chapter in which the LE method was used as the low fidelity UP, the airfoil case considers the gPC-SG method as the low UP, but at a sparse grid integration level of $l = 1$ which the lowest integration level. The main idea behind this is not only to attempt different alternatives for the low UP, but also avoiding the computational cost (function calls) of the low UP while performing adaptive sampling. This is always possible with the gPC-SG because of the nested nature of sparse grid node distribution. This means that an integration level $l = n + 1$ uses all the points of lower integration levels, $l = n, n - 1, \ldots, 1$. Therefore, the function calls of the low UP can be used by the high UP. There is, however, an initial higher cost of the low UP. An integration level $l = 1$ requires $2d + 1$ points for "d" uncertain parameters. This cost is higher than the cost of the LE if one-sided finite difference is considered for the calculation of the derivatives. However, the cost is the same of the derivatives if a central difference is considered. As a result, it can be said that the gPC-SG with $l = 1$ as the low UP has similar cost of the LE method if central finite difference for the derivatives calculation is used.

The search of the Pareto fronts by employing the single-level and bi-level is shown in figure 22, after 5, 10, and 20 adaptive samples. As a reference the Pareto front found by using a quasi-MC method and the MO-GA from the previous section is also

shown. Again, this front is considered as the actual Pareto front. The single-level strategy is initialized with 4 points in the design space, whereas the bi-level strategy in addition is initialized with 24 points for the low fidelity UP. The high fidelity initial points are shown by green diamonds. The kriging and co-kriging models of the single-level and bi-level strategies are tuned after every new sample update by maximizing the likelihood function with a genetic algorithm.

It is easily noted that both strategies are able to place designs closer to the Pareto front as the number of adaptive samples increases. In the case of the single-level approach, initially it will try to explore the design space by augmenting the current non-dominated set; however, the location of these designs are not yet close to the actual front, see figure 22(a). As the adaptive sampling process progresses, few non-dominated designs can be seen at the actual front, for instance at 20 samples (figure 22(e)) there are three samples. Moreover the non-dominated set, symbolized by the blue circles, is located in the near region of the actual front.

For the bi-level strategy, after exploring regions that are no close to the actual Pareto front, one design is placed near the actual front at 5 adaptive samples as seen in figure 22(b). As the adaptive process continues more regions are explored; however, by 10 adaptive samples not only two designs are exactly located at the actual front, but also the non-dominated design is very close to the actual front (figure 22(d)). In general, the bi-level strategy has a higher rate of placing non-dominated design near the Pareto front than the single-level. This is confirmed after 50 adaptive samples as shown in figure 23. It is noticed that the bi-level strategy explores less areas of no interest and thus is able to place samples in the nearby regions of the actual Pareto front.
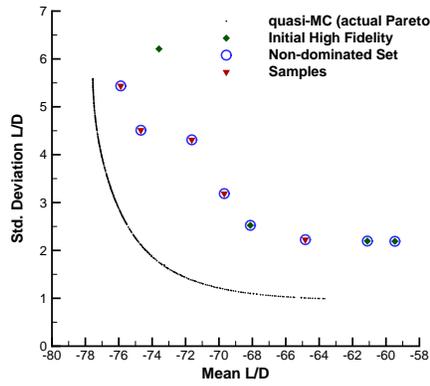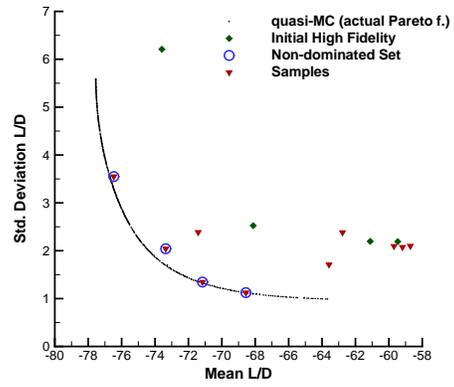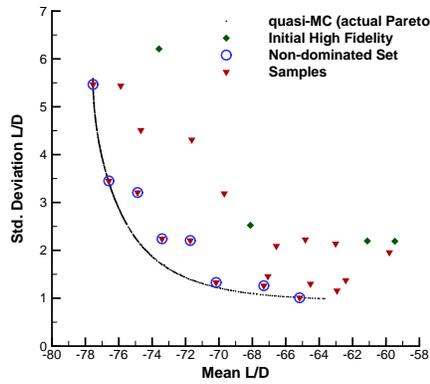
(a) Single-level, 5 samples
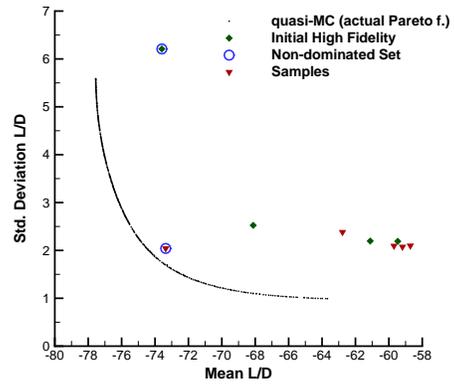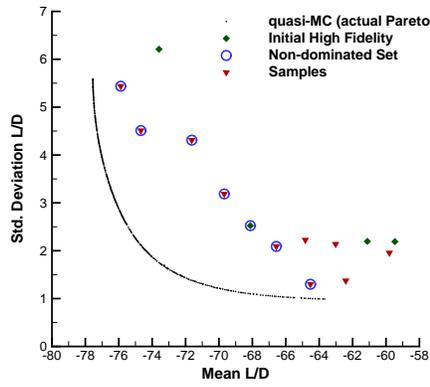
(b) Bi-level, 5 samples

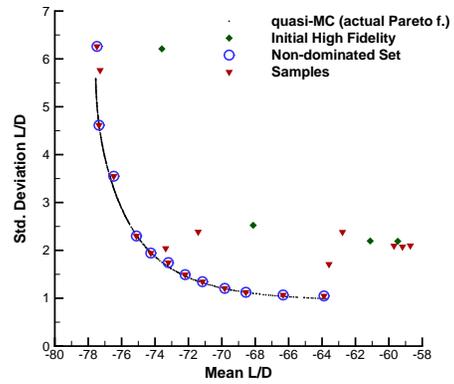(c) Single-level, 10 samples

(d) Bi-level,10 samples

(e) Single-level, 20 samples

(f) Bi-level, 20 samples

Figure 22: Search of Pareto front by the single-level and bi-level robust design strategies after 5, 10, and 20 adaptive samples
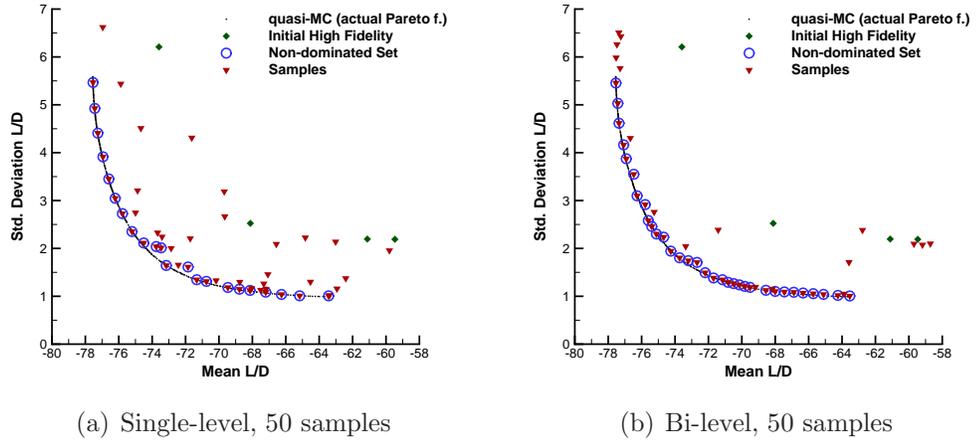
123

(a) Single-level, 50 samples (b) Bi-level, 50 samples

Figure 23: Search of Pareto front by the single-level and bi-level robust design strategies after 50 adaptive samples

6.2.2.3 Computational cost comparison

It was shown that as a function of adaptive samples the bi-level strategy performs better than the single-level. An explanation for this is that initially the bi-level has more information since it has not only data of the high fidelity UP, but also data of the low fidelity UP. Therefore, comparisons should be made as a function of the computational cost (function calls) rather than adaptive samples. In order to assess this, the metrics:

i. Number of non-dominated designs lying at the actual Pareto front,

ii. Average distance of the non-dominated set to the actual Pareto front,

defined in the previous chapter are employed. A non-dominated design is considered to be located on the actual Pareto front if its distance to the actual front is lower than a certain threshold. For this problem, the threshold is set to $\delta \leq 0.1$.

The number of non-dominated designs at the actual Pareto front as a function of the computational cost (number of function calls) is shown in figure 24(a). It must be noted that the bi-level strategy has a higher initial cost the single level since it requires a larger sample of the low fidelity propagator in addition to the sample of

124
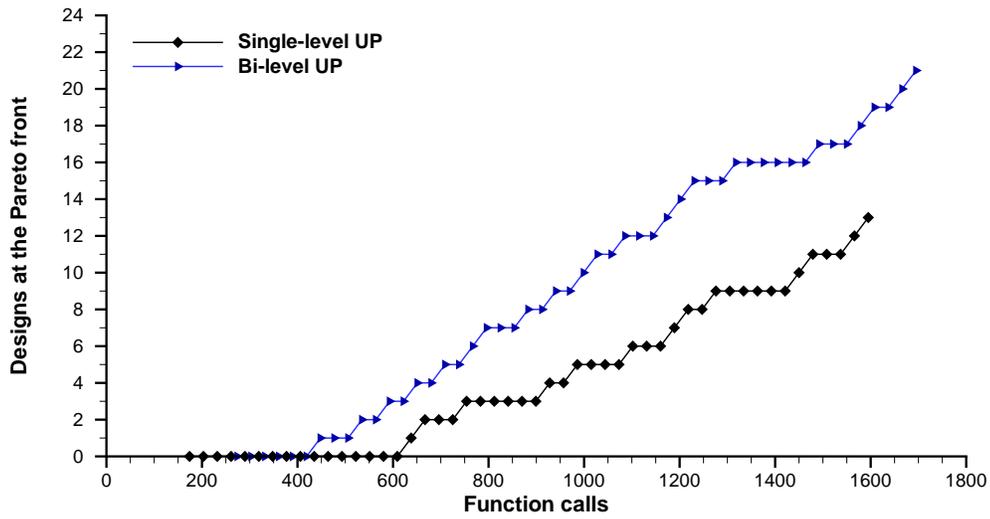
(a)
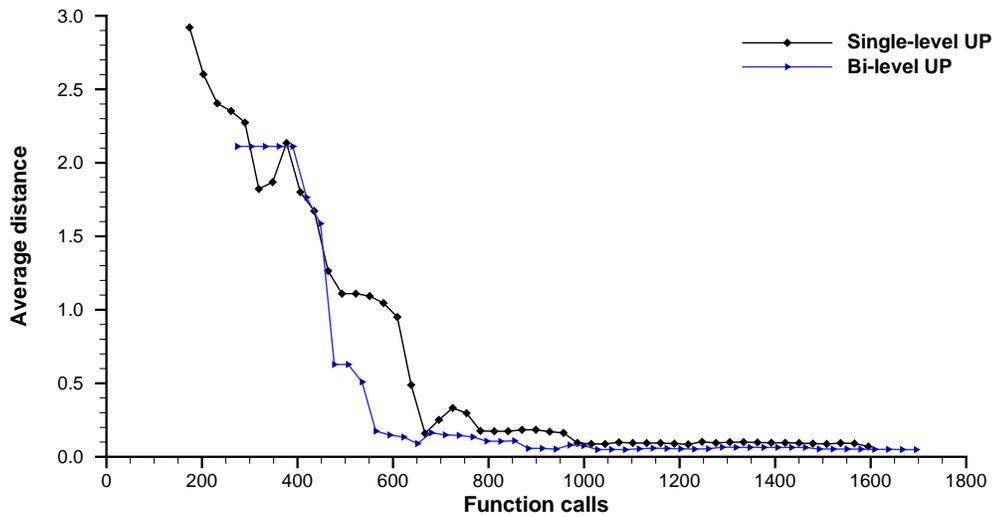
(b)

Figure 24: Designs at the Pareto front (Fig.(a)) & Average distance (Fig.(b))

the high fidelity propagator. Nevertheless, from figure 24(a), it can be seen that for any determine budget (number of function calls) the bi-level strategy places more non-dominated designs in the proximity of the actual Pareto front.

The second mean to measure the effectiveness is the average distance of the non-dominated set to the actual Pareto front. The average distance as a function of function calls is shown in figure 24(b). For both strategies, the average distance tends to decrease with function calls. However, it is noted that, in general, the bi-level strategy gives a shorter average distance to the actual Pareto front. For large computational budgets, the average distance of both strategies is small; however, for the bi-level the distance is slightly shorter.

6.3   Transonic wing case

In this section, the robust design of a transonic wing is addressed. During aircraft operation, conditions such as Mach number and cargo weight are subject to variability and random fluctuations. The first one is likely to change due to weather conditions or variation in the cruise speed, while the latter can change due to different number of passengers, cargo weight, and variation of the fuel weight. Therefore, there is a need to incorporate the effects of operating conditions variability at a design stage.

The present transonic wing design case is developed for early design stages; therefore, low order analyses are adopted. Nevertheless, there is no limitation to apply the developed methods to later design stages, including detail design, although high fidelity analysis such as computational fluid dynamics (CFD) will be needed.

At transonic speeds, the effects of compressibility leads to more complicated features in the flow field such as shocks. Therefore, analysis than can accurately capture such as features may be needed. One alternative is the use of high fidelity analysis such as computational fluid dynamics (CFD). However, this analysis is mostly reserved for later stages of design after large-scales variables such as aspect ratio and area have been selected. In this work, an alternate analysis that combines a vortex lattice method and a compressible solver for airfoils is adopted. Athena vortex lattice (AVL) [32] is used for 3-dimensional wing flowfield. MSES [30] is used for

compressible profile drag

The vortex lattice method tend to be most accurate for high aspect ratio wings, while the compressible effects on aerodynamic quantities can be captured accurately for low transonic flow with the Euler equations in MSES [102]. Therefore, the focus of this test case is high aspect ratio wing at low transonic speeds. Despite of the simplicity of the analysis, it will be shown that predictions of aerodynamic quantities can be reasonably well captured for early sizing of a robust design wing

6.3.1   Deterministic codes

The aerodynamic analysis is performed with Athena Vortex Lattice (AVL) [32]. AVL is an extended vortex-lattice model program for aerodynamic analysis, trim calculations, dynamic stability analysis, and aircraft configuration development. The viscous effects in the boundary layer are accounted by including drag profile information. This profile drag is then added to the induced drag computed by the vortex lattice code. Although this assumes independence between the profile drag and induce drag, it is a reasonable approximation for high aspect ratio wings.

The airfoil drag information is obtained from MSES [30]. This is a two-dimensional analysis and design code for multi-element airfoils. It employs a steady state Euler formulation on a streamline grid for solving the inviscid outer flow. The boundary layer, however, is simulated by an integral boundary layer formulation based on two-equation integral and the coupling with the inviscid flow is attained by using the displacement thickness.

Although originally the AVL code assumes a quadratic fit for the profile drag, in this study the viscous drag is explicitly given to AVL from the MSES codes, so no fit is assumed.

6.3.2 Validations

Previous to the use AVL and MSES for transonic wing calculations, validations are needed to demonstrate their applicability to this problem. First validations of MSES to capture aerodynamic quantities of airfoil sections at transonic speed are shown. This is done by comparing with experimental data. Then, AVL and MSES are validated against CFD data for a transonic wing.

6.3.2.1 Transonic airfoils

In order to assess the accuracy of MSES for transonic profiles, validations are performed by comparing with experimental data by Cook *et al.* [23] for the RAE 2822 airfoil. Since the experimental data is reported in term of the normal coefficient, the following implicit equation :

$$c_n = c_l \cos \alpha + c_d \sin \alpha, \tag{120}$$

needs to be solved for the angle of attack, α. MSES is used to determine the value of lift coefficient, c_l, drag coefficient, c_d and angle of attack, α, that matches the given c_n. Equation 120 is solved iteratively until a threshold of 10^{-6} is attained. Once these values are determined, the drag coefficients predictions given by MSES are compared to those from the experiments.

The values obtained from MSES as well as the experimental data are shown in table 11 for the thirteen cases reported in the experiment. The highest percent error found in the drag prediction is 16 % for the case 3. However, most of the validated cases are below 9%. Most importantly, for the highest Mach number cases, the disagreement in the drag prediction is not larger than 6%. This is particular important since this study focuses in Mach numbers in that range.

The predicted pressure distribution for the highest Mach number (case 10) is shown is figure 25. This calculation, however, was carried out by matching the pressure distribution. This procedure given by Huff, Wu and Sankar [56] compensates

Table 11: RAE 2822 airfoil drag validations

| | Experiment | | | | | MSES | |
Case	M_∞	Re $(\times 10^{-6})$	Transition x/c	c_n	c_d	c_d	Drag error (%)
1	0.676	5.7	0.11	0.566	0.0085	0.00830400	2.306
2	0.676	5.7	0.11	- 0.121	0.0079	0.00798500	1.076
3	0.600	6.3	0.03	0.522	0.0101	0.00843400	16.495
6	0.725	6.5	0.03	0.743	0.0127	0.01156000	8.976
7	0.725	6.5	0.03	0.658	0.0107	0.00978900	8.514
8	0.728	6.5	0.03	0.802	0.0175	0.01512600	13.566
9	0.730	6.5	0.03	0.803	0.0168	0.01598800	4.833
10	0.750	6.2	0.03	0.743	0.0242	0.02284200	5.611
12	0.730	2.7	0.03	0.721	0.0133	0.01385700	3.798
13A	0.740	2.7	0.03	0.733	0.0188	0.01841500	2.048

the effect of the wind tunnel interference which is not easily determined from the experimental data. A "matched" pressure distribution is the best agreement between the experimental data and the analysis predictions. This is achieved by adjusting the Mach number and angle of attack. In the present study, however, the Mach number is fixed to the experimental value and the adjustments are made only by varying the angle of attack. This results in a lift coefficient and angle of attack of 0.74274 and 2.6443^o, respectively. Although the pressure distribution obtained by MSES does not match exactly the experimental data, it is considered to be in good agreement with the experiment. Moreover, this prediction seems to be comparable with a previous validation using a two-dimensional, Reynolds-averaged, compressible Navier Stokes solver [56].

6.3.2.2 Transonic wing

The accuracy of AVL / MSES for calculating the aerodynamic quantities of transonic wings is assessed here. The results given by AVL / MSES are compared to those
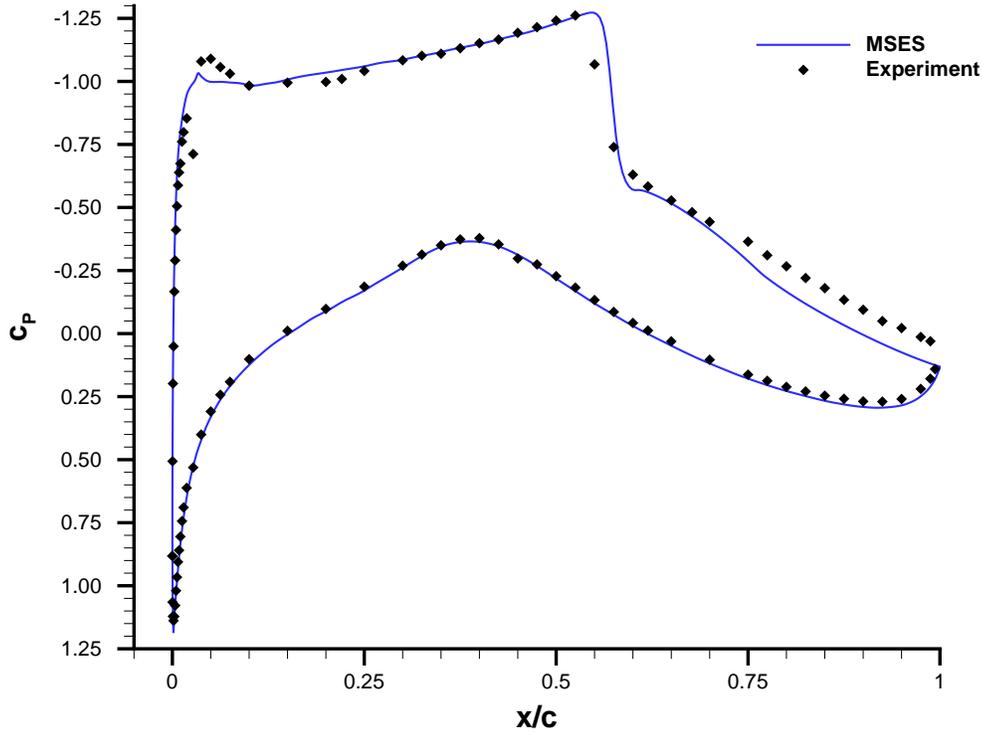
Figure 25: RAE 2822 pressure distribution comparison, $M_\infty = 0.75$, $Re = 6.2 \times 10^6$

given by OVERFLOW, a NASA CFD code. These comparisons are performed for a transonic wing of bussines jet whose details are given in the next section.

The CFD data [68] comprises three cases at different Mach numbers which conditions are shown in table 12. These values of Mach number are representatives of the range of Mach number that are used in the robust optimization problem given in the next section.

The OVERLOW code solves the Navier-Stokes equations in overset structured grids. It was used with a Roe upwind scheme, a Beam-warming block diagonal scheme, and one equation Spalart-Allmaras turbulence model. For all cases, the boundary layer mesh size was set by considering a flat plate with $y^+ = 1$ estimate based on the wing average chord Reynolds number, and the grid consist of 16 millions cells. Every case required 600 CPU hours in a linux cluster.

Table 12: Validation cases for transonic wing

| Case	Altitude	M_∞	Re (*)	C_L
1	35000	0.710	10600000	0.44035
2	35000	0.720	10769789	0.42820
3	35000	0.728	10900000	0.41884
4	35000	0.740	11068946	0.40542
5	35000	0.750	11200000	0.39463
5	35000	0.758	11300000	0.38634
6	35000	0.770	11517691	0.37442

* Based on the wing average chord

The lift to drag ratio, L/D, obtained by AVL / MSES, and OVERFLOW is shown in figure 26(a). It is noticed that AVL / MSES overpredicts this ratio for all the cases. Nevertheless, the pattern of the lift to drag ratio with Mach number is well captured by AVL / MSES. The quantification of the disagreement of this ratio between these analysis codes, as percent error, is shown in figure 26(b) along with the percent error of the drag coefficient C_D. For both aerodynamic quantities, the error is lower than 4% for Mach numbers up to 0.74; however, the percent error can be as high as 9% for a Mach number of 0.77. More details of the calculated aerodynamic quantities and the percent errors are shown in tables 13, 14, and 15, respectively.

For any real design application the result of AVL / MSES may not be reasonable. However, in spite of the error, AVL / MSES are able to capture general trends of the aerodynamic quantities of interest. Most importantly, in this work this type of analysis is preferred due to computational feasibility. This is because the computational cost of more sophisticated analysis such as CFD demands more resources, and thus they are too costly.
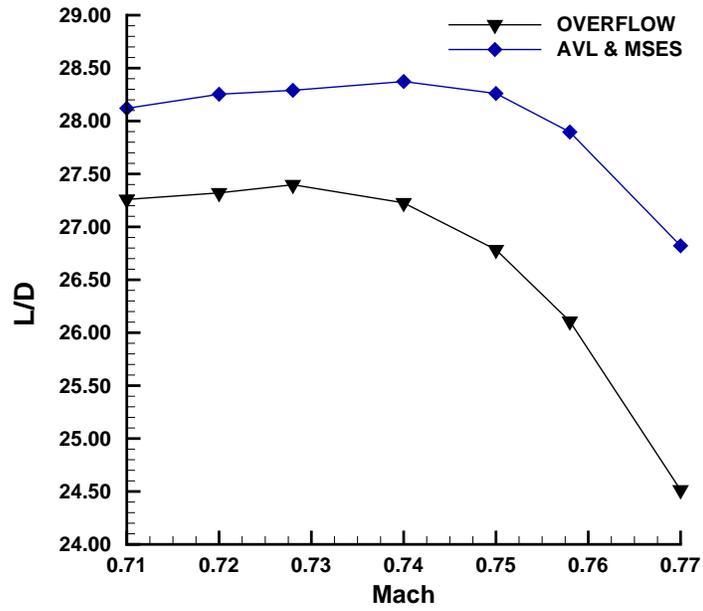
(a)
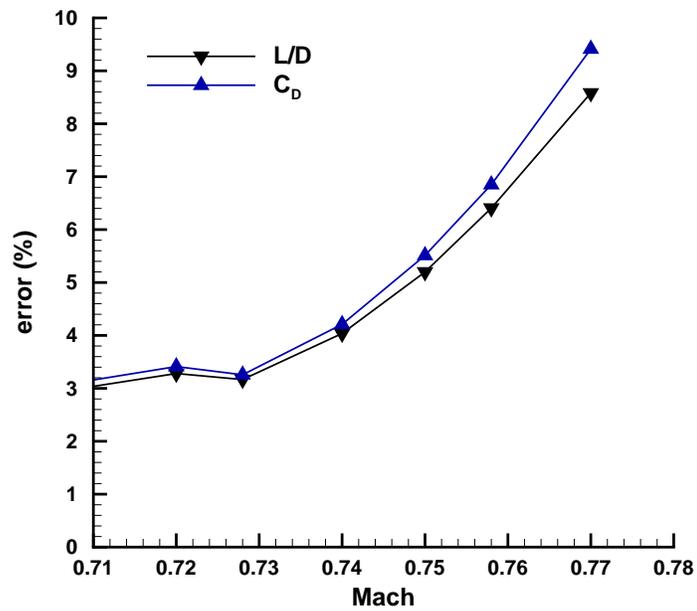
(b)

Figure 26: Wing aerodynamic quantities validation

Table 13: AVL/MSES calculated aerodynamic quantities

Case	M_∞	C_L	C_D	L/D
1	0.710	0.440343	0.01565944	28.119996
2	0.720	0.428202	0.01515596	28.253095
3	0.728	0.418862	0.01480589	28.290247
4	0.740	0.405421	0.01428888	28.373222
5	0.750	0.394631	0.01396417	28.260259
6	0.758	0.386360	0.01384986	27.896356
7	0.770	0.374422	0.01395972	26.821442

Table 14: OVERFLOW calculated aerodynamic quantities

Case	M_∞	C_L	C_D	L/D
1	0.710	0.440350	0.01615	27.259
2	0.720	0.428200	0.01567	27.321
3	0.728	0.418840	0.01529	27.398
4	0.740	0.405420	0.01489	27.227
5	0.750	0.394630	0.01473	26.784
6	0.758	0.386340	0.01480	26.108
7	0.770	0.374420	0.01527	24.514

Table 15: Percent error of calculated aerodynamic quantities

		Percent error (%)		
Case	M_∞	C_L	C_D	L/D
1	0.710	0.001487	3.037510	3.158576
2	0.720	0.000655	3.280403	3.411644
3	0.728	0.005326	3.166182	3.256614
4	0.740	0.000393	4.037067	4.209874
5	0.750	0.000258	5.199127	5.511719
6	0.758	0.005326	6.405647	6.849839
7	0.770	0.000016	8.580718	9.412752

6.3.3 Design implementation

The aircraft configuration used in this test is based on a medium-range business jet aircraft, the *Learjet 60*, manufactured by Bombardier. The aircraft has a long-range cruise Mach number of 0.74 at altitude of 35,000 ft.

Table 16: Specification for the business jet

Performance		
Long-range cruise Mach number	0.74	
Take-off gross weight	23500	lb
Operating weight	14000	lb
Maximum payload weight	2109	lb
Maximum fuel weight	7910	lb
Wing geometry		
Reference area	264.50	ft^2
Wing span	43.79	ft
Sweep angle*	16	deg
Taper ratio*	0.397	

* : based on drawings

In this test case, only the cruise condition is considered for the robust optimization problem. The geometry of the business jet has been simplified for the purposes of solving the robust design problem. Moreover, due to the lack of technical information, some geometry parameters has been approximated from drawings. Therefore, this case only represents a proof-of-concept problem to demonstrate the usefulness of the presented methods, and is by no means intended to represent a realistic full-configuration case. Information of this aircraft is shown in table 16.

The optimization problem to ultimately be solved is the robust design problem

described in section 6.1, i.e.,

$$\text{Minimize} \quad \boldsymbol{F} \quad = \quad [\,-\mu_{L/D}\,,\,\sigma_{L/D}\,]^T \tag{121}$$

Subject to

$$\boldsymbol{X}_l \leq \quad \boldsymbol{X} \quad \leq \boldsymbol{X}_u,$$

where $\boldsymbol{F}$ is the objective vector which is composed by the mean and the standard deviation of the wing lift to drag coefficient, $\boldsymbol{X}$ is the design variable vector whose element are wing planform variables :

$$\boldsymbol{X} \quad = \quad \begin{bmatrix} s \\ ar \\ \lambda \\ tr \end{bmatrix} \quad = \quad \begin{bmatrix} wing\ area \\ aspect\ ratio \\ sweep\ angle \\ taper\ ratio \end{bmatrix}.$$

The lower and upper limits of the design variables, $\boldsymbol{X}_l$ and $\boldsymbol{X}_u$, are shown in table 17

Table 17: Wing design variables and ranges

Design variable	Units	Lower limit $\boldsymbol{X}_l$	Upper limit $\boldsymbol{X}_u$
Wing area	ft^2	220	350
Aspect ratio		7	9
Sweep angle	deg	10	20
Taper ratio		0.3	0.5

In addition, a constrain in the wing volume is imposed

$$198.5\,\text{ft}^3 \leq V_w \leq 344.3\,\text{ft}^3$$

The stochastic variables are uncertain operating conditions:

$$\boldsymbol{\xi} = \begin{bmatrix} M_\infty \\ w \end{bmatrix}. = \begin{bmatrix} \textit{Mach number} \\ \textit{weight} \end{bmatrix}.$$

The description of the stochastic variables are shown in table 18.

Table 18: Uncertain parameters

Uncertain parameter	Units	Distribution	Support	
			a	b
Mach number		$U(a,b)$	0.71	0.77
weight	lb	$U(a,b)$	- 2000	2000

The uncertain weight, w, considers weight variation on the payload and fuel weight. This weight is added to the weight of the aircraft which is calculated according as follow :

$$W = w_o + w_w + w,$$

where the weight $w_o = 15736$ lb includes the weight of the fuselage, systems, and fuel, these are considered to be fixed since no change in this part of the aircraft is allowed. The weight of the wings, w_w, is calculated according to the statistical group weights method [98].

6.3.4   Results

In all previous test cases presented in this dissertation, the actual Pareto front was assumed to be the front calculated by a multi-objective genetic algorithm (MO-GA) and the quasi-Monte Carlo (quasi-MC). However, in the present test case due to

the significant higher cost of the analysis codes this Pareto front is not obtained. Consequently, no comparisons for different UP methods with multi-objective genetic algorithm are given.

It was previously observed that the Pareto fronts calculated by a MO-GA and the gPC-SG was in good agreement with those of MO-GA and the quasi-MC. For the present test case, advantage is taken of the ability of the gPC-SG to reproduce results of more expensive methods such as quasi-MC, and thus the actual Pareto front is considered to be that of the MO-GA and the gPC-SG.

6.3.4.1 *Single-level and bi-level gPC-SG based robust optimization*

In order to avoid the computational burden of approximating Pareto front with multi-objective genetic algorithm, the single and bi-level robust design strategies proposed in the previous chapter are applied here for the robust design of the business jet transonic wing. The single-level strategy employs only one level of fidelity of the uncertainty propagation method, a high fidelity UP that is the gPC-SG. The bi-level strategy considers a second level of fidelity of the UP method. This additional UP is a low fidelity method.

Similarly to the airfoil case, the gPC-SG with a sparse integration level $l = 1$ is considered as the low UP. This choice avoids the additional computational cost of the low UP while performing adaptive sampling due to the nested nature of the sparse grid node distribution. The high fidelity UP is also the gPC-SG, whereas at a sparse integration level of $l = 3$.

The search of the Pareto front is shown in figure 27 after 25, 50, and 100 adaptive samples. As a reference the Pareto front calculated by the MO-GA and the gPC-SG are also shown and it is considered to be the actual front. The single level is initialized with 10 designs, whereas the bi-level strategy in adition is initialized with 100 designs for the low fidelity UP. However, due to the constrain only 8 and 79 designs are

feasible for the high and low fidelity UP, respectively. Similar to the previous test cases, the kriging, and co-kriging models of the single and bi-level strategies are updated and tuned after every new adaptive sample by maximizing their respective likelihood function with a genetic algorithm.

Both strategies are able to place more designs either at the Pareto front or in its the near region as the number of adaptive samples increases. This can be seen, for instance, for the single level approach after 25 adaptive samples in which its current non-dominated set, symbolized by blue circles, is approaching the actual front, and 3 designs are placed at the Pareto front. As the number of adaptive samples increases, the non-dominated set does not seem to move close to the Pareto front although the number of non-dominated designs at the actual front has increased to 6 as shown in figure 27(c) for 50 adaptive samples. Instead, areas that are not in the near region of the Pareto front are explored, and thus most of the samples are placed in regions away from the actual front. However, in spite of continuing exploring these areas, the single-level strategy is able to place more designs at the Pareto front as seen in figure 27(e) for 100 adaptive samples. In this figure, 13 designs can be seen at the actual front.

The bi-level approach seems to explore less areas of no interest, and thus is able of placing more design at the Pareto front as seen in figure 27(b) for 25 adaptive samples at which 8 designs are located at the Pareto front. As the number of adaptive samples increases, the exploration of regions of no interest occurs as well; however, more designs are still placed at and in the near region of the actual front, for instance at 50 adaptive samples, 14 design are found at the Pareto front as shown in figure 27(d). This situation continues and at 100 adaptive samples iterations, 23 designs are located at the actual Pareto front as shown in figure 27(f).
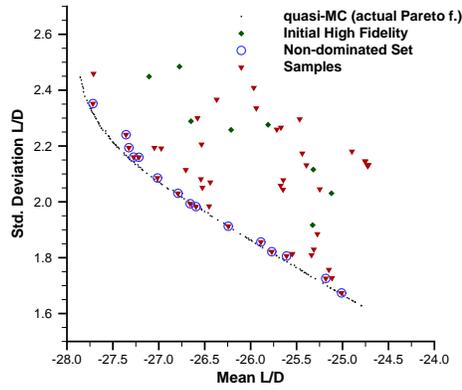
It must be noticed that for both approaches the exploration of areas of no interest is much higher compared to the airfoil case and the analytical test cases. This
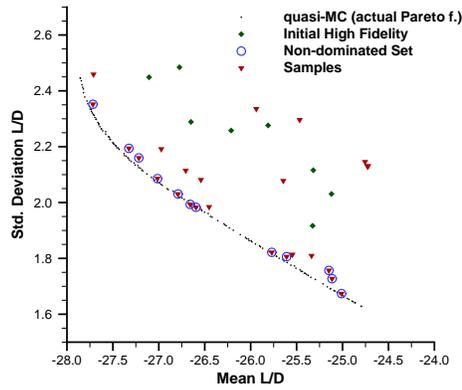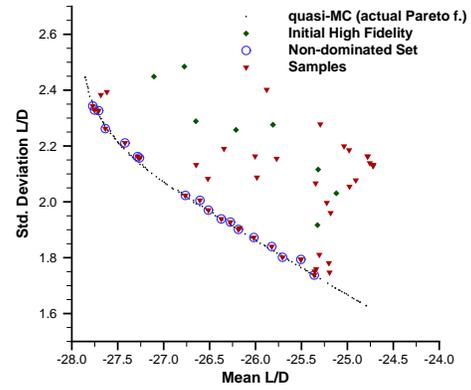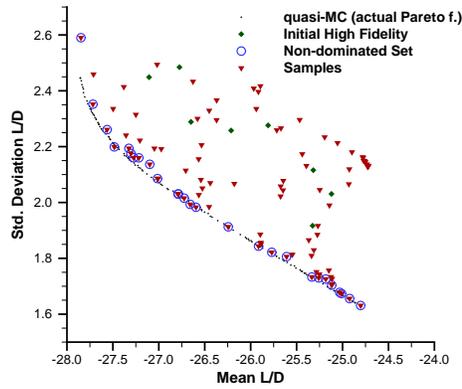
(a) Single-level, 25 samples
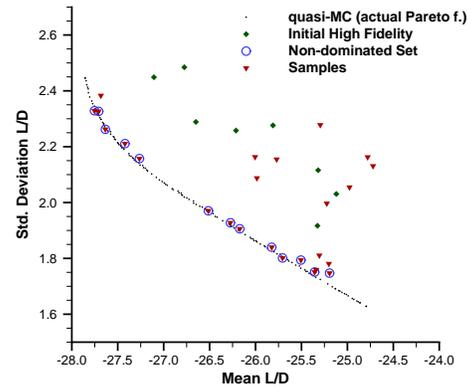
(b) Bi-level, 25 samples

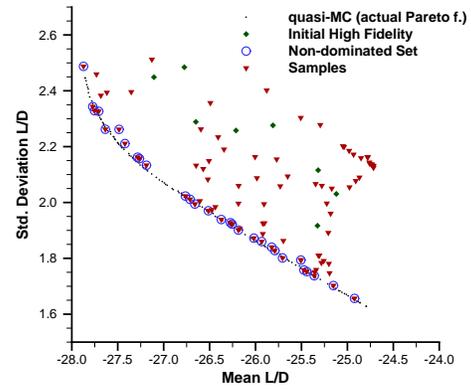(c) Single-level, 50 samples

(d) Bi-level, 50 samples

(e) Single-level, 100 samples

(f) Bi-level, 100 samples

Figure 27: Search of Pareto front by the single-level and bi-level robust design strategies after 25, 50, and 100 adaptive samples

is inevitably a consequence of the higher dimensionality of the design space of the transonic wing case.

6.3.4.2 Computational cost comparison

Previously it was shown that for the same number of adaptive iteration, the bi-level robust design strategy performs better than the single level strategy. This follows a similar trend to what was found for the airfoil case and the analytical test function cases. This result is, however, no surprising since information from the low fidelity UP is provided to the bi-level approach in addition to the high fidelity UP. Therefore, the bi-level strategy always starts with more information. Because of this, the correct mean to measure the performance of both approaches is by comparing the computational cost (function calls) instead of adaptive iterations.

In the previous chapter, the following criteria :

i. Number of non-dominated designs located at the actual Pareto front,

ii. Average distance of the non-dominated set to the actual Pareto front,

were defined for measuring effectiveness and they are employed here. At a determine adaptive sample iteration, a member of the current Pareto set is considered to be at the actual Pareto front if its distance is lower than a threshold, for the present case of $\delta < 0.0175$.

The performance as function of the computational cost of the single and bi-level strategies is shown in figure 28. It must be noticed that the initial cost of the bi-level strategy is much higher for this case than for all the previous test cases. This in turn increases the difference of the initial computational cost of both strategies. This is a direct consequence of the higher dimensionality (4 design variables) in the design space which in turn requires a larger sample for the low fidelity UP of the bi-level strategy.

The number of non-dominated designs at the actual front is shown in figure 28(a). It is noticed that this plot can be divided in two regions. In the fir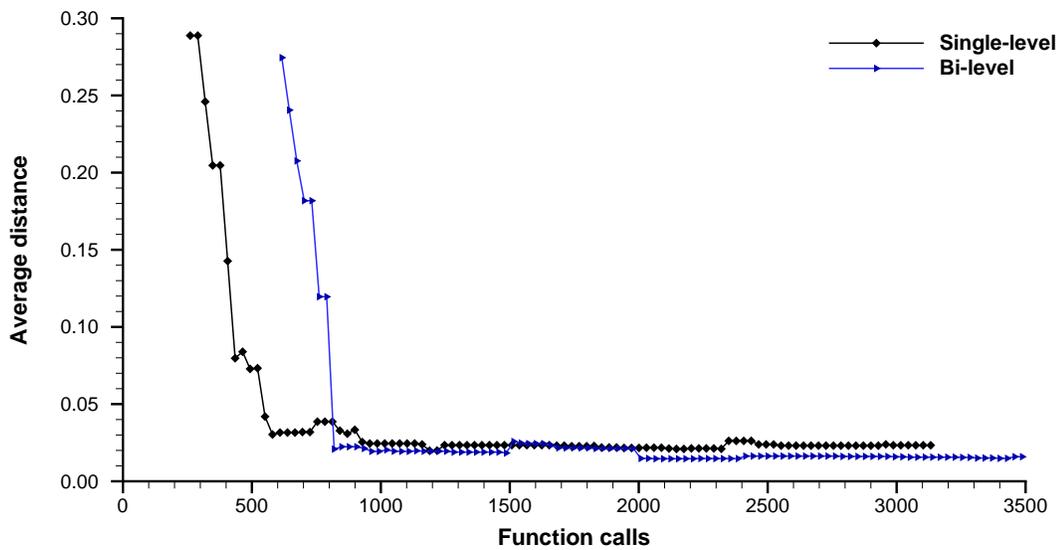st one, for computational budgets smaller than approximately 1050 function calls, the single-level strategy performs better than the bi-levels strategy, by placing more designs at the Pareto front. This region is strongly influenced by the initial computational cost of both strategies. The single-level counts with the difference of the budget between both approaches to place designs at the Pareto front. In the present case, this difference is 355 function calls. Furthermore, in addition to the difference in computational cost, the single-level has about 435 function calls (16 adaptive samples) before the bi-level strategy equates its number of non-dominated designs at the Pareto front. In the second region, for computational budgets larger than 1050 function calls, the bi-level strategy is able to place more non-dominated designs at the actual Pareto front than the single level for the computational budget. Consequently, in that region the bi-level strategy performs better.

The second metric, the average distance to the actual Pareto front, is shown in figure 28(b). During the first adaptive samples, both strategies decrease considerably the average distance. For instance, it takes approximately 174 function calls (6 adaptive samples) for the single-level strategy to decrease the average distance from 0.28 to 0.08, and for the bi-levels strategy, it takes about 203 function calls (7 adaptive samples) to reduce the average distance from 0.30 to 0.03. Similar to the first metric, this plot can be divided in two regions.

In the first one, for budgets lower than 812 function calls, the average distance of both approaches is strongly influenced by the initial computational cost. Therefore, in this region the bi-level strategy does not offer any advantage, and it takes some computational budget for the bi-level strategy to attain comparable average distance of the single-level; this occurs at a budget of approximately 812 function calls. In the second region, for budgets greater than 812 function calls, the bi-levels strategy has a
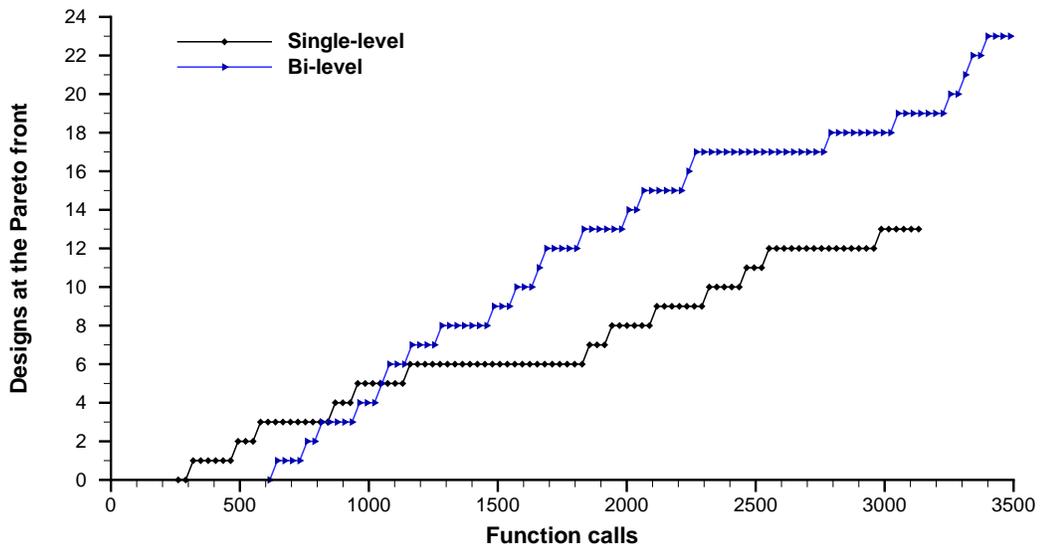
(a)

(b)

Figure 28: Designs at the Pareto front Fig. (a) & Average distance Fig. (b)

slightly shorter distance than the single-level strategy although in the range of 1515 to 1980 function calls the average distance for both approaches is almost the same

and equal to 0.02. However, for larger computational budgets the bi-level strategy again gives a slightly shorter distance.

In summary, although the rate of placing designs at the Pareto front is higher for the bi-level strategy, there is considerable range of function calls in which the single-level strategy performs better than the bi-level strategy. This results from the fact that initially there is a considerable difference in the cost between both approaches. Therefore, there is a number of adaptive samples required for the bi-level strategy to attain the same number of designs at the Pareto front of the single-level. In the present case, due to low rate of placing design at the Pareto front of the single-level strategy, this occurs at computational budget of approximately 1050 function calls. For computational budgets greater than that, the bi-level strategy places more designs at the actual front.

6.4   Considerations and limitations

There are some considerations and limitations to be accounted when applying the proposed strategies to design under uncertainty.

6.4.1   gPC-SG UP strategy

This strategy is subjected to the mathematical requirements of the polynomial chaos method as well as the sparse grids. The most important requirement for the gPC-SG strategy is smoothness in the stochastic space. Although the sparse grid integration technique is able to deal with discontinuous integrand given the proper basis such as multilinear or wavelet basis, the polynomial chaos (PC) basis requires smoothness in the stochastic space. This is a consequence of the spectral nature of the gPC representation. Therefore, as long as the cost function, $\mathcal{J}$, is continuous although it can be highly non-linear, the gPC-SG strategy can be used.

Another consideration is the order "p" of the polynomial chaos. Theoretically, the higher the chaos order, the more accurate the gPC approximation. Previous studies

in stochastic PDE's have shown that chaos of third or fourth order are enough to represent a second order stochastic process. However, unlike the intrusive gPC in which the chaos order affects directly the size of the PDE's system to be solved, the non-intrusive gPC is affected differently by the chaos order. The chaos order influences the number expansion coefficients and hence the number of calculations. However, for the non-intrusive polynomial chaos the main limitation is not the number of terms of the gPC expansion, but the number of evaluation of the cost function $\mathcal{J}$ (function calls) since it is considered that the computational cost of the cost function (analysis) is more expensive than the computation of the expansion coefficients. Therefore, in the present strategy higher chaos order can be used without compromising the the overall computational cost of the UP strategy.

The last consideration is the sparse grid level " l." This is a very important parameter of the gPC-SG strategy since it controls the number of cost function evaluations (the computational expense). High levels of the sparse grid integration leads to more accurate calculations of the gPC expansion coefficients. However, for practical use, it is not recommendable to increase the sparse grid level too high. This is because the computational expense increases with the level as well as the dimensionality of the stochastic space. In practice, it is desirable to maintain low levels of 2 or 3. This can be done by setting up a threshold in the level. In addition, the level can also be controlled by setting a threshold in the approximation of the statistical moments with the level.

In all the robust optimization problems, it was shown that an sparse grid level of $l = 3$, and polynomial chaos order of $p = 6$ were enough to approximate the results obtained by the quasi-Monte Carlo method.

6.4.2 Single-level gPC-SG based robust optimization strategy

The single-level strategy is restricted by the limitation of the gPC-SG strategy as well as those of the multi-objective expected improvement (MO-EI), and the Gaussian processes (GP). The gPC-SG limitations were already mentioned and not repeat here for brevety. A common limitation of the MO-EI along with any other adaptive sampling technique is the lack of a stopping criteria. In this work, it was chosen to stop the adaptive sampling process at a determine budget which is set up by the user. Regarding the GP process, the main limitation is the number of data that can be used. Interpolation GP processes such as kriging requires inversion of $N \times N$ matrices, where N is the size of the data. Inversion have a computational cost that scales with $\mathcal{O}(N)^3$, and thus this cost can grow quickly for data of large size. In this work, the size of data has not been an issue since the data for all the test cases were of relatively small size. However, for more realistic problems other types of approaches may be considered, for instance regression type of GP such as the relevance vector machine (RVM).

6.4.3 Bi-level gPC-SG based robust optimization strategy

Among the three approaches presented in this dissertation, it is the bi-level strategy that requires the most consideration. In addition to all the consideration and limitation of the gPC-SG, the MO-EI, and GP, other aspects must be considered for its use.

The first aspect to consider is the relative computational cost between the low and the high fidelity uncertainty propagation methods. In general, large cost ratios favors the bi-level strategy. There are two cases in which this ratio increases. The first case is for large degree of non-linearity of the cost function and uncertainty. This was the object of study in chapter V and gave support to the third research question: *"how is the bi-level strategy affected by levels of non-linearity and uncertainty?"*. Large ratios

are also found as the number of uncertain parameters increases. This occurs because the computational cost of the high fidelity UP grows faster than the low fidelity UP. The cost as a function of the uncertain parameters is shown in figure 29(a) for the gPC-SG and the LE method, whereas the cost ratio between the gPC-SG and the LE method is shown in figure 29(b).
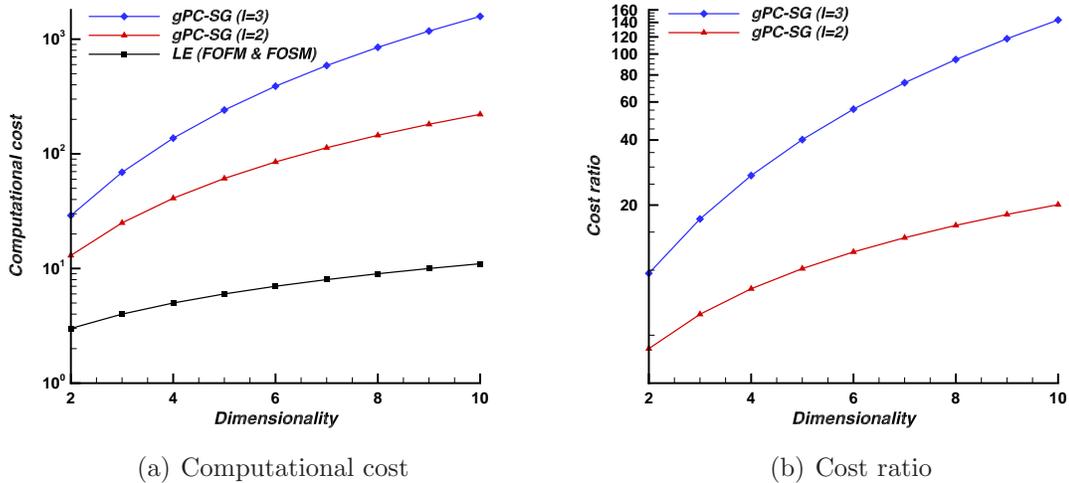

(a) Computational cost

(b) Cost ratio

Figure 29: Computational cost (a) and cost ratio (b) for the gPC-SG strategy

The second aspect is the initial computational cost of the bi-level strategy compared to that of the single-level strategy. In general, this cost is always higher for the bi-level strategy due to the information of the low fidelity UP. The main reason for any increase of the amount of data required for the low fidelity UP is the dimensionality of the design space. As this dimensionality increases, so does the size of initial sample of the low fidelity UP. This is unavoidable since any useful information of the low fidelity UP comes from having a global information of the design space. This ultimately affects the performance of the bi-level strategy. For instance, in the case of the low Reynold airfoil case, the bi-level strategy outperform the single level strategy. For this case the dimensionality in design space and stochastic space was 2. However, in the transonic wing case, the dimensionality of the design space was 4,

whereas the stochastic space remained the same, i.e. 2. This increase in the dimensionality demanded a larger amount of data for the low fidelity UP. As a consequence, the advantage of the bi-level strategy was only seen for large computational budgets since at lower budgets the single-level outperformed the bi-level strategy. A possible mean to alleviate the influence of the initial cost of the low fidelity UP is to have large ratio of the high to the low fidelity computational cost. This in turn makes the initial cost of the low UP less significant than the cost of the high fidelity UP.

CHAPTER VII

CONCLUSIONS

An approach for robust design based on stochastic expansions was investigated. The research is divided in two parts : 1) stochastic expansions for uncertainty propagation and 2) adaptive sampling for Pareto front approximation. For the first part, a strategy based on the non-intrusive generalized polynomial chaos (gPC) expansion method is developed. Second, in order to alleviate the computational cost of approximating the Pareto front, two strategies based on adaptive sampling for multi-objective problems are presented. The first one is based on the two aforementioned methods, whereas the second one considers, in addition, two levels of fidelity of the uncertainty propagation method. The proposed approaches were tested successfully in the robust optimization of a low Reynolds number airfoil and a transonic wing with uncertain operating conditions. The gPC-based method is able to find the same Pareto front as a reference Monte Carlo-based strategy but with lower computational cost. The bi-level strategy shows further computational efficiency. Based on this research, the following conclusions are drawn.

The primary research question in this dissertation was to investigate a common challenge in design under uncertainty: how can uncertainty be propagated efficiently for robust design purposes so the computational burden of simulated-based design under uncertainty is reduced? Common past approaches rely on either methods that are computationally cheap, such as local expansion based methods, or expensive methods such as Monte Carlo. In order to address this general problem, this thesis investigated specific implementations which accomplished reduction of the computational burden by improving the efficiency of (1) the uncertainty propagation method and (2) the

robust optimization formulation.

First, a stochastic expansion-based strategy for uncertainty propagation was presented. It employs the non-intrusive generalized polynomial chaos (gPC) expansion. The computational cost of calculating the expansion coefficients is alleviated by adopting a sparse grid (SG) integration technique. This is an advantage for propagating uncertainties, especially as the number of uncertain parameters increases. It is also the main difference between the presented gPC-SG strategy and previous approaches that employed the chaos expansion. Comparisons with expensive UP methods such as those based Monte Carlo showed the usefulness of this strategy.

Second, in the robust optimization part, two strategies were presented. The first strategy combines the above UP strategy and adaptive sampling techniques for multi-objective optimization in order to efficiently approximate the Pareto front. The second strategy considers two levels of fidelity of the uncertainty propagation method. In the latter strategy, the optimization objectives are calculated by two UP methods having different levels of fidelity. The main idea is that information from a less accurate but cheap UP method alleviates the use of a more accurate but expensive method. The proposed gPC-SG strategy is used as the high fidelity UP method, whereas a less sophisticated method is adopted as the low fidelity. In order to efficiently sample the design space, adaptive sample techniques are also used.

The two robust design strategies were successfully tested on the robust optimization problem of a low Reynolds number airfoil. Both strategies were able to gradually place designs at the actual Pareto front and to reduce the average distance of the non-dominated set to the actual front as the number of adaptive sample increases. However, the bi-level strategy showed better performance than the single level strategy leading to more designs at the Pareto front and shorter average distances from the non-dominated set to the actual front for the same computational cost

Nevertheless, effective use of the bi-level strategy requires much more consideration. First, in order to achieve a benefit over the single-level method, the relative ratio of the cost of the high fidelity and low fidelity UP needs to be high. This ratio increases because of the degree of nonlinearity, uncertainty and number of uncertain parameters. Second, there needs to be a balance between the number of stochastic and design variables. This was shown in the transonic wing case. Although the relative cost ratio between the low and the high fidelity UP was the same as in the airfoil case, it was shown that the performance of the bi-level strategy was dependent on the total computational budget. This is an unavoidable consequence of the higher dimensionality of the design space which in turn increases the initial cost of the low fidelity UP.

Recommendations for future work

Although this dissertation contributes to the mitigation of the computational cost of design under uncertainty, it must be pointed out that all strategies presented are preliminary. Design under uncertainty poses many challenges and opportunities that require intensive future research.

First, alleviating the cost of propagating uncertainties still requires further research. Although the use of sparse grids reduces the computational cost, this still suffers from the curse of dimensionality. A potential improvement on this is the use of sensitivity information from the adjoint method. In design, adjoint methods have been mostly used for gradient based optimization, but these methods are potentially useful in uncertainty propagation since the sensitivity information can be obtained at a cost that is independent of the number of uncertain parameters. The main idea is to extend the use of adjoint methods to more general UP method such as stochastic expansions and not merely its immediate and simple application to methods such as local expansion.

The second area for future research is in efficient multifidelity methods for approximating the Pareto front. Such research could focus on either on its traditional use for modeling the fidelity of physics or as presented in this dissertation, by modeling the fidelity of the uncertainty propagation method. Multi-fidelity methods seem very promising since optimization objectives can be an outcome of a large size sample of the cost function. This computational burden is aggravated if the cost function is computationally expensive, e.g. those resulting from high fidelity analysis codes. A multi-fidelity strategy using global surrogate modeling was developed in this work. However, a different path could be to explore the application multi-fidelity approaches from a local perspective.

REFERENCES

[1] ACHATZ, S., "Higher order sparse grid method for elliptic partial differential equations with variable coefficients," *Computing*, vol. 71, no. 1, pp. 1–15, 2003.

[2] ALEKSEEV, A. K. and NAVON, I. M., "Calculation of uncertainty propagation using adjoint equations," *International Journal of Computational Fluid Dynamics*, vol. 17, no. 4, pp. 283–288, 2003.

[3] ALEKSEEV, A. K., NAVON, I. M., and ZELENTSOV, M. E., "The estimation of functional uncertainty using polynomial chaos and adjoint equations," *International Journal for numerical methods in fluids*, vol. 67, no. 3, pp. 328–341, 2010.

[4] ALLEN, J. K., SEEPERSAD, C., CHOI, H., and MISTREE, F., "Robust design for multiscale and multidisciplinary applications," *Journal of mechanical design*, vol. 128, no. 4, pp. 832–843, 2006.

[5] ALVAREZ, M. and LAWRENCE, N. D., "Sparse convolved gaussian processes for multi-output regression," in *Advances in Neural Information Processing Systems 21* (KOLLER, D., SCHUURMANS, D., BENGIO, Y., and BOTTOU, L., eds.), pp. 57–64, 2009.

[6] ANG, A. H.-S. and TANG, W. H., *Probability concepts in engineering planning and design.* New YORK: Wiley,, 1975.

[7] ASKEY, R. and WILSON, J., *Some basic hypergeometric polynomials that generalize Jacobi polynomials*, vol. 54. Providence, Rhode Island: American mathematical society, 1985.

[8] AUGUSTIN, F., GILG, A., PAFFRATH, M., RENTROP, P., and WEVER, U., "Polynomial chaos for the approximation of uncertainties: chances and limits," *European Journal of Applied Mathematics*, vol. 19, no. 2, pp. 149–190, 2008.

[9] BARTHELMANN, V., NOVAK, E., and RITTER, K., "High dimensional polynomial interpolation on sparse grids," *Advances in Computational Mathematics*, vol. 12, 2000.

[10] BELLMAN, R. E., *Dynamic Programming.* New Jersey: Princeton University Press,, 1957.

[11] BELLMAN, R. E., *Adaptive control processes: a guided tour.* New Jersey: Princeton University Press,, 1961.

[12] Blander, J., Biernacki, R., Chen, S., Grobelny, P., and Hemmers, R., "Space mapping technique for electromagnetic optimization," *IEEE Transactions on Microwave Theory and Techniques*, vol. 42, no. 12, pp. 2536–5422, 1994.

[13] Boyle, P. and Frean, M., "Dependent gaussian processes," in *Advances in Neural Information Processing Systems 17* (Saul, L. K., Weiss, Y., and Bottou, L., eds.), pp. 217–224, Cambridge, MA: MIT Press, 2005.

[14] Bungartz, H.-J. and Griebel, M., "Sparse grids," *Acta Numerica*, vol. 13, 2004.

[15] Bungartz, H.-J., *Finite elements of higher order on sparse grids.* Aachen: Sharker Verlag, 1998.

[16] Bungartz, H.-J. and Dornseifer, T., "Sparse grids: Recent developments for elliptic partial differential equations," in *Multigrid methods V* (Hackbusch, W. and Wittum, G., eds.), vol. 3 of *Lecture notes in computational science and engineering*, (Berlin, Germany), pp. 89–114, Springer, 1998.

[17] Bungartz, H.-J. and Dornseifer, T., "Multivariate quadrature on adaptive sparse grids," *Computing*, vol. 71, no. 1, pp. 89–114, 2003.

[18] Caflisch, R. E., "Monte carlo and quasi-monte carlo methods," *Acta Numerica*, vol. 7, pp. 1–49, 1998.

[19] Chassaing, J.-C. and Lucor, D., "Stochastic investigation of flows about airfoils at transonic speeds," *AIAA Journal*, vol. 48, no. 5, pp. 938–950, 2010.

[20] Chen, Q.-Y., Gottieb, D., and Hesthaven, J., "Uncertainty analysis for the steady-state flows in a dual throat nozzle," *Journal of computational physics*, vol. 204, no. 1, pp. 378–398, 2005.

[21] Chung, H.-S. and Alonso, J. J., "Design of a low-boom supersonic business jet using cokriging approximation models," No. AIAA-2002-5598, (Atlanta, GA), 9th AIAA/ISSMO Symposium on Multidisciplinary Analysis and Optimization, September 2002.

[22] Chung, H.-S. and Alonso, J. J., "Using gradients to construct cokriging approximation models for high-dimensional design optimization problems," No. AIAA-2002-0317, (Reno, NV), 40th AIAA Aerospace Science Meeting and Exhibit, January 2002.

[23] Cook, P. H., McDonald, M. A., and Firmin, M., "Aerofoil rae 2822-pressure distributions, and boundary layer and wake measurements," Tech. Rep. AGARD-AR-138, AGARD, Neuilly-sur-Seine, France, May 1979.

[24] Cressie, N. A. C., *Statistics for spatial data.* New York: J. Wiley,, 1993.

[25] DEBUSSCHERE, B. J., NAJM, H. N., PEBAY, P. P., KNIO, O. M., G, R. G. G. R., and LEMAÎTRE, O. P., "Numerical challenges in the use of polynomial chaos representations for stochastic processes," *SIAM Journal on Scientific Computing*, vol. 26, no. 2, pp. 698–719, 2004.

[26] DELVOS, F. J. and SCHEMPP, W., *Boolean methods in interpolation and approximation.* Pitman research notes in mathematics series 230, Harlow, Essex, England: Longman scientific and technical, 1989.

[27] DODSON, M. and PARKS, G. T., "Robust aerodynamic design optimization using polynomial chaos," *Journal of Aircraft*, vol. 46, no. 2, pp. 635–646, 2009.

[28] DRELA, M., "XFOIL: an analysis and design system for low reynolds number airfoils," in *Low Reynolds number aerodynamics, Proceedings of the conference* (MUELLER, T. J., ed.), no. 54 in Lecture notes in engineering, (Notre Dame, Indiana), pp. 1–12, June 1989.

[29] DRELA, M., "Integral boundary layer formulation for blunt trailing edges," No. AIAA-1989-2166, (Seatle, WA), 7th AIAA Applied Aerodynamics Conference, Aug. 1989.

[30] DRELA, M., *A user's guide to MSES 3.04.* Cambridge, MA: MIT computational aerospace science lab., 2006.

[31] DRELA, M. and GILES, M. B., "Viscous-inviscid analysis of transonic and low reynolds number airfoils," *AIAA Journal*, vol. 25, no. 10, pp. 1347–1355, 1987.

[32] DRELA, M. and YOUNGREN, H., *Anthena Vortex Lattice Program 3.31.* http://web.mit.edu/drela/Public/web/avl/: MIT computational aerospace science lab., 2011.

[33] ELLISON, S. L. R., M., R., and WILLIAMS, A., *Quantifying uncertainty in analytical measurement.* EURACHEM/CITAC, 2000.

[34] FONSECA, C. M. and FLEMING, P. J., "An overview of evolutionary algorithms in multiobjective optimization," *Evolutionary Computation*, vol. 3, no. 1, pp. 1–16, 1995.

[35] FORRESTER, A. I. J. and KEANE, A. J., "Recent advances in surrogate-based optimization," *Progress in Aerospace*, vol. 45, 2009.

[36] FORRESTER, A. I. J., SOBESTER, A., and KEANE, A. J., "Multi-fidelity optimization via surrogate modeling," *Proceedings of the Royal Society A*, vol. 463, no. 4, pp. 3251–3269, 2007.

[37] GANO, S. E. and RENAUD, J. E., "Hybrid variable fidelity optimization by using a kriging-based scaling function," *AIAA Journal*, vol. 43, no. 11, pp. 2422–2430, 2005.

[38] GENZ, A. C., "A package for testing multiple integration subroutines," in *Numerical Integration* (KEAST, P. and FAIRWEATHER, G., eds.), pp. 337–340, Holland: Kluwer and Dordrecht, 1987.

[39] GERSTNER, T. and GRIEBEL, M., "Numerical integration using sparse grids," *Numerical Algorithms*, vol. 18, 1998.

[40] GERSTNER, T. and GRIEBEL, M., "Dimension-adaptive tensor-product quadrature," *Computing*, vol. 71, no. 1, pp. 65–87, 2003.

[41] GHANEM, R. and DHAM, S., "Stochastic finite element analysis for multiphase flow in heterogeneous porous media," *Transport in Porous Media*, vol. 32, no. 3, pp. 239–262, 1998.

[42] GHANEM, R. G. and SPANOS, P. D., *Stochastic finite elements: a spectral approach.* New York: Springer-Verlag, 1991.

[43] GHATE, D. and GILES, M. B., "Inexpensive monte carlo uncertainty analysis," (Hyderabad, India), 2nd Symposium on Applied Aerodynamics and Design of Aerospace Vehicles - SAROD 2005, December 2005.

[44] GHISU, T., PARKS, G. T., JARRET, J. P., and CLARKSON, P. J., "Adaptive polynomial chaos for gas turbine compresion systems performance analysis," *AIAA Journal*, vol. 48, no. 6, pp. 1156–1170, 2010.

[45] GHISU, T., PARKS, G. T., JARRET, J. P., and CLARKSON, P. J., "Robust design optimization of gas turbine compression systems," *Journal of Propulsion and power*, vol. 27, no. 2, pp. 282–295, 2011.

[46] GHISU, T., JARRET, J. P., and PARKS, G. T., "Robust design optimization of airfoils with respect to ice accretion," *Journal of Aircraft*, vol. 48, no. 1, pp. 287–304, 2011.

[47] GILES, M. and DRELA, M., "A two-dimensional transonic aerodynamic design method," No. AIAA-1986-1793, (Washington, DC), AIAA meeting, Jan. 1986.

[48] GILES, M., DRELA, M., and THOMPKINS, W. T., "Newton solution of direct and inverse transonic euler equations," No. AIAA-1985-1530, (Washington, DC), AIAA meeting, Jan. 1985.

[49] GOOVAERTS, P., *Geostatistics for natural resources evaluation.* New York: Oxford University press, 1997.

[50] GORDON, W. J., "Blending function methods of bivariate and multivariate interpolation and approximation," *SIAM Journal on Numerical Analysis*, vol. 8, pp. 158–177, 1971.

[51] GRIEBEL, M., "Sparse grids and related approximation schemes for higher dimensional problems," *Foundations of Computational Mathematics*, no. 248, 2005.

[52] GUMBERT, C. R., NEWMAN, P., and HOU, G. J.-W., "Effect of random uncertainty on the computational design of a 3-d flexible wing," No. AIAA-2002-2806, (St. Louis, MO), 20th AIAA Applied Aerodynamics Conference, June 2002.

[53] HALD, A., *Statistical theory engineering applications.* New York: Wiley, 1952.

[54] HOSDER, S., WALTERS, R. W., and PEREZ, R., "A non-intrusive polynomial chaos method for uncertainty propagation in cfd simulations," No. AIAA-2006-891, (Reno, NV), 44th AIAA Aerospace Sciences Meeting and Exhibit, Jan 2006.

[55] HUANG, D., ALLEN, T. T., NOTZ, W. I., and MILLER, R. A., "Sequential kriging optimization using multiple-fidelity evaluations," *Structures and Multidisciplinary Optimization*, vol. 32, 2006.

[56] HUFF, D. L., WU, J.-C., and SANKAR, L., "Analysis of viscous transonic flow over airfoil sections," No. AIAA-1987-0420, (Reno, NV), AIAA 25th Aerospace Sciences Meeting, Jan. 1987.

[57] HUYSE, L., "Free-form airfoil shape optimization under uncertainty using maximum expected value and second-order second-moment strategies," Tech. Rep. CR-2001-211020, NASA, Langley Research Center, Virginia, June 2001.

[58] HUYSE, L., "Solving problems of optimization under uncertainty as statistical decision problems," No. AIAA-2001-1519, (Seattle, WA), 42nd AIAA/ASME/ASCE/AHS/ASC Structures, Structural Dynamics, and Materials Conference and Exhibit, April 2001.

[59] HUYSE, L. and LEWIS, R. M., "Aerodynamic shape optimization of two-dimensional airfoils under uncertain conditions," Tech. Rep. CR-2001-210648, NASA, Langley Research Center, Virginia, Jan. 2001.

[60] HUYSE, L., PADULA, S. L., LEWIS, R. M., and LI, W., "Probabilistic approach to free-form airfoil shape optimization under uncertainty," *AIAA Journal*, vol. 40, no. 9, pp. 1764–1772, 2002.

[61] JONES, D. R., SCHONLAU, M., and WELCH, W. J., "Efficient global optimization of expensive black-box functions," *Journal of Global Optimization*, vol. 13, no. 4, pp. 455–492, 1998.

[62] KEANE, A., "Statistical improvement criteria for use in multiobjective design optimization," *AIAA Journal*, vol. 44, no. 4, pp. 879–891, 2006.

[63] KEANE, A. J. and NAIR, P. B., *Computational approaches for aerospace design.* New York: Wiley, 2005.

[64] KENNEDY, M. C. and O'HAGAN, A., "Predicting the output from a complex computer code when fast approximations are available," *Biometrika*, vol. 87, no. 1, pp. 1–13, 2000.

[65] KLIMKE, W. A., *Uncertainty modeling using fuzzy arithmetic and sparse grids.* PhD dissertation, University of Stuttgart, Institute of Applied Analysis and Numerical Simulation, Nov. 2005.

[66] KUYA, Y., TAKEDA, K., ZHANG, X., and FORRESTER, A. I. J., "Multifidelity surrogate modeling of experimental and computational aerodynamic data set," *AIAA Journal*, vol. 49, no. 2, pp. 289–298, 2011.

[67] LEE, C. H., *Bayesian Collaborative Sampling: Adaptive Learning for Multidisciplinary Design.* PhD dissertation, Georgia Institue of Technolgy, School of Aerospace Engineering, Dec. 2011.

[68] LEE, C. H., *CFD Analysis of a Transonic Business Jet Wing.* Atlanta, GA: Internal technical report, Aerospace Systems Design Laboratory, Georgia Institute of Technology, 2012.

[69] LEE, S. H. and CHEN, W., "A comparative study of uncertainty propagation methods," *Structural Multidisciplinary Optimization*, vol. 37, no. 3, pp. 239–253, 2009.

[70] LEMAÎTRE, O. P., KNIO, O. M., NAJM, H. N., and GHANEM, R. G., "A stochastic projection method for fluid flow: I. basic formulation," *Journal of computational physics*, vol. 173, no. 2, pp. 481–511, 2001.

[71] LEMAÎTRE, O. P., REAGAN, M. T., NAJM, H. N., GHANEM, R. G., and KNIO, O. M., "A stochastic projection method for fluid flow: II random process," *Journal of computational physics*, vol. 181, no. 1, pp. 9–44, 2002.

[72] LI, G., ROSENTHAL, C., and RABITZ, H., "High dimensional model representations," *The Journal of Physical Chemistry A*, vol. 105, no. 33, pp. 7765–7777, 2001.

[73] LIN, G., SU, C.-H., and KARNIADAKIS, G., "Predicting shock dynamics in the presence of uncertainties," *Journal of computational physics*, vol. 217, no. 1, pp. 260–276, 2006.

[74] MA, X. and ZABARAS, N., "An adaptive hierarchical sparse grid collocation algorithm for the solution of stochastic differential equations," *Journal of computational physics*, vol. 228, no. 8, pp. 3084–3113, 2009.

[75] MACKAY, D. J. C., *Information Theory, Inference, and Learning Algorithms.* Cambridge, U.K.: Cambridge University Press, 2003.

[76] MATHELIN, L. and HUSSAINI, M., "A stochastic collocation algorithm for uncertainty analysis," Tech. Rep. CR-2003-212153, NASA, Langley Research Center, Virginia, Feb. 2003.

[77] MATHERON, G., "Principles of geostatistics," *Economic Geology*, vol. 58, no. 8, pp. 1246–1266, 1963.

[78] MYERS, R. H. and MONTGOMERY, D. C., *Response Surface Methodology: Process and Product Optimization Using Designed Experiments*. New York: John Wiley and Sons, 1995.

[79] NAJM, H. N., "Uncertainty quantification and polynomial chaos techniques in computational fluid dynamics," *Annual Review of Fluid Mechanics*, vol. 41, pp. 35–52, 2009.

[80] NOVAK, E. and RITTER, K., "High dimensional integration of smooth functions over cubes," *Numerische Mathematik*, vol. 75, 1996.

[81] NOVAK, E., RITTER, K., SCHMITT, R., and STEINBAUER, A., "On an interpolary method for high dimensional integration," *Journal of Computational and Applied Mathematics*, vol. 112, 1999.

[82] OBERKAMPF, W. L., DELAND, S. M., RUTHERFORD, B. M., DIEGERT, K. V., and ALVIN, K. F., "Error and uncertainty in modeling and simulation," *Reability engineering and system safety*, vol. 75, no. 3, pp. 333–357, 2002.

[83] OBERKAMPF, W. L., HELTON, J. C., JOSLYN, C. A., WOJTKIEWICZ, S. F., and FERSON, S., "Challenge problems: uncertainty in ssystem response given uncertain parameters," *Reability engineering and system safety*, vol. 85, no. 1-3, pp. 11–19, 2004.

[84] O'HAGAN, A. and KINGMAN, J. F. C., "Curve fitting and optimal design for prediction," *Journal of the Royal Society Series B*, vol. 40, no. 1, pp. 1–42, 1978.

[85] PADULO, M., CAMPOBASSO, M. S., and GUENOV, M. D., "Novel uncertainty propagation method for robust aerodynamic design," *AIAA Journal*, vol. 49, no. 3, pp. 530–543, 2011.

[86] PARK, G.-J., LEE, T.-H., LEE, K. H., and HWANG, K.-H., "Robust design : an overview," *AIAA Journal*, vol. 44, no. 1, pp. 181–191, 2006.

[87] PETTIT, C. L., CANFIELD, R. A., and GHANEM, R., "Stochastic analysis of an aerolastic system," (New York, NY), 15th ASCE Engineering Mechanics Conference, June 2002.

[88] PHADKE, M. S., *Quality engineering using robust design.* Englewood Cliffs, N.J.: Prentice Hall, 1989.

[89] Phillip, D., *Methods of numerical integration*. New York: Academic Press, 1975.

[90] Poette, G., Després, B., and Lucor, D., "Uncertainty quantification for systems of conservation laws," *Journal of computational physics*, vol. 228, no. 7, pp. 2443–2467, 2009.

[91] Putko, M. M., Newman, P. A., and III, A. C. T., "Employing densitivity derivatives for robust optimization under uncertainty in cfd," (Albuquerque, NM), 9th ASCE Specialty Conference on Probabilistic Mechanics and Structural Reliability, July 2004.

[92] Putko, M. M., Newman, P. A., III, A. C. T., and Green, L. L., "Approach for uncertainty propagation and robust design in cfd using sensitivity derivatives," No. AIAA-2001-2528, (Anaheim, CA), 15th AIAA Computational Fluid Dynamics Conference, June 2001.

[93] Rabitz, H. and Alis, O. F., "General foundations of high-dimensional model representations," *Journal of Mathematical Chemistry*, vol. 25, no. 2-3, pp. 197–233, 1999.

[94] Rabitz, H., Alis, O. F., Shorter, J., and Shim, K., "Efficient input-output model representations," *Computer Physics Communications*, vol. 117, no. 1-2, pp. 11–20, 1999.

[95] Rahman, S. and Xu, H., "A univarite dimension-reduction method for multidimensional integration in stochastic mechanics," *Probabilistic Engineering Mechanics*, vol. 19, no. 4, pp. 393–408, 2004.

[96] Rajnarayan, D., Haas, A., and Kroo, I., "A multifidelity gradient-free optimization method and application to aerodynamic design," No. AIAA-2008-6020, (Victoria, British Columbia), 12th AIAA/ISSMO Multidisciplinary Analysis and Optimization Conference, Sept. 2008.

[97] Rasmussen, C. and Williams, C., *Gaussian Processes for Machinary learning*. Cambridge, Massachusetts: the MIT Press, 2006.

[98] Raymer, D. P., *Aircraft design: A conceptual approach*. Washington, D.C.: American Institute of Aeronautics and Astronautics, Inc, 1999.

[99] Reese, C. S., Wilson, A. G., Hamada, M., Martz, H. F., and Ryan, K. J., "Integrated analysis of computer and physical experiments," *Technometrics*, vol. 46, no. 2, pp. 153–164, 2004.

[100] Robinson, T. D., Eldred, M. S., Wilcox, K. E., and Haimes, R., "Surrogate-based optimization using multifidelity models with variable parametrization and corrected space mapping," *AIAA Journal*, vol. 46, no. 11, pp. 2814–2822, 2008.

[101] Selig, M. S., McGranahan, B. D., and Broughton, B. A., "Summary of low-speed airfoil data." vol 5, preliminary data, available online, Jan. 2011.

[102] Smith, M., Wong, T.-C., Postdam, M., and Baeder, J., "Evaluation of computational fluid dynamics to determine two-dimensional airfoil characteristics for rotorcraft applications," *Journal of the American Helicopter Society*, vol. 51, no. 1, pp. 70–79, 2006.

[103] Smolyak, S. A., "Quadrature and interpolation formulas for tensor products of certain classes of functions," *Soviet mathematics - Doklady*, vol. 4, 1963.

[104] Su, J. and Renaud, J. E., "Automatic differentiation in robust optimization," *AIAA Journal*, vol. 35, no. 6, pp. 1072–1079, 1997.

[105] Taguchi, G., *Introduction to quality qngineering: designing quality into products and processes.* Tokyo, Japan: Quality Resources, 1986.

[106] Tatang, M. A., Pan, W. W., Prinn, R. G., and McRae, G. J., "An efficient method for parametric uncertainty analysis of numerical geophysical model," *Journal of Geophysical Research*, vol. 102, 1997.

[107] Vassberg, J. C., DeHaan, M. A., Rivers, S. M., and Wahls, R. A., "Development of a common research model for applied cfd validation studies," (Honolulu, Hawaii), 26th AIAA Applied Aerodynamics Conference, Aug. 2008.

[108] Wiener, N., "The homogeneous chaos," *American Journal of Mathematics*, vol. 60, 1938.

[109] Williams, C. K. I. and Rasmussen, C. E., "Gaussian processes for regression," in *Advances in Neural Information Processing Systems 8* (Touretzky, D. S., Mozer, M. C., and Hasselmo, M. E., eds.), (Cambridge, Massachusetts), pp. 514–520, The MIT Press, 1996.

[110] Xiu, D. and Hesthaven, S., "High-order collocation methods for differential equations with random inputs," *SIAM Journal on Scientific Computing*, vol. 27, no. 3, pp. 1118–1139, 2005.

[111] Xiu, D. and Karniadakis, E. G., "Modeling uncertainty in flow simulations via generalized polynomial chaos," *Journal of Computational Physics*, vol. 187, pp. 137–167, 2003.

[112] Xiu, D. and Karniadakis, G. E., "Wiener-askey polynomial chaos for stochastic differential equations," *SIAM Journal on Scientific Computing*, vol. 24, no. 2, pp. 619–644, 2002.

[113] Zang, T. A., Hemsch, M. J., Hilburger, M. W., Kenny, S. P., Luckring, J. M., Maghami, P., Padula, S. L., and Stroud, W. J., "Needs and opportunities for uncertainty-based multidisciplinary design methods for aerospace vehicles," Tech. Rep. TM 2002-211462, NASA, Langley Research Center, Virginia, July 2002.